

ELECTROSPUN CERAMIC FIBERMATS FOR FILTRATION APPLICATIONS IN
LUNAR MISSIONS FOR IN-HABITAT APPLICATIONS

By

APRATIM BISWAS

A DISSERTATION PRESENTED TO THE GRADUATE SCHOOL
OF THE UNIVERSITY OF FLORIDA IN PARTIAL FULFILLMENT
OF THE REQUIREMENTS FOR THE DEGREE OF
DOCTOR OF PHILOSOPHY

UNIVERSITY OF FLORIDA

2012

© 2012 Apratim Biswas

To my parents

ACKNOWLEDGMENTS

I would like to acknowledge all the support and advice that I have received from my advisor, Dr. Wolfgang M. Sigmund. I would also like to acknowledge Florida Space Research Initiative for funding the research. I am also thankful to the Dr. Chang-Yu Wu and his research group for collaborating with our research group and the Particle Engineering Research Center, UF and Major Analytical Instrumentation Center, UF for allowing me to use their facilities.

TABLE OF CONTENTS

	<u>page</u>
ACKNOWLEDGMENTS.....	4
LIST OF TABLES.....	7
LIST OF FIGURES.....	8
LIST OF ABBREVIATIONS.....	10
ABSTRACT	12
CHAPTER	
1 BACKGROUND	15
1.1 Motivation	15
1.2 Goal, Objectives and the Challenges – General Outline.....	16
1.3 Filtration.....	18
1.3.1 Filtration Technologies - Selection.....	18
1.3.2 Filtration Theories for Fibrous Filters.....	19
1.4 Fiber Processing.....	23
1.4.1 Overview of Various Fiber Processing Techniques.....	23
1.4.2 Electrospinning.....	24
1.5 Materials Selection.....	26
1.6 Photocatalysis.....	28
1.6.1 Photocatalytic Properties of Titania	28
1.6.2 Effect of Dopants on Photocatalytic Activity of Titania.....	30
2 EXPERIMENTAL METHODS	42
2.1 Preparation of Aqueous TiO ₂ -SiO ₂ Hybrid Sol	42
2.2 Electrospinning of Ceramic Fibers	43
2.2.1 Modification of Fiber Diameter.....	44
2.2.2 Heat Treatment	46
2.3 Preparation and Electrospinning of Doped Titania Sol.....	47
2.3.1 Preparation of Titania Sol.....	47
2.3.2 Addition and Electrospinning of Niobium Doped Titania Sol.....	47
2.4 Determination of Filtration Properties.....	49
2.5 Determination of Photocatalytic Properties	50
3 RESULTS AND DISCUSSIONS	59
3.1 Effect of Electrospinning Conditions on Fiber Morphology, Crystal Structure and Mechanical Properties of TiO ₂ -SiO ₂ Fibers	59
3.2 Filtration Properties of Electrospun Ceramic Fibermat.....	65

page

3.3 Influence of Niobium Dopant on the Morphology, Crystal Structure and Photocatalytic Activity of Electrospun Titania Fiber	69
4 CONCLUSIONS AND FUTURE WORK	109
LIST OF REFERENCES	112
BIOGRAPHICAL SKETCH.....	119

LIST OF TABLES

	<u>page</u>
2-1 Addition of niobium ethoxide to titania sol (9 ml)	53
2-2 Addition of $\text{Nd}(\text{NO}_3)_3 \cdot 6\text{H}_2\text{O}$ to titania sol (9 ml).....	54
3-1 $\text{TiO}_2\text{-SiO}_2$ aqueous sol compositions and electrospinning conditions used throughout the research for $\text{TiO}_2\text{-SiO}_2$ sol [$E = 1 \text{ kV/cm}$, $Q = 0.6 \text{ ml/h}$, collector distance = 25 cm].....	77
3-2 Fiber diameter of electrospun $\text{TiO}_2\text{-SiO}_2$ fibers after heat treatment in presence of air in a box furnace	78
3-3 Loss of fiber diameter on heat treatment at 600°C in air for 3 hours	79
3-4 Influence of addition of ethanol on fiber diameter of heat treated electrospun $\text{TiO}_2\text{-SiO}_2$ fibers (2% w/v PVP, $M_w 1.3 \times 10^6$ used as polymeric aid).....	79
3-5 Modifying fiber diameter of heat treated fiber by varying different electrospinning parameters	80
3-6 Fiber morphology for electrospun fibers of pure titania and niobium doped titania after heat treating at 600°C for 3 hours. 4% w/v PVP was added. Electric field strength and flow rate were maintained at 1 kV/cm and 0.6 ml/h ...	81
3-7 Specific surface of niobium doped titania fibers after heat treatment	82

LIST OF FIGURES

	<u>page</u>
1-1 Various filtration mechanisms in action in collecting aerosolized particles by a single fiber	34
1-2 Calculated fractional collection efficiency for particulates of different sizes	35
1-3 Schematic diagram of conventional fiber processing using wet/dry/melt spinning technology ^[22]	36
1-4 Schematic diagram of electrospinning set-up.....	37
1-5 Ashby chart for wear rate constant vs hardness for various material classes ^[35]	38
1-6 Schematics of the photocatalytic reaction process.....	39
1-7 Effect of doping transition metals on electronic band structure in TiO ₂	39
1-8 Influence of atomic number on the effect of doping transition metals on the electron band structure of TiO ₂	40
2-1 Processing of TiO ₂ -SiO ₂ aqueous sol	55
2-2 The electrospinning set-up used in electrospinning TiO ₂ -SiO ₂ . A vertical set-up was used throughout the research.	56
2-3 Heat treatment of TiO ₂ -SiO ₂ fibermat.....	57
2-4 The filtration testing set-up used for determining the filtration properties of electrospun TiO ₂ -SiO ₂ fibermats.....	58
2-5 Chamber used to expose sample to ultra violet or visible light radiation	58
3-1 Influence of PVP content on the morphology of electrospun TiO ₂ -SiO ₂ fibers ...	83
3-2 TiO ₂ -SiO ₂ fibermats, electrospun from sol containing 0.4% w/v PVP, after heat treatment at 600°C for 3h.	85
3-3 Flexibility of heat treated TiO ₂ -SiO ₂ fibers.....	86
3-4 Morphology and crystallinity of heat treated TiO ₂ -SiO ₂ nanofibers	88
3-5 Chemistry behind synthesis of aqueous hybrid sol of TiO ₂ -SiO ₂	90
3-6 Electrospun micron sized TiO ₂ -SiO ₂ fibers.....	91

	<u>page</u>
3-7 Pore size distribution of electrospun TiO ₂ -SiO ₂ fibermat obtained using BJH method	92
3-8 Original particle size distribution of aerosol generated in filtration testing set-up	93
3-9 Experimentally determined pressure drop of electrospun TiO ₂ -SiO ₂ fibermats plotted vs average fiber diameter	94
3-10 Plot of mass/(square of thickness) vs average fiber diameter	96
3-11 Collection efficiency of ceramic fibermats plotted versus average fiber diameter	97
3-12 The effect of using activated carbon fiber as collector for electrospun fibers	98
3-13 Dependence of fiber diameter after heat treatment on the niobium dopant level	102
3-14 X-ray diffraction plots demonstrating the impact of niobium dopant on anatase to rutile phase transformation	103
3-15 Effect of niobium dopant on diameter and specific surface of electrospun TiO ₂ fibers.	105
3-16 BJH pore size analysis of niobium doped titania fibers.....	106
3-17 Influence of niobium dopant on UV/Vis absorption spectra of titania fibers	107
3-18 Differential reflectance of niobium doped titania	108

LIST OF ABBREVIATIONS

Δp	Pressure drop across a filter
P	Penetration factor for a filter
η	Collection efficiency of a filter
Q	Quality factor of a filter. Also used to denote flow rate in equations describing electrospinning process
α	Porosity of a filter
E_R	Collection efficiency due to interception
d_p	Diameter of particulates in aerosol
d_f	Diameter of fiber
Ku	Kuwabara hydrodynamic factor
E_t	Collection efficiency from entrapment of particles due to inertial impaction
ρ_p	Particle density
C_C	Cunningham factor
μ	Viscosity of gas
V	Face velocity of air-stream
E_D	Collection efficiency due to diffusion of small particles
D	Diffusion coefficient
h_t	Terminal jet diameter
$\bar{\epsilon}$	Dielectric constant of air
γ	Surface tension of a sol or any liquid
I	Current
χ	Radius of curvature of the jet at the regions of whipping instability in electrospinning process
Φ	Quantum yield

k_{CT}	Charge transfer rate
k_R	Recombination rate of holes and electrons
A	Absorbance.
ΔA	Loss in absorbance
ϵ	Absorptivity
C_0	Initial dye concentration
C	Concentration of dye at any particular time
ΔC	$C_0 - C$; i.e. loss is concentration of dye due to degradation
ρ	Density of any material. For the purpose of this dissertation it stands for the density of the material of which the fibers are made
Eq	Equation

Abstract of Dissertation Presented to the Graduate School
of the University of Florida in Partial Fulfillment of the
Requirements for the Degree of Doctor of Philosophy

ELECTROSPUN CERAMIC FIBERMATS FOR FILTRATION APPLICATIONS IN
LUNAR MISSIONS FOR IN-HABITAT APPLICATIONS

By

Apratim Biswas

May 2012

Chair: Wolfgang Michael Sigmund
Major: Materials Science and Engineering

In the absence of atmosphere and hydrosphere, there are few collisions between dust particles in the lunar environment. Further, particles become charged in presence of cosmic rays and similarly charged particles repel each other. Hence particles retain sharp edges and often have high aspect ratios. When exposed to lunar dust, humans show symptoms similar to hay fever. Such particles are also damaging to equipment. Humans and robots, used in operations, can bring such dust particles inside the human habitat making them airborne. High efficiency particulate air (HEPA) filters provide an effective way to trap such particles. But due to environment conditions, polymer based filters are susceptible to mechanical erosion. The presence of high energy radiation, due to the absence of atmosphere and magnetic fields, is also damaging to polymers. Ceramic materials are resistant to abrasion and radiation and hence were chosen as the preferred class of materials for the filtration media. Among all the ceramics, TiO_2 was selected for its photocatalytic activity which may play a key role in energy-efficient survival in space or lunar stations. Such fibers are multi-functional with the advantage of self-cleaning property in presence of radiation. However ceramic fibers, including TiO_2 fibers, have a significant disadvantage of their own. They are brittle and were

considered too prone to failure to be successfully used as a filtration media when they reach nanometer dimensions. This dissertation describes the advances in fabrication and understanding of fundamentals in overcoming these challenges. In absence of crack initiation sites, amorphous ceramic fibers have near theoretical strength and strain to failure. Amorphous $\text{TiO}_2\text{-SiO}_2$ fibermats, with lower flaw populations and exceptional surface quality, have been developed. They can be rolled to a radius of curvature of 3.4 mm – exhibiting flexibility. The fibermats are also mechanically robust and can withstand the stress associated with general handling and fixture used for holding the filtration media. Electrospinning was selected as the fabrication method due to superior performance towards fiber diameter uniformity and the ability to decrease fiber diameters to the nm level. Filtration tests have been carried out on such fibermats concerning a number of key variables such as fiber diameter, particle size, pressure drop and more. Multifunctionality, as filter material and as photocatalyst, allows the filters to be regenerable. Furthermore, organic vapors (odors) and plant super hormones (ethylene gas) can be oxidized. This is key for a sustainable human base where food needs to be grown and the level of odors in habitat has to be minimized. Ceramic materials based on TiO_2 and titania composites were selected. To enhance the catalytic properties doping with a pentavalent ion, viz. niobium, with varying concentrations was done. Materials were electrospun and characterized. An increase of niobium yields stabilization of the anatase phase at 600°C as evident from XRD patterns. Higher treatment temperatures allow a transformation to rutile. This is important since the semiconductor junction of anatase to rutile decreases electron-hole recombination rate, which enhances the photocatalytic activity. Furthermore, doping

anatase with niobium increases the porosity and with it the catalytically active area. In fact the specific surface area of titania fibers increases by almost 6 times when doped with only 2.5 at% niobium. However, in this work reduced photocatalytic activity was observed. It is hypothesized that phase separation of the niobium rather than doping in a solid solution occurred which will change the properties of the semiconductor junction in an unfavorable way. The other possible explanation is the decrease in the anatase – rutile semiconductor junction in niobium doped titania.

CHAPTER 1 BACKGROUND

1.1 Motivation

The core motivation behind the research was to develop filtration media suitable for application in lunar environment, especially in-habitat. There are several factors which make lunar environment unique. In the absence of atmosphere there is very little dust particle-dust particle collision. The particles are also exposed to plasma and UV radiations and are charged and repel each other^[1, 2]. This results in particles having sharp jagged edges and high axial ratios. In-habitat, such sharp hard particles can also damage the dermal water vapor barrier^[3] in humans and are also irritating to eyes. The lunar dust particles can also be damaging to the lungs^[4]. Hyper-reactivity to lunar dust has been observed before by astronauts during the Apollo missions^[5]. Such particles are too abrasive for polymer based fibrous filters. The high energy radiations are also damaging to the polymer. On the other hand ceramics are not only hard and abrasion resistant but can also withstand the irradiative environment. In filtration theory of fibrous filters, a reduction in fiber diameter is related to a decrease in pressure drop due to decrease in drag force^[6] and an increase in filtration quality factor. When used in-habitat, micro-organisms can be trapped in such filters. Photocatalysis can be used as a mechanism to degrade any such deposition and in turn help in repeated use of the filtermat. This served as the motivation behind the search for ceramic fibers with high photocatalytic activity. Niobium was added as dopant to titania before fibers were electrospun to study for their impact on the photocatalytic properties of titania fibers. If photocatalytic enough, such fibrous filters would self-clean in sunlight, especially considering the fact that in the absence atmosphere, the lunar environment is highly

irradiative. Thus a potentially harmful fact can be utilized in such a way that it yields beneficial result.

While the core motivation in the research has been in space applications, such fibermats have enormous potential as high efficiency particulate air (HEPA) filter in terrestrial applications too. The Department of Energy defines HEPA filters as filters which have a minimum efficiency of 99.97% for aerosolized 300 nm particles^[7]. Such filters have been proven as an effective protection against contamination of SARS virus^[8] through inhalation and preventing aspergillosis in immunocompromised individuals^[9] with hematologic malignancies. Development of HEPA filters is also a national security priority as a protection against biological warfare and bio-terrorism agents such as anthrax^[10]. In presence of ultraviolet radiation, photocatalytic HEPA filters can destroy such virulent species and maybe used multiple times in such applications.

1.2 Goal, Objectives and the Challenges – General Outline

This section of the dissertation aims at clearly identifying the long term goal, intermediate objectives towards it and the challenges which must be surmounted to attain the desired objectives. And along the way, the current state of the art has been explained with an emphasis on the gap in knowledgebase that must be filled to attain the final goal.

The dissertation is the result of the body of work done towards completion of a project where the main goal is to prepare filtration media for use in lunar mission. With that as the bottom line, we have two prominent choices – fibrous filters and membranous filters^[11]. The membranous filters have pores in the membrane and the fibrous filters are composed of several layers of fibers deposited on top of each other.

There are several factors which have to be considered before a particular filtration media is selected. Briefly, these include collection efficiency and pressure drop. Porous fibers have higher collection efficiency and can entrap a larger fraction of particles but the fibrous filters have lower pressure drop and require lesser operating energy. In the absence of abundant energy source, the lesser operating energy requirement makes fibrous filter the winner between the two types.

With the type of filtration media thus determined, we are faced with a new challenge – the nature of lunar dust itself. Erosive processes like atmosphere or hydrosphere are absent^[1, 2] and particles are similarly charged due to the presence of cosmic rays. All these factors ensure that there is little particle-particle collision and hence the particles remain sharp with jagged edges – too hard and abrasive for polymeric filter media. A hard abrasion resistant material is required and ceramic materials would be the perfect candidate for that.

Heat treated polycrystalline ceramic fibers are notoriously brittle and are impossible to be fitted into the filtration set-up. There is a lack of technological evolution towards developing mechanically robust and flexible fibermats which can be used in this application. This is an area which has been addressed several times throughout this dissertation with the eventual development of flexible fibermats. The filtration properties of the fibermats, thus prepared, have been studied, reported and discussed.

In an ideal scenario the fibermats can be recycled and used multiple times. This requires cleaning on a regular basis. Due to lack of abundant energy sources, minimizing the energy utilization is always important in space. If a material is developed which exhibits photocatalytic activity in the visible light range then sunlight itself may be

used to clean and re-use the filters. Thus the final portion of the body of work is devoted to increasing the utility of the filters and is included in the last part of the dissertation.

1.3 Filtration

Keeping in view the fact that the motivation behind the research is developing a solution for filtration application, it is important to briefly explain the various options that are available and the logical reasoning behind choosing fibrous filters. It is also important to briefly explore the filtration theory since one of the objectives is to try to study how fiber diameter, filter thickness, void ratio etc. influence the filtration properties like pressure drop and filtration quality factor.

1.3.1 Filtration Technologies - Selection

The types of filters which are most important for sampling and filtering aerosolized particles are fibrous and porous filters^[6]. In fiber based filters, a mat of fine fibers is used as filtration media in a direction perpendicular to the flow of airflow and contrary to the popular misconception; such filters can trap aerosolized particles much smaller than the separation between the fibers. In porous filters the porosity is about 50-90% less compared to fibrous filters. The aerosolized particles are trapped when the air-stream carrying them flows through the complex porous structure. Similar to fibrous filters, porous filters too can trap particles smaller than the pore size. The most important factors to consider while selecting a filter are a) pressure drop, b) collection efficiency and c) the quality factor^[6]. In porous filters the collection efficiency is high but that comes at the expense of high pressure drop. Having a higher pressure drop implies that a higher energy is required for filtration and hence an increase in the operating expense. Taking all these factors into consideration, fibrous filter was selected to be most appropriate for the application.

1.3.2 Filtration Theories for Fibrous Filters

Fibrous filters are often used to capture aerosolized particles in air. Before we can understand the details of how a fibrous filter works and why it is an excellent choice for the intended application, a few concepts must be discussed. The first such term is collection efficiency. In the most abstract sense, collection efficiency of a single fiber may be defined as the ratio between the cross-sectional area of the air-stream from which particles are removed to the projected area in the direction of the flow^[12]. This can eventually be formulated as the fraction of entering particles that are retained by the fiber^[11].

$$\eta = \frac{\textit{number of particles in the inlet} - \textit{number of particles in the outlet}}{\textit{number of particles in the inlet}} \quad (1-1)$$

In filtration theory a term called penetration factor is often used which includes the collection efficiency as a factor. The penetration factor reflects the fraction of entering particles that exit the filter. The penetration factor is often denoted by P.

$$P = \frac{N \textit{ out}}{N \textit{ in}} \quad (1-2)$$

In terms of the collection efficiency, η , P can be expressed by Eq. 1-3.

$$P = 1 - \eta \quad (1-3)$$

The second important parameter in the theory of fibrous filters is the pressure drop, Δp . The pressure drop is related to the energy required for the air stream to flow through the filter membrane, the higher the energy required, the higher is the pressure drop.

An ideal filter should have 100% collection efficiency and a very low pressure drop. Quality factor is the parameter which reconciles both these parameters. Filtration quality factor, Q , is expressed by Eq. 1-4.

$$Q = \frac{\ln\left(\frac{1}{P}\right)}{\Delta p} \quad (1-4)$$

In filtration theory, instead of considering collection efficiency and pressure drop as separate parameters, the quality factor gives us a single number which can be used to judge a filter. Higher the quality factor is for a fibermat, the better it is as a filter.

A large portion of the conducted research is devoted to the understanding of how fiber diameter, filter thickness, porosity etc. influence the filtration properties. In light of this it is important to look into the theory of filtration as it relates to a single fiber.

Particles are captured by any or a combination of the three methods depending on their size: a) interception, b) inertial impaction and c) diffusion. In the theory it is assumed that the particles are trapped onto the fiber due to Van der Waals force of attraction. Interception is the process that takes place when the particle reaches within a distance nearly equal to the radius of the particle. The collection efficiency, E_R , of the interception method is given by Eq. 1-5.

$$E_R = \frac{(1 - \alpha)d_p^2}{Ku(d_f^2 + d_p \cdot d_f)} \quad (1-5)$$

where, E_R is the efficiency of the interception, α is the porosity of the filter and d_p and d_f are the diameter of particle and fiber respectively. Ku is known as Kuwabara hydrodynamic factor^[6] and is expressed by Eq. 1-6.

$$Ku = -\ln\frac{\alpha}{2} - \frac{3}{4} + \alpha - \frac{\alpha^2}{4} \quad (1-6)$$

Sometimes the path of the particle is diverted from the direction of the airflow because of inertia. This is known as the inertial impaction. The efficiency of this type of particle entrapment is expressed as E_t and given by Eq. 1-7^[13].

$$E_t = \left(\frac{\rho_p d_p C_c U}{36\eta K u^2 d_f} \right) \left\{ (29.6 - 28\alpha^{0.62}) \left(\frac{d_p^2}{d_f^2} \right) - 27.5 \left(\frac{d_p}{d_f} \right)^{2.8} \right\} \quad (1-7)$$

In the equation ρ_p is the particle density and C_c is known as the Cunningham Correction Factor arising from the gas slippage^[14]. U is the face velocity of the air and η is the viscosity of the air.

A different type of particle entrapment dominates when particles are much smaller and $d_p/d_f < 0.4$. In such cases, the particles move out of the streamline due to Brownian motion in irregular path and are ultimately captured by diffusion. The collection efficiency of a single fiber due to diffusion, E_D , is given by Eq. 1-8.

$$E_D = 2 \left(\frac{D}{d_f U} \right)^{\frac{2}{3}} \quad (1-8)$$

where D is the particle diffusion coefficient and U is the face velocity as mentioned previously. The collection efficiency is proportional to $d_f^{-2/3}$, $d_f^{-3/4}$ and $d_f^{-2/3}$ respectively in the interception, inertial impaction and diffusion modes respectively. Thus from the perspective of all the three entrapment methods, decrease in fiber diameter is associated with an increase in collection efficiency.

Another factor to consider is the pressure drop caused by the resistance to airflow across the fiber. This resistance is called the drag force and is the main contributor to

the pressure drop in the fibrous filters. It is related to fiber diameter by the Stoke's law expressed in Eq. 1-9.

$$F_D = \frac{3\pi\mu V d_f}{C_C} \quad (1-9)$$

where μ is the viscosity of the gas, V is the face velocity of the gas as before and d_f is the fiber diameter. C_C is the correction factor related to the contribution of slip flow on the drag force and is called the Cunningham factor^[6, 14]. For high Knudsen number (K_n) in the range of 0.5 to 134, C_C is expressed by Eq. 1-10.

$$C_C = 1 + A.K_n \quad (1-10)$$

where A is an experimentally determined constant. Since pressure drop decreases and collection efficiency increases with decrease in fiber diameter, theoretically, a reduction in fiber diameter should lead to an increase in quality factor. A separate section has been devoted in our research to study the relationship between various parameters in filtration. Figure 1-1 illustrates the various filtration mechanisms of capture of aerosolized particles in air as has been explained in this section.

There is another concept in the filtration theory which has been used while designing the experimental methods. The collection efficiency of a fibrous filter is dependent on the size of particulates in the aerosol. Different filtration mechanisms are active for particulates in different size range and it has been experimentally found that the most penetrating particle size (MPPS) is usually in the range of 100 nm – 500 nm^[15, 16], with most experiments for filtration quality factor recommended at particle size of 300 nm^[7, 16]. Figure 1-2 illustrates the concept of MPPS. As evident from the diagram, the

MPPS also depends on the fiber diameter and generally decreases with decrease in fiber diameter.

1.4 Fiber Processing

While the main application for ceramic fibers in the course of our research has been filtration, synthesis of fibers and especially nanofibers are of great importance in several other areas such as tissue engineering^[17-19] and catalyst support^[20, 21]. In the following sections the different traditional ways of fiber processing like dry spinning, wet spinning, melt spinning^[22] and newer non-traditional alternatives like electrospinning^[22, 23] are discussed. Finally electrospinning has been explored as the preferred option for the specific application of interest.

1.4.1 Overview of Various Fiber Processing Techniques

The specific traditional technique used to process fibers is based on the solubility of the polymer in solvents and on whether they melt at higher temperatures. For the polymers which are soluble, it is dissolved in a solvent and spun. After this the solvent can be removed either by evaporation or extraction. When the solvent is removed through evaporation it is known as dry spinning. It is known as wet spinning when the solvent is removed by extraction by either utilizing or not utilizing a chemical reaction. Diffusion plays a very important role in both the systems. A different method known as melt spinning can be used for polymers which are not soluble but can be melted. As the nomenclature suggests, the polymer is at first melted and then spun into fibers. Figure 1-3 shows the generic schematic representation of the fiber formation process. As illustrated in the figure, the solution or the melt (depending on the specific process) is fed into the system either by an extruder or by compressed gas (usually nitrogen). After being passed through a filter, the solution or the melt is fed into a spinneret which is a

metallic plate with enough strength to withstand the pressure gradient and having several capillaries^[22]. The extruded solution or melt is finally treated depending on the nature of the material and the exact method to form the final fibers.

The above generic description of traditional technology has been intentionally over-simplified. In real application such technologies are really complicated and involve expensive equipment having very high precision^[22]. At present there are several newer alternative techniques, including electrostatic spinning^[22-24], spray spinning^[22, 25] and centrifugal spinning^[22, 26, 27] which do not require spinneret and fiber transport rollers. Among these processes, electrostatic spinning, more commonly known as electrospinning, has been adopted for our purpose as it is the most simple, very versatile and provides ample opportunity to vary fiber diameter from few tens of nanometers to several microns^[24, 28, 29]. Using suitable polymer as aid, ceramic fibers can be easily electrospun from precursor sol.

1.4.2 Electrospinning

A significant portion of the research has been devoted to fiber processing by electrospinning and it is important to present a concise overview of the electrospinning process. Electrospinning is the process of generating fibers using a high electrostatic field and has been known since the 1930s^[23, 24, 30, 31]. A very high electrostatic field is applied between a syringe containing polymer or ceramic sol to be electrospun and a metallic collection target. This electric field leads to charge stored in the material and finally fibers are drawn by it.

The electrospinning process can be divided into three phases^[24, 32]. In the first phase, a fluid jet is ejected from the syringe needle and is smoothly accelerated by the electric field. During this process, a cone is formed by the balance of several forces

acting on the liquid jet. Gravitational force and electric polarization stress tend to elongate the droplet, forming a cone known as the Taylor Cone. Opposing these two forces there are two other forces – surface tension and normal electrical stress which try to form a droplet. The general set-up for electrospinning is presented in Figure 1-4. The figure also illustrates the various forces which are in equilibrium to form the cone. Once the electrostatic force overcomes the surface tension, a fine charged jet is ejected from the Taylor cone.

The second phase starts once the jet starts moving towards the collector. In this stage of electrospinning there are three types of instabilities which may occur – i) axisymmetric Rayleigh instability due to surface tension leading to the formation of droplets, ii) axisymmetric instability induced by electric field and, iii) non-axisymmetric instability, leading to bending of fibers^[24, 32-34]. The third form of instability is the most important from the perspective of reducing fiber diameter. Which instability will dominate during the process depends on the viscosity / conductivity ratio. With increase in the surface charge density and the electric field strength, the effect of classical Rayleigh instability is suppressed while enhancing the dominance of all forms of instabilities induced by electric field. Increase in the non-axisymmetric instability and whipping mode enhances the ability of the process to reduce the fiber diameter.

In the final stage of the electrospinning process, the repulsive force from the surface charge of the jet is balanced by the surface tension. Because these forces compensate each other, the stretching and thinning of the jet due to whipping instability ceases and the jet attains its final diameter. Mathematically the terminal diameter can be obtained from the expression in Eq. 1-11.

$$h_t = \left(\gamma \bar{\varepsilon} \frac{Q^2}{I^2} \frac{2}{\pi(2 \ln \chi - 3)} \right)^{1/3} \quad (1-11)$$

where h_t is the terminal diameter, γ is the surface tension, Q is the flow rate of the liquid, I is the current, $\bar{\varepsilon}$ is the dielectric constant of air and χ is the ratio of radius of curvature of the jet at regions of whipping instability (R) to the diameter of the jet (h) and is assumed to be approximately 100.

1.5 Materials Selection

The materials selection process for this research has been briefly mentioned in the section on motivation. In this section we would first explore the initial material selection in details and then briefly mention the other considerations made to enhance the photocatalytic activity with the objective to have a potential multifunctional final material.

Harder a material is, the more resistant it is to abrasion. Since the material needs to survive the erosive nature of the lunar dust, the primary consideration for the material is hardness. Ashby chart^[35] for hardness vs wear rate constant, as illustrated in Figure 1-5 shows the clear superiority of ceramics in this respect.

Out of several available options in ceramics, TiO_2 is particularly interesting because of its photocatalytic activity^[36-39]. However, similar to most ceramics, TiO_2 is brittle. While the fracture toughness for metals are in the range from 10s – 100s $\text{MPa}\cdot\text{m}^{1/2}$, for ceramics it ranges from 0.1 – 4 $\text{MPa}\cdot\text{m}^{1/2}$ ^[40, 41]. Among the various forms of ceramics the fracture toughness of single crystals ranges from 0.3 to 2.0 $\text{MPa}\cdot\text{m}^{1/2}$ while polycrystalline ceramics have a higher toughness ranging from 2-4 $\text{MPa}\cdot\text{m}^{1/2}$. In comparison amorphous ceramics have a much lower toughness, usually below 1 $\text{MPa}\cdot\text{m}^{1/2}$.

$m^{1/2}$. This is because while a crack has to propagate along the grain boundaries in polycrystalline ceramics and along a close-packed plane in single-crystal ceramics, in amorphous ceramics, due to the absence of any preferred plane, crack propagates perpendicular to the surface. But near theoretical fracture toughness have been observed in micron sized SiO_2 fibers^[40, 41] when fiber surfaces were coated with a very thin layer of epoxy to prevent crack initiation. Electrospun TiO_2 nanofibers crystallize with grain size approximately $30\mu\text{m}$ when heat treated at 500°C ^[29] however SiO_2 has a much higher crystallization temperature of 1500°C and remains amorphous at 500°C ^[42]. For this reason a hybrid oxide of TiO_2 and SiO_2 was selected as the preferred material with the hypothesis that an amorphous SiO_2 matrix can improve the mechanical toughness.

Apart from the consideration of mechanical properties there was another important motivation behind selecting TiO_2 - SiO_2 and it has to do with the stability of the precursor sol itself. Ethanol based titania sol is not stable and within a few hours titania starts precipitating in the system. This happens due to the high chemical reactivity of titanium alkoxides, which are commonly used as precursors to titania, to the moisture present in air. In the aqueous sol prepared in our research, after undergoing hydrolysis and condensation, Si-O-Ti bonds are formed. This inhibits the crystallization of TiO_2 and hence a stable sol is produced. The sol can be stored for several months. Details of the reaction would be provided in a later section.

In the final section of the research an attempt have been made to improve the photocatalytic activity of titania by using niobium as a dopant. Briefly, the most important components of photocatalysis are generation of $[\text{OH}\cdot]/\text{H}_2\text{O}_2$ and recombination of

electrons and holes. Since recombination of electron and holes inhibits the formation of $[\text{OH}^\cdot]/\text{H}_2\text{O}_2$, reducing the rate of recombination is an effective technique to enhance the photocatalytic activity of a material. Pentavalent (Nb^{5+}) ions have been doped in an attempt to create trapping levels for holes to improve the photocatalytic activity. Because of the amount and nature of the background that has to be covered for this part of the research a separate section has been dedicated to it in section 1.6.

1.6 Photocatalysis

The intended application for the material is for it to be used as a fibrous filtration media in space within human habitat. So an important criterion for the material is that it should be easy to clean. A process such as photocatalysis would be ideal for use to clean the fibermats using a light source of appropriate wavelength. If a fiber mat can be developed with a material which requires light having wavelength in the visible range it would be ideal for application even in space stations where it can self-clean using sunlight.

1.6.1 Photocatalytic Properties of Titania

Titania is a semiconductor with wide band-gap of 3.2 eV for the anatase phase and 3.0 eV for the rutile form ^[43, 44]. Strictly speaking, while all semiconductors have photocatalytic properties, oxides and compound semiconductors exhibit better photocatalytic activity ^[45, 46]. There are two forms of photocatalytic reactions – catalyzed photoreaction and sensitized photoreaction. In the catalyzed photoreaction the initial photoexcitation occurs in an absorbate molecule. This excited molecule then interacts with the catalyst substrate and transfers electron^[46, 47]. On the other hand, in case of sensitized photoreaction, photoexcitation takes place first in the catalyst substrate and the substrate then interacts with absorbate molecule^[46]. These processes are compared

in the schematics in Figure 1-6. Generally, when mentioned in the context of TiO₂, photocatalysis refers to sensitized photoreaction.

The photocatalytic reaction may be divided into several parts and each step needs to be individually considered to ascertain where improvements may be made to enhance overall photocatalytic activity. The main reaction steps along with time required for each are summarized below^[48]. Flash photolysis^[49, 50] was the technique which was used to measure the reaction times.

Photoexcitation and generation of charge carriers; 10⁻¹⁵ seconds:



Migration of holes to the surface and trapping; 10x10⁻⁹ seconds:



Migration of electrons to the surface of the catalyst and trapping; 100x10⁻¹² seconds:



Recombination of electron with holes trapped in $\{>Ti^{IV}OH\}^+$; 100x10⁻⁹ seconds:



Recombination of holes; 10x10⁻⁹ seconds:



Oxidation (10⁻³ seconds) or reduction (100 x 10⁻⁹ seconds):





where vb and cb stand for valence band and conduction band respectively and ir stands for electron excited by radiation.

The photocatalytic efficiency of a material is measured in terms of a quantity called quantum yield. Quantum yield can be defined as the number of events happening for each photon that is absorbed. This quantity combines both the charge transfer rate and recombination rate and considers probabilities for all pathways for electrons and holes^[47]. In an ideal situation, quantum yield (Φ) is directly proportional to charge transfer rate (k_{CT}) and inversely proportional to the sum of charge transfer rate and electron-hole recombination rate (k_R). This is expressed in Eq. 1-20.

$$\Phi \propto \frac{k_{CT}}{k_{CT} + k_R} \quad (1-20)$$

A close look at the reaction steps reveals that while oxidation/reduction takes time in the range of milliseconds and 100s of nanoseconds, the recombination of holes and electrons takes 10-100s nanoseconds. Thus slowing down the rate of recombination of holes is more effective in increasing the quantum yield and in turn improving the photocatalytic activity. In the work described in this dissertation an attempt has been made towards this end by using dopant. The choice of the specific dopant has been discussed in details in section 1.6.2.

1.6.2 Effect of Dopants on Photocatalytic Activity of Titania

Using dopants with a different oxidation state than titanium is a very effective method to improve the photocatalytic activity^[51]. Specifically, the influence of doping transition metals on the photocatalytic activity of semiconductor photocatalyst has been

of interest for several decades now ^[52-57]. Transition metal ions like Fe^{3+} and Cu^{2+} ^[58] improves the photocatalytic activity by generating trapping energy level in the forbidden energy band and inhibits electron – hole recombination ^[47]. This is represented visually in Figure 1-7. When doped, the transition metal ion can occupy either interstitial sites or substitutional sites depending on the specific ion.

Apart from inhibiting electron-hole recombination, there is another effect of addition of dopants which has a great importance in terms of applicability of the material. In undoped TiO_2 the energy a photon is required to have to start a photocatalytic reaction is greater than the band gap. This is because to form a charge carrying electron-hole pair, an electron must be excited to the conduction band. But in the presence of electron trapping energy levels, the energy required by a photon is only the energy difference between the valence band and the lowest trapping level. This has some far reaching consequences. Because of the wide band gap of 3.2 eV in undoped TiO_2 , high energy UV radiation is required for the reaction to take place. However when doped with certain transition metal ions, TiO_2 has displayed photocatalytic properties in the presence of radiation having wavelength in the visible light range ^[44, 52, 54, 55]. Only about 3%-5% of solar energy on earth is in the form of UV and thus, if used on terrestrial surface, only a small fraction can be utilized to initiate the photocatalytic activity in such material ^[44, 57, 59]. So photocatalysis induced by photons in the visible light range is a highly desired property.

Figure 1-8. A) explains how specific transition metals change the density of states in TiO_2 . The electronic states were obtained by using first principal band calculation based on density function theory ^[44]. In the presence of transition metals with partially

filled d-orbitals new states appear from the overlap of oxygen orbitals and orbitals from the dopant. As a general rule, the states exhibit a red shift (i.e. decrease in the energy levels) with addition of dopants and this red-shift increases as the atomic number of the dopant added increases^[60-66] [44]. This red shift is explained by the charge transfer between the d-orbitals of the dopant atoms and the conduction or valence bands of TiO₂ [44, 61]. Photoconductivity both from cathodic process (due to electrons in the conduction band) and anodic process (due to holes in the valence band) has been observed in TiO₂ doped with transition metals^[64-66]. This observation can be rationalized by the mechanism illustrated in the schematic in Figure 1-8. B.

When doped with vanadium, electron transition from valence band to the t_{2g} electron level is made possible by a photon having energy in the visible light range. The holes that are left in the valence band in the process contribute to anodic photocurrent. The case is quite different in case of TiO₂ doped with iron. Since iron has a higher atomic number compared to vanadium, its t_{2g} electron levels have much lower energy and actually overlap the valence band. Photons having energy in the visible light range can lead to electron transfer from the t_{2g} level to the conduction band. In this case anodic photocurrent from the holes and cathodic photocurrent from electron, both are observed. Chromium has an atomic number in between vanadium and iron and its t_{2g} energy level lies almost at the middle of the valence and conduction band. In this case two separate electron transitions occur when irradiated by visible light. There is an acceptor transition in which electron is transferred from the valence band to t_{2g} level and a donor transition where electron is transferred from t_{2g} to conduction band. Similar to

the case of iron doping, both anodic and cathodic photocurrents are observed due to presence of both holes and conduction band electrons.

Even though several transition metal dopants have shown significant enhancement in photocatalytic activity, little research work has been published on the influence of doping with niobium. In one report titania particles doped with niobium has shown improved photocatalytic activity^[67]. For each Ti^{4+} atom substituted by Nb^{5+} ion, one excess electron exists in the 3d orbital of titanium atom, ^[68] leading to better photoconductivity in niobium doped titania^[68, 69]. Niobium has also been observed to inhibit the phase transformation of titania from anatase to rutile^[70, 71]. The probable reason for this is reduction in oxygen vacancies^[70, 72]. The electron-hole recombination rate in anatase is much lower than rutile and hence anatase shows better photocatalytic activity^[73]. These factors motivated the research on studying the effect of niobium doping on the photocatalytic property of electrospun titania fibers.

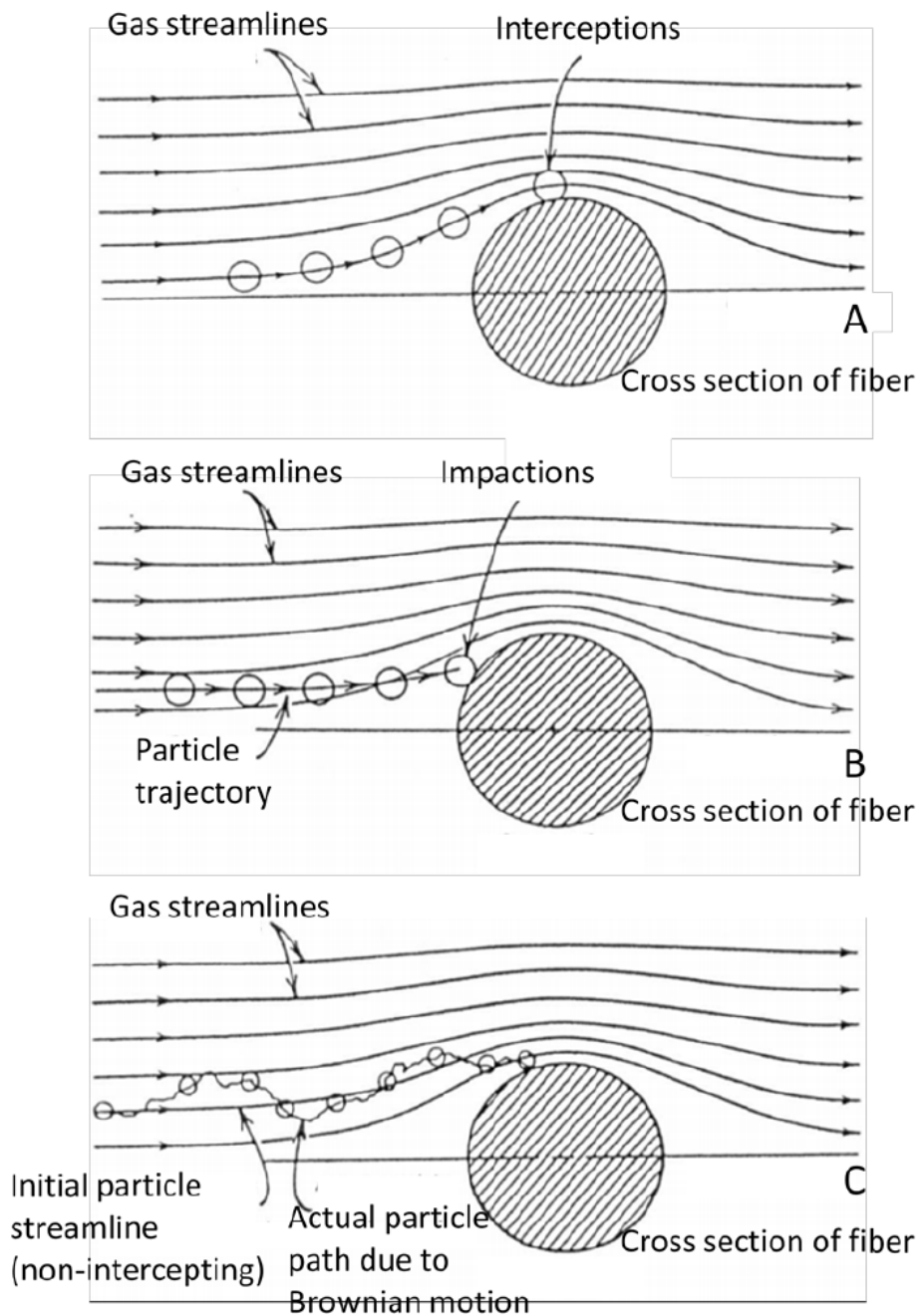
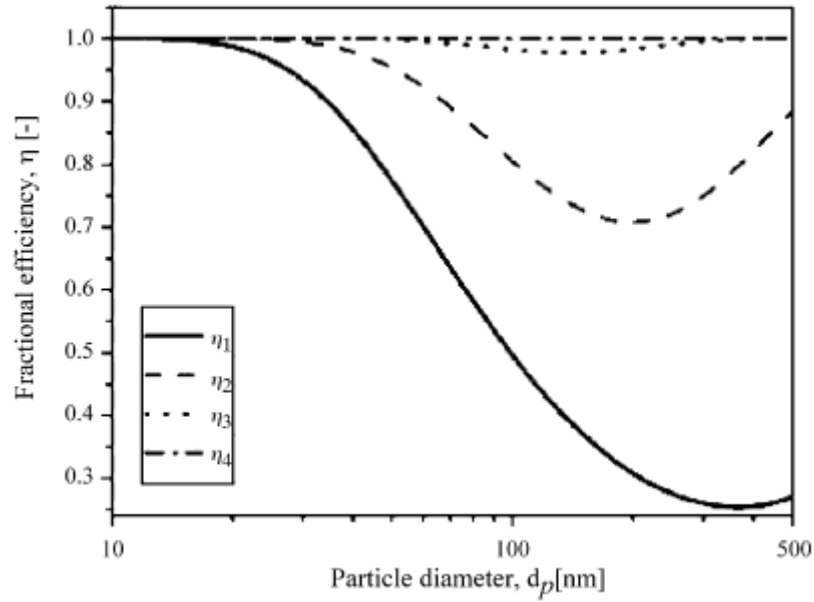


Figure 1-1. Various filtration mechanisms in action in collecting aerosolized particles by a single fiber. The methods are A) Interception, B) Inertial Impaction and C) Diffusion. Reprinted from Hinds, W.C., *Aerosol Technology*, 1999. John Wiley and Sons Inc., pp – 192-194. (Reprinted with permission.)



Structural parameters of filters^a

S.N.	Filter number	Thickness (mm)	Fiber diameter (μm)	Solidity (dimensionless)	Basis weight (g/m^2)	Filter specific area (m^2/m^3)
1	1	3	10	0.1	273	0.4×10^5
2	2	1	2	0.05	45.5	1.0×10^5
3	3	1	0.7	0.02	18.2	1.14×10^5
4	4	0.2	0.1	0.005	0.91	2.0×10^5

Figure 1- 2. Calculated fractional collection efficiency for particulates of different sizes. In conjunction with the information on the Filters, it is evident that the Efficiency depends on Fiber Diameter^[15, 16]. Reprinted from A. Podgórski, A. Balazy, L. Gradon, *Chemical Engineering Science*, **2006**, 61, 6804, with permission from Elsevier.

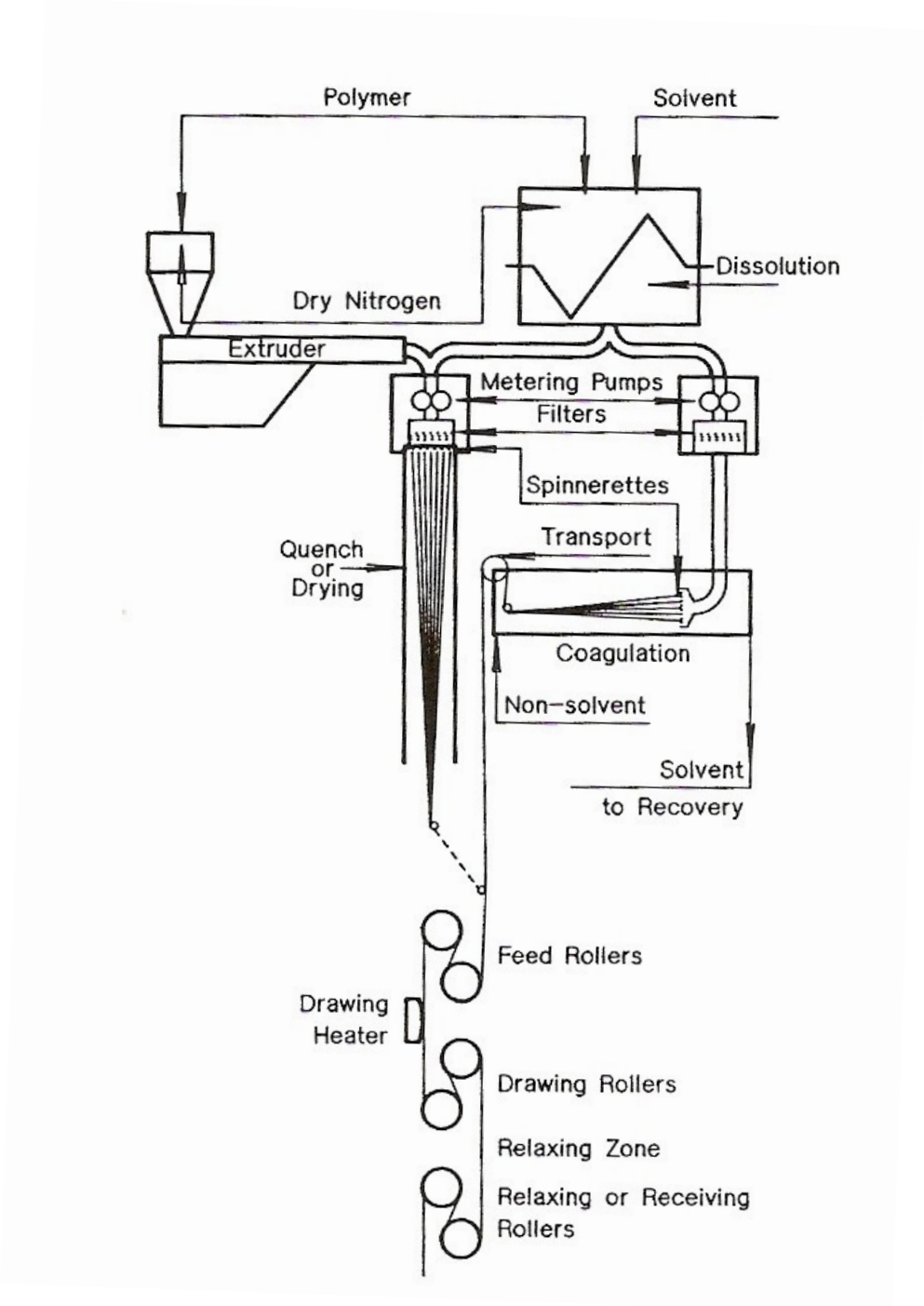


Figure 1-3. Schematic diagram of conventional fiber processing using wet/dry/melt spinning technology^[22]. Reprinted from Z. K. Walczak, *Processes of Fiber Formation*, 1/e ed., **2002**, pp. 1, with permission from Elsevier.

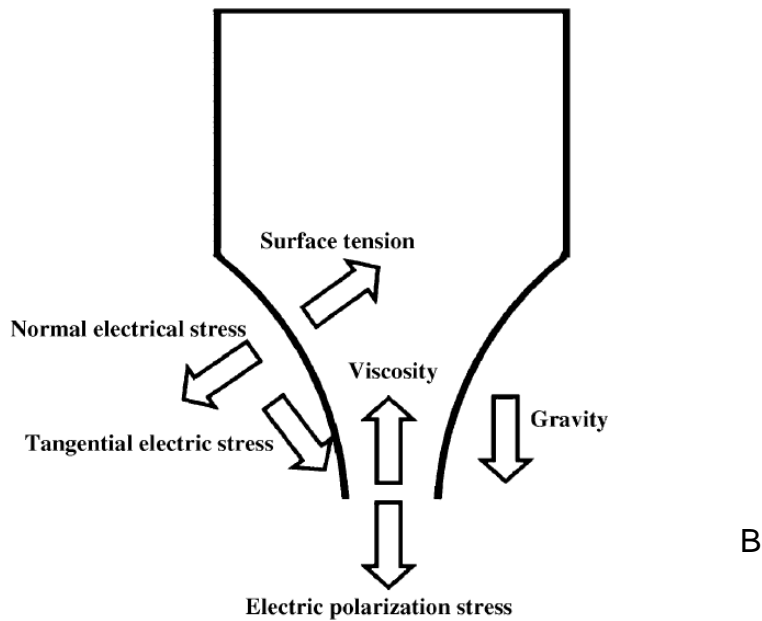
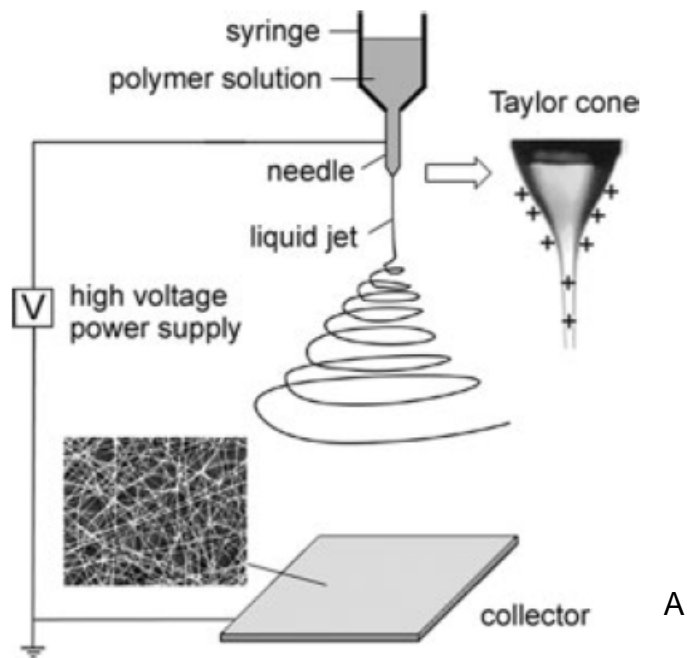


Figure 1-4. Schematic diagram of electrospinning set-up. A) Set-up used in vertical configuration^[28]. B) The various forces in equilibrium forming the Taylor cone^[24]. Image A is reprinted from D. Li, Y. Xia, *Advanced Materials* **2004**, 16, 1151, with permission from Elsevier. Image B is reprinted from W. Sigmund, J. Yuh, H. Park, V. Maneeratana, G. Pyrgiotakis, A. Daga, J. Taylor, J. C. Nino, *Journal of the American Ceramic Society* **2006**, 89, 395, with permission from John Wiley and Sons.

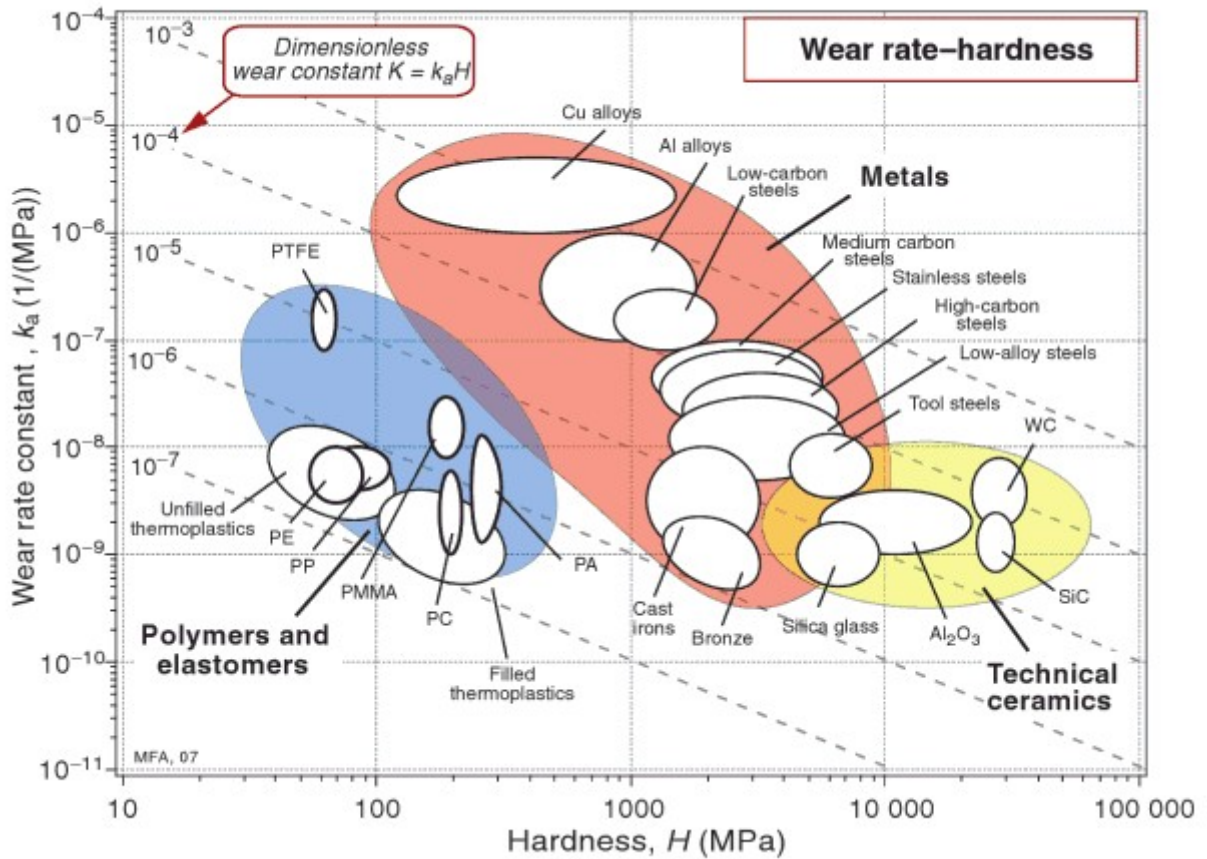


Figure 1-5. Ashby chart for wear rate constant vs hardness for various material classes^[35]. Reprinted from H. S. Michael Ashby, David Cebon, *Materials: engineering, science, processing and design*, Butterworth-Heinemann, 2/e, 2009, pp 231, with permission from Elsevier.

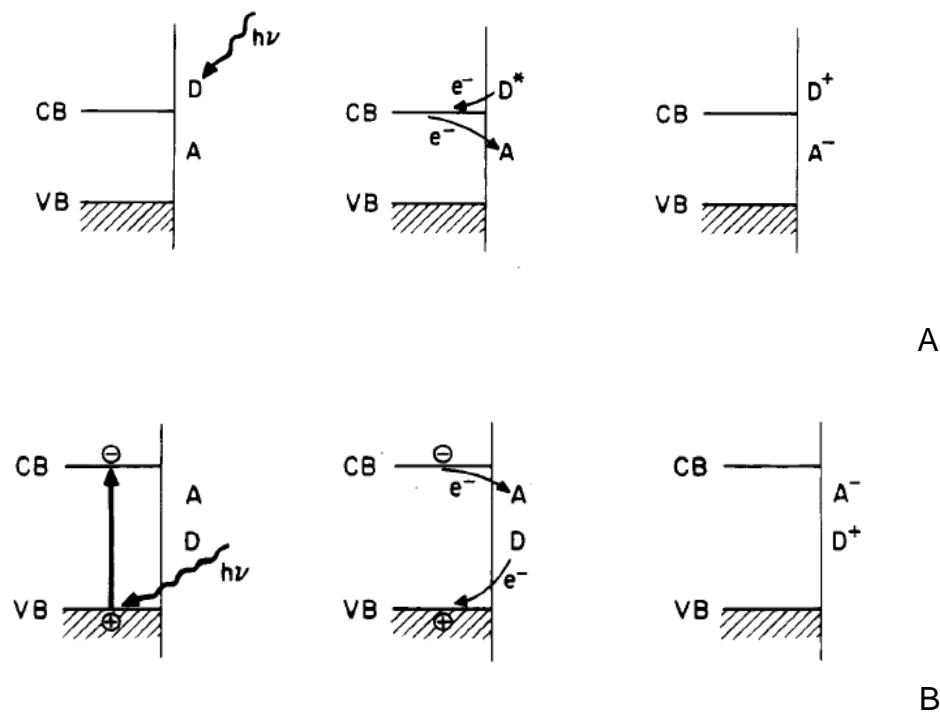


Figure 1-6. Schematics of the photocatalytic reaction process. A) Catalyzed photoreaction. B) Sensitized photoreaction^[46, 47]. Reprinted with permission from A. L. Linsebigler, G. Q. Lu, J. T. Yates, *Chemical Reviews* **1995**, 95, 735. Copyright American Chemical Society.

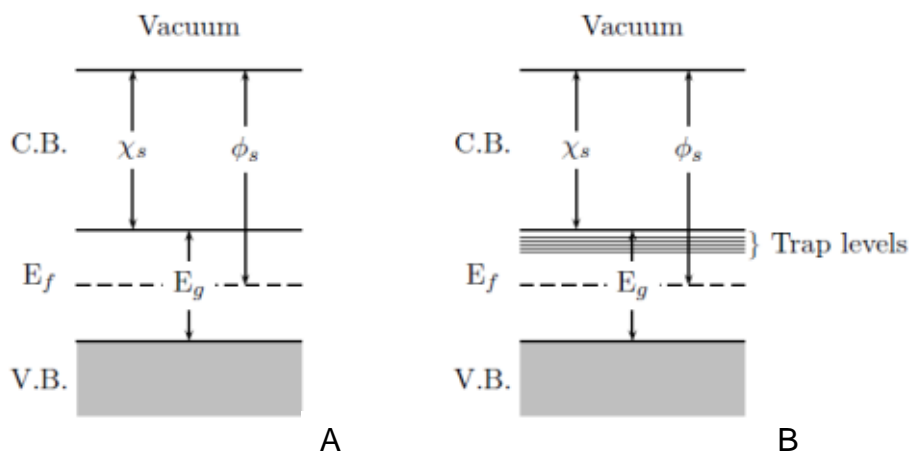
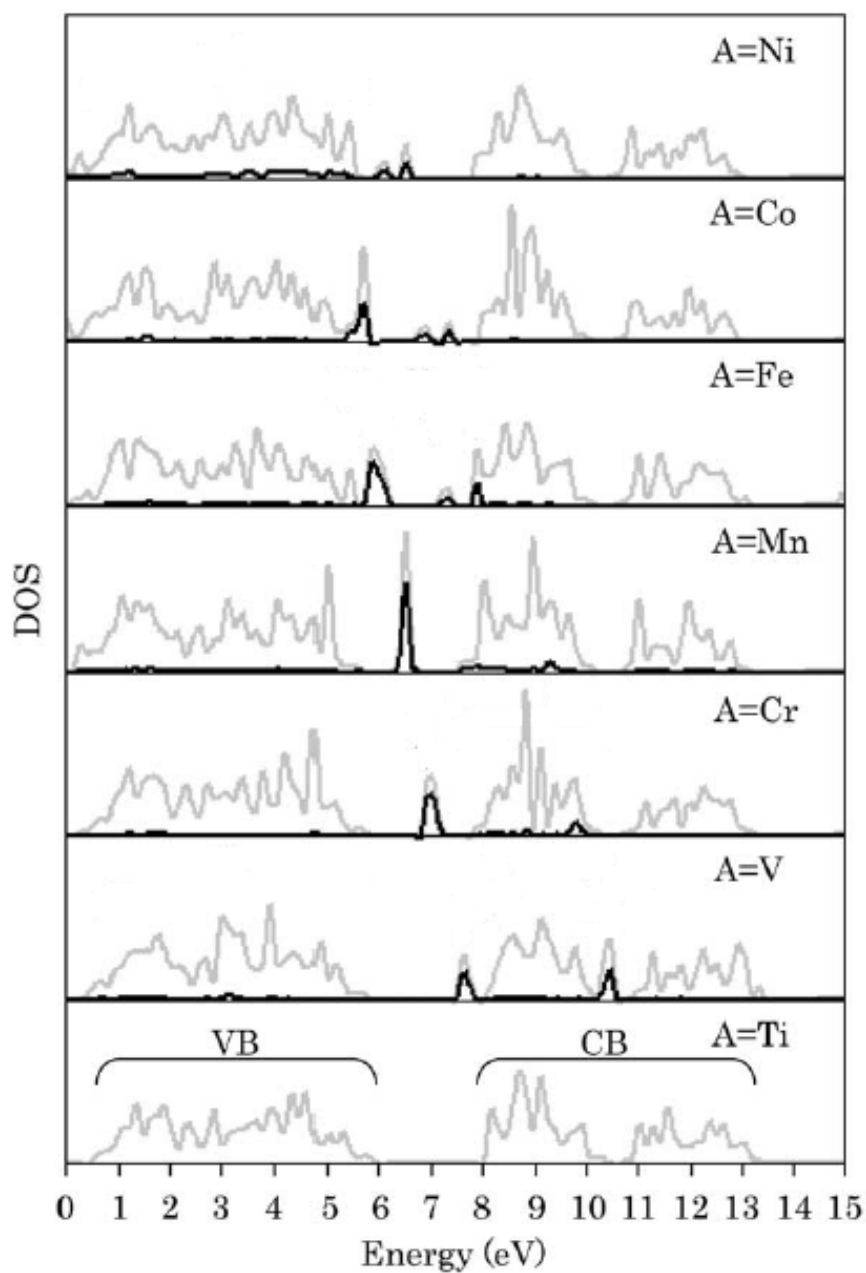
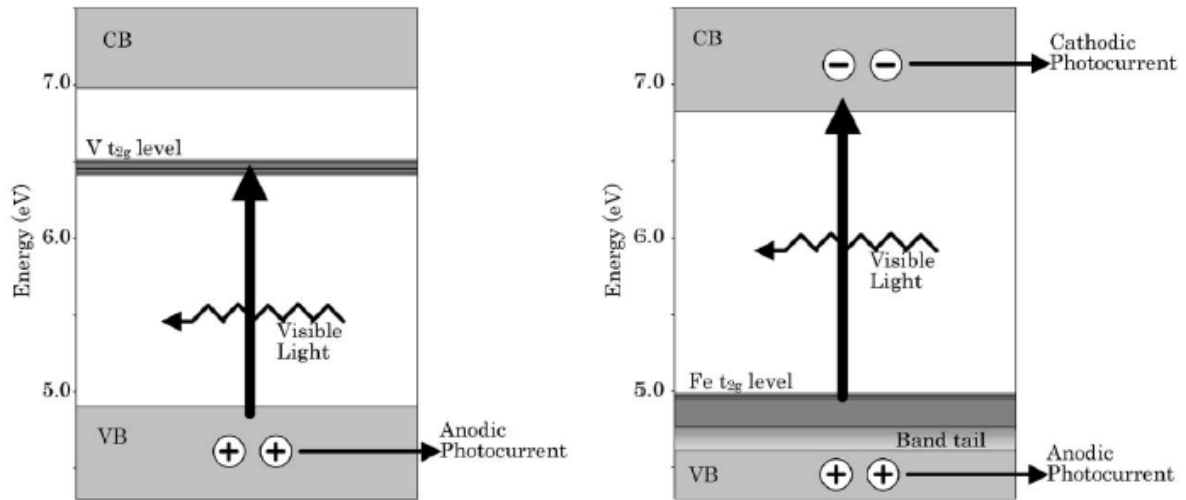


Figure 1-7. Effect of doping transition metals on electronic band structure in TiO_2 . A) Band structure of TiO_2 before doping with transition metal ion. (B) Band structure of TiO_2 after doping with transition metal ion. E_g is the band gap^[45]. This illustration specifically shows electron traps. Creation of hole traps is also possible^[59, 61]. Such energy levels are formed close to the valence band. Reprinted with permission from Titania carbon nanotube composites for enhanced photocatalysis, G. Pyrgiotakis, 2006.

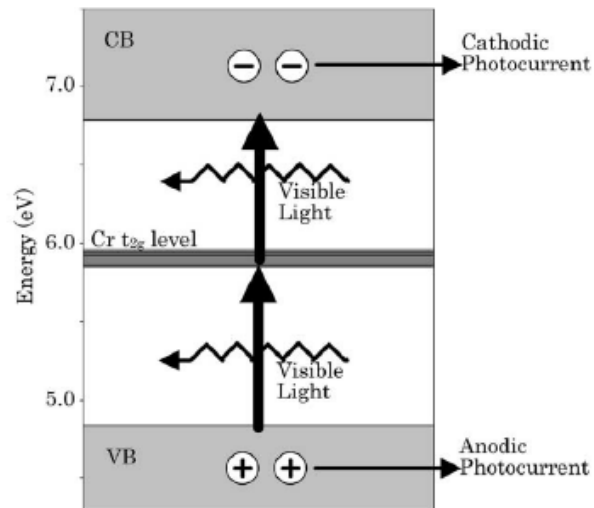


A

Figure 1-8. Influence of atomic number on the effect of doping transition metals on the electron band structure of TiO₂. A) Density of States (DOS) diagram for TiO₂ doped with transitional metal A^[44]. The lighter line represents the total DOS and the darker line represents the DOS of the dopant metal. B) The process of photoexcitation of electrons under visible light irradiation in TiO₂ doped with transitional metals – vanadium, iron and chromium^[44]. Reprinted from T. Umebayashi, T. Yamaki, H. Itoh, K. Asai, *Journal of Physics and Chemistry of Solids* **2002**, 63, 1909, with permission from Elsevier.



(c)



B

Figure 1-8. Continued.

CHAPTER 2 EXPERIMENTAL METHODS

2.1 Preparation of Aqueous TiO₂-SiO₂ Hybrid Sol

Since electrospinning has been selected as the technique for processing fibers in the body of work described in this dissertation, a sol has been prepared for the purpose. As previously mentioned in the background section, ethanol based TiO₂ sols are not chemically stable and titania starts precipitating within hours. Apart from this, heat treated titania fibers have coarse grains depending on the heat treatment temperature. Since silica has a crystallization temperature of around 1500°C, it remains amorphous when heat treated at 500°C, the temperature that is required for crystallization of titania^[42]. This can produce an amorphous SiO₂ matrix. The whole method of preparing the sol can be illustrated by the diagram in Figure 2-1. The synthesis involves preparation of two separate sols – sol A and sol B and then they are mixed homogeneously to form the hybrid sol. In the first step 0.5 ml of HNO₃ (nitric acid concentrate, 1N, Fisher Chemical) is added to 99.5 ml of deionized water to modify the pH level of water to approximately 2.3 (0.005N). This is the common starting ingredient for both the sols. To make sol A, 3 ml of H₂O (pH modified to 2.3) is first added to 18.386 ml of 3-glycidoxypropyltrimethoxysilane (99.5% Acros) (GPTMS). The mixture is stirred for 10 – 20 minutes with a mechanical stirrer. Finally 28.476 ml of titanium (iv) n-butoxide (99%, Acros) (TB) is added to the mixture and stirred for 1 hour to obtain sol A. Preparation of sol B is started by adding 18.386 ml of 3-glycidoxypropyltrimethoxysilane (99.5%, Acros) to 66 ml H₂O (pH modified to 2.3) and stirring for 2 hours. 7.379 ml of tetraethyl orthosilicate (98%, Acros) (TEOS) is added to the mixture and stirred for 2

hours to prepare sol B. Finally 49.862 ml of sol A is added to 91.765 ml of sol B and stirred for 2 hours to obtain the aqueous $\text{TiO}_2\text{-SiO}_2$ sol.

The preparation of sol involves hydrolysis and condensation for both sol A and sol B. Detailed discussion of the reactions occurring during the process are given in another section. The final resultant sol has such a composition that after the heat treatment, the electrospun fibers have a composition of $\text{TiO}_2\text{:SiO}_2$ molar ratio of 1:3. Unlike ethanol based TiO_2 sols, the aqueous $\text{TiO}_2\text{-SiO}_2$ hybrid sol can be stored for several months, even in the presence of air. This stability has been attributed to the formation of Ti-O-Si bonds which inhibit formation and precipitation of TiO_2 . This has been explained in further details in a later section.

2.2 Electrospinning of Ceramic Fibers

To the $\text{TiO}_2\text{-SiO}_2$ sol, prepared according to the way mentioned in the previous section, Polyvinylpyrrolidone (PVP) having a molecular weight of 1.3×10^6 was added to aid the electrospinning process. This sol, with the polymeric aid dissolved in it, was filled in a 5 ml BD syringe. A 15 gauge unbeveled needle (Jensen Global) with a nominal inner diameter of 1.372 mm was attached to the syringe. While the needle diameter does not appear in the electrospinning equation it still plays an important role. Depending on the polymer content and the solvent used the sol tends to clog finer needles. Because of this a larger gauge diameter is more appropriate for higher polymer content and more volatile solvent. The syringe containing the aqueous sol was attached to a syringe pump and electrospun in vertical configuration. Vertical configuration was used since in this case the gravity pulls the fiber in the same direction as the electrostatic field. In the horizontal configuration the pull due to gravitational energy is perpendicular to the direction of the electrostatic field. Because of this reason

the collector distance from the syringe needle has a significant influence on the position and size of the collection area in the horizontal configuration. A vertical set-up is ideal in avoiding any such influence. From a purely technical perspective vertical set-up is known to result in a flow rate which is in excess to the desired rate. This sometimes leads to formation of beads or even worse - formation of just droplets due to Rayleigh instability. However the consistency of the $\text{TiO}_2\text{-SiO}_2$ aqueous sol with dissolved PVP polymeric aid was such that no such excess flow was observed. The syringe pump used can control the flow rate to the precision of 0.001 ml/h. The flow rate was varied in the course of the research to modify the fiber diameter. Figure 2-2 shows the experimental set-up used during the electrospinning process.

Apart from fiber diameter, the quality of the fibers obtained through the process is also important. Beads may form when Rayleigh instability, as described in details in the background section, dominates over the non-axisymmetric whipping instability. Such beads are undesirable from the perspective of mechanical strength. They also make the air flow through the fibermat filter media complicated and unpredictable. The theory based on the drag force caused by a single fiber cannot be applied for such fibers and so fibermats with such fibers cannot be used for testing the hypothesis that fibermats with finer fibers have lower pressure drop and higher quality factor. Thus detailed imaging using Scanning and Transmission Electron Microscopy was carried out on the electrospun fibers. The various measures which were taken to modify the fiber diameter and the heat treatment are explained in details in the next few subsections.

2.2.1 Modification of Fiber Diameter

As has been discussed in details in the background section, the drag force and in turn the pressure drop decreases with decrease in fiber diameter. However this is a

theory based on a single fiber interacting with air. This makes it very important to study the filtration properties of fibermats as a function of fiber diameter. Several parameters were varied to this effect. To better appreciate the work it is worth revisiting the equation on terminal diameter in electrospinning process.

$$h_t = \left(\gamma \bar{\epsilon} \frac{Q^2}{I^2} \frac{2}{\pi(2 \ln \chi - 3)} \right)^{1/3} \quad (2-1)$$

where Q is flow rate, γ is surface tension of the sol, I is the current flowing through the jet. These are the parameters which can be used to vary the fiber diameter.

The first parameter that has been varied in an attempt to reduce fiber diameter is the electrostatic field strength^[24]. Terminal thickness of the electrospun jet is inversely proportional to electric field strength and hence decreases with increase in electric field strength. The electrostatic potential gradients used in the research are 0.5 kV/cm and 1 kV/cm.

While a viscous enough ceramic sol can be electrospun as it as^[74], most ceramic sols need polymer to aid in the electrospinning process. The polymeric chains in the system entangle with each other and form the fiber. Polyvinylpyrrolidone (PVP), having a molecular weight of 1.3×10^6 , was used throughout the research to aid the electrospinning process. Polymer can store charge when the electric field is applied. So increase in the polymer content increases the charge content in the sol, apart from an increase in the number of polymer molecules that are entangled with each other to form a fiber. An increase in the polymer content of electrospun fibers also means an increase in the volume proportion of material that is burnt off during the heat treatment process and an increase in percentage reduction of fiber diameter after heat treatment. While

the increase in the charge content and the volume percentage that is burnt off during the heat treatment leads to a reduction in fiber diameter, the increase in chain entanglement leads to an increase in fiber diameter. Keeping this background in perspective, the amount of PVP added was varied during the research.

Finally, in course of the research, surface tension was varied by adding ethanol in 1:1 volume ratio to the aqueous hybrid sol. When added to water, ethanol is known to reduce surface tension significantly. Surface energy of water decreases by more than 60% when 50 mass% ethanol is dissolved in it^[75].

2.2.2 Heat Treatment

Complete crystallization accompanied by complete burnout of PVP can be achieved at 500°C for pure TiO₂ fibers^[29]. But Ti-O-Si bonds exist in the hybrid sol and the electrospun fibers. This bond inhibits the crystallization of TiO₂^[76]. Previous research suggests that the crystallization process starts above 800°C^[77]. The advantages of having amorphous fibers over crystallized fibers have been described in the background section and would be detailed further in a later section. So in order to maintain the amorphous structure but at the same time make sure that all the polymeric aid are burnt off, heat treatment was carried out at 600°C for 3 hours in air. A well ventilated box furnace was used for this purpose. During heat treatment the electrospun fibermats warp onto themselves and become unusable as filters and so they were heat treated in between two silicon wafers to prevent this. Figure 2-3 illustrates the XRD patterns of TiO₂-SiO₂ heat treated at several temperatures as observed in previous research.

2.3 Preparation and Electrospinning of Doped Titania Sol

2.3.1 Preparation of Titania Sol

As has been discussed in details in the background section, in an environment where sources of energy are limited, it is of considerable practical interest to have photocatalytically active filter media which can be cleaned either by exposing to ultra violet radiation and better yet visible light. The primary focus in this part of the research is to develop and study photocatalytically active fibers. Since titania is a commonly used photocatalytic material, this gives a baseline to compare the photocatalytic activities of doped materials that have been synthesized in an attempt to enhance the photocatalytic activity.

A sol based on ethanol was prepared since titanium alkoxides, which are commonly used as precursors to TiO_2 , readily hydrolyzes and precipitates within a few seconds in presence of water. 3 ml of titanium butoxide was added to a solution of 3 ml of ethanol and 3 ml of glacial acetic acid. The mixture is mechanically stirred for 1 hour to obtain the final titania sol. Acetic acid is added to stabilize the sol and slow down the precipitation process considerably.

2.3.2 Addition and Electrospinning of Niobium Doped Titania Sol

Sol-gel route was selected to dope the titania sol, prepared in the way described above, with niobium. Niobium ethoxide (99.95%, Thermo Fisher) was used for the purpose. Calculated amount of niobium ethoxide was added to produce sols containing 2.5 at%, 5 at% and 10 at% of Nb. Table 2-1 lays out the exact amount of niobium ethoxide added to achieve desired dopant levels. To ensure that the sol is homogeneous it is mechanically stirred for 1 hour at room temperature. Another important factor that has to be considered is that niobium ethoxide is prone to hydrolysis

in presence of the moisture present in air. Because of this care has been taken to minimize the exposure time of niobium ethoxide to air.

It is worth mentioning that the shelf life of the Nb-doped TiO₂ sol is significantly lower than the aqueous TiO₂-SiO₂ sol. It must be electrospun within 2 days after synthesis, otherwise precipitates starts forming – both titania sol and niobium ethoxide being prone to hydrolysis.

The niobium doped titania sols were electrospun using a vertical set-up as described in section 2.2. However there are certain specific modifications made for electrospinning the doped sols. 4% w/v polyvinylpyrrolidone (PVP) was added to the Nb-doped titania sol and stirred for 1 hour before electrospinning. The same quantity of polymer aid was added irrespective of the dopant level. The flow rate and electric field strength were kept at 0.6 ml/h and 1 kV/cm respectively, for all the Nb-doped titania sol samples. These measures help eliminate complications in interpretations as much as possible and provide the opportunity to focus on the effect of dopant concentration on the photocatalytic activity of titania fibers.

The collector used in case of doped titania samples was slightly different from that used for pure titania sol. An activated carbon fiber (ACF) fiber mat was placed on top of the aluminum foil connected with the terminal. When fibers come in contact with aluminum foil they transfer stored electrostatic charge. However unlike aluminum foil, ACF fiber mat has low electrical conductivity. Thus when collected over ACF fiber mats the charge stored in the fibers cannot be dissipated as easily and the fibers deposited on the collector repel each other. This fact has been used to inhibit fusion of fibers while

they are still drying, improving the mechanical properties. This would be discussed in more details in a later section.

2.4 Determination of Filtration Properties

The standard used for designing the experiment is based on the Department of Energy (DOE) standard^[7] for HEPA filters. The filtration properties were measured for 300 nm particles at a face velocity of 4.1 liters per minute. The experimental procedure would be laid out in further details in the next few paragraphs.

During the course of the research TiO₂-SiO₂ fibermats, in particular, were tested for filtration properties. Even though the fibermats are mechanically robust and flexible and are easy to handle, they are not strong enough to be held tightly in the filtration testing fixture. Because of this reason, the fibermats were sandwiched between two ACF fibermats (ACF, American Kynol, Inc., NY). The fibermats were cut into circles with cross-sectional diameter of 47 mm. The sandwiched fibermat was fitted snugly inside the fixture as shown in Figure 2-4. The filtration testing set-up can be broadly divided into three parts – aerosolized particle generation unit, the filter and finally the particle counter and analyzer. An attached pressure gauge measures the pressure drop across the filter.

As has been previously described in the background section, the most penetrating particle size for fiber based filter media is in the range from 500 nm to 100 nm depending on the fiber diameter and hence for high efficiency particulate air (HEPA) filters it is recommended to perform the tests for 300 nm particles. A suspension of spherical polystyrene latex (PSL) particles having a diameter of 0.29 μm (<= 3% CV, Thermo Scientific, 5030A) was prepared in deionized water by adding 2g/liter of the PSL particles. This aqueous suspension was aerosolized in a six-jet Collision nebulizer

(Model CN25, BGI Inc., MA). This aerosol was dried inside a dilution drier as shown in the Figure 2-4. This step is performed so that the water on the surface of the PSL particles maybe evaporated and the air stream would carry particles which have a very narrow size distribution around 0.29 μm .

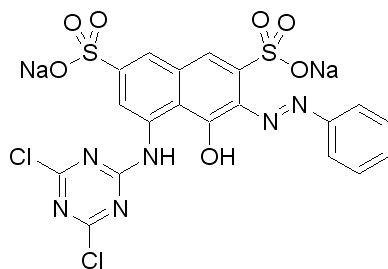
It is in the second part of the set-up where the filtration takes place. As mentioned previously, the fibermat is sandwiched between two ACF fibermats for support. The face velocity of the air stream with aerosolized particles is 5.3 cm/s - corresponding to 4.1 liters per minute (LPM). The pressure drop across the filter is measured by a Magnehelic differential pressure gauge (Model 2010, Dwyer Instruments, IN).

The final stage of the experiment involves a scanning mobile particle counter (SMPS) (Model 3936, TSI Inc., MN) which measures the number of particles in an air stream and also shows the distribution of particles. This information was used to calculate the collection efficiency of the particles.

Fibermats with different average fiber diameter and thickness were tested using this set-up and details of such particulars including the results will be discussed in a later section.

2.5 Determination of Photocatalytic Properties

The photocatalytic properties of niobium doped fibermats were tested in an aqueous medium. The fibermats were mixed with ethanol (200 proof, Fisher Scientific) and ground up using a mortar pestle. The suspension of ground fibers in ethanol is placed on a heating plate and heated at around 70°C to evaporate the ethanol and obtain dry ground fibers. To 20 ml of deionized water 1 ml of Brilliant Procion Red MX-5B pigment solution having a concentration of 10^{-3} g/ml was added. The pigment has the following chemical structure:



Procion Red MX-5B was chosen due to the presence of three benzene rings and one triazine ring all of which make the dye molecule especially stable compared to dyes which have fewer rings ^[78]. This is important since it ensures that the pH, temperature and other factors can get stabilized in the system before the degradation of the dye is over. The dried ground fibers were added to the pigment solution at a concentration of 0.00048 mg/ml of solution.

A magnetic stirrer was placed in each glass vial containing the sample and each sample was mechanically stirred continuously during the exposure. As mentioned previously, the photocatalytic reaction occurs on the surface and hence new water molecules must be transported to the surface for the creation of oxidizing and reducing species. Stirring the sample during the experiment ensures that newly created species are removed from the surface more quickly than possible by conventional diffusion. In each batch only two samples were placed inside the chamber. This ensures that the vials would not cast any shadow on each other and all the samples receive equal amount of radiation. All samples were exposed for 8 h to UVB.

After exposure for the specific time, an UV/Vis Perkin-Elmer Lambda 800 spectrometer was used to perform absorption spectroscopy of the samples for wavelengths between 250 nm and 800 nm. The instrument uses a tungsten halogen bulb in the visible range and a deuterium lamp in the ultraviolet range as source for

electromagnetic radiation. The presence of particles leads to scattering of light and hence very small fraction of light is able to pass through the sample to the detector for the spectroscopy. For this reason, the sample was pulled in a 5 ml BD syringe and then filtered using syringe filter having pore diameter of 1.0 μm to remove the dispersed fibers.

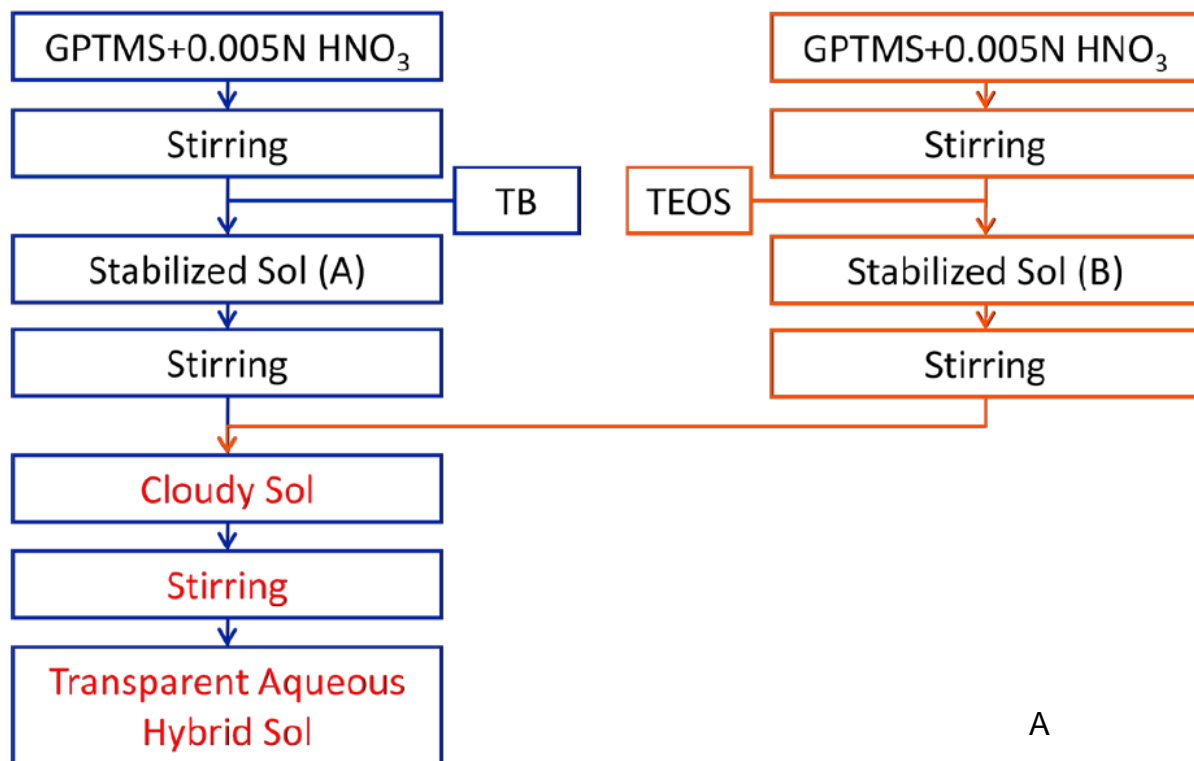
Photocatalytic activity depends on the specific surface area (surface area of a material per unit mass) and materials having larger specific surface area can adsorb more molecules on the surface and shows enhanced photocatalytic activity^[79, 80]. Because of this reason, specific surface area for each sample was measured according to the theory developed by Brunauer, Emmett and Teller, also known as the BET technique. To account for the influence of surface area of the material, the specific area determined from the experiment is used to normalize the absorption spectra. The pore size distribution was also obtained using the Barrett-Joyner-Halenda (BJH) method.

Table 2-1. Addition of niobium ethoxide to titania sol (9 ml)

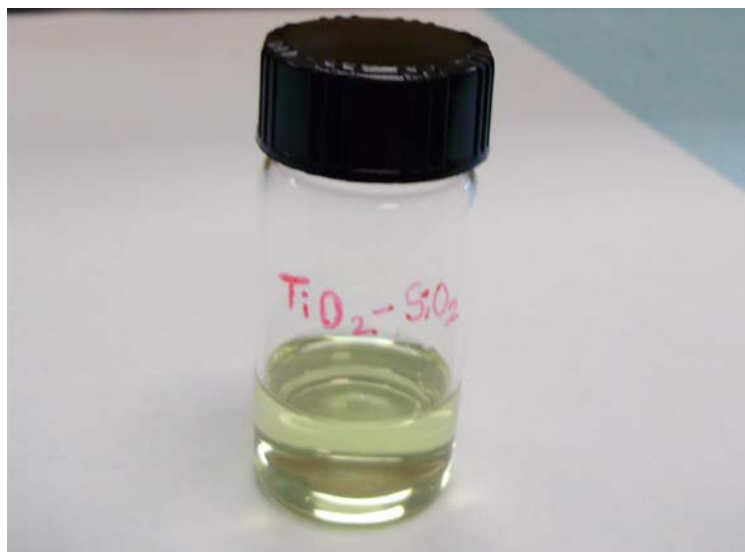
Composition	Volume of niobium ethoxide added
2.5 mol% Nb doped TiO ₂	0.056 ml
5 mol% Nb doped TiO ₂	0.114 ml
10 mol% Nb doped TiO ₂	0.242 ml

Table 2-2. Addition of $\text{Nd}(\text{NO}_3)_3 \cdot 6\text{H}_2\text{O}$ to titania sol (9 ml)

Composition	Mass of $\text{Nd}(\text{NO}_3)_3 \cdot 6\text{H}_2\text{O}$ added
0.5 mole% Nd doped TiO_2	0.0192g
0.75 mole% Nd doped TiO_2	0.0288g
1.0 mole% Nd doped TiO_2	0.0385g
1.25 mole% Nd doped TiO_2	0.0483g
1.5 mole% Nd doped TiO_2	0.0581g
1.75 mole% Nd doped TiO_2	0.0680g
2.0 mole% Nd doped TiO_2	0.0779g
2.5 mole% Nd doped TiO_2	0.0990g
3.0 mole% Nd doped TiO_2	0.1180g



A

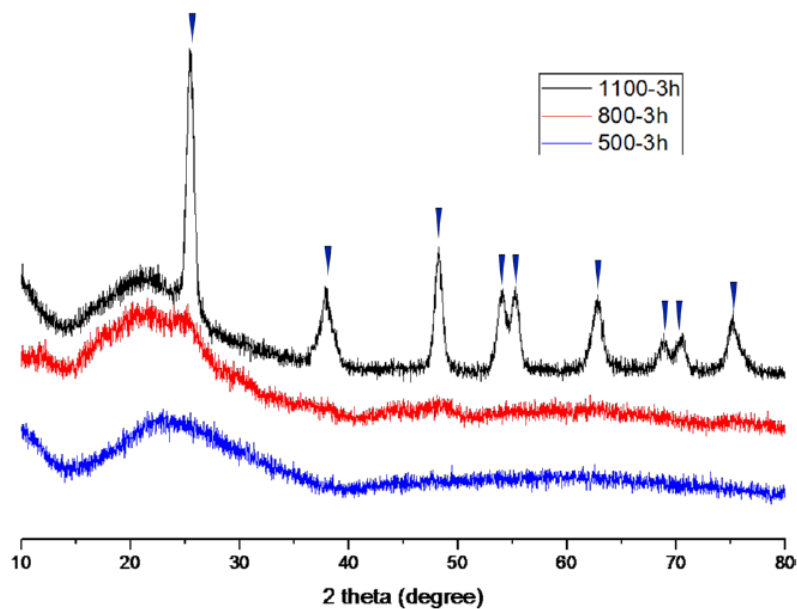


B

Figure 2-1. Processing of $\text{TiO}_2\text{-SiO}_2$ aqueous sol. A) Schematic diagram representing the different steps involved in preparation of the aqueous sol. GPTMS: 3-glycodoxypropyltrimethoxysilane, TEOS: tetraethylorthosilicate, TB: titanium butoxide^[77]. B) $\text{TiO}_2\text{-SiO}_2$ sol stored in presence of air after 5 months. No visible precipitation of titania particles observed. Figure A is reprinted with permission from H. Park, *Electrospinning of Nanofiber for Filtration Media*, 2010.



Figure 2-2. The electrospinning set-up used in electrospinning $\text{TiO}_2\text{-SiO}_2$. A vertical set-up was used throughout the research.



A



B

Figure 2-3. Heat treatment of $\text{TiO}_2\text{-SiO}_2$ fibermat. A) X-ray diffraction pattern for different $\text{TiO}_2\text{-SiO}_2$ samples heat treated at 500°C, 800°C and 1100°C for 3 hours from previous research findings^[77]. Crystallization just starts when heat treated at 800°C for 3 hours. This has been used to plan heat treatment temperature. B) Box furnace used for heat treating samples. Sample was placed at the same level as the thermocouple to ensure that the effect of thermal gradient of the furnace on heat treatment is minimal. Figure A is reprinted with permission from H. Park, *Electrospinning of Nanofiber for Filtration Media*, 2010.

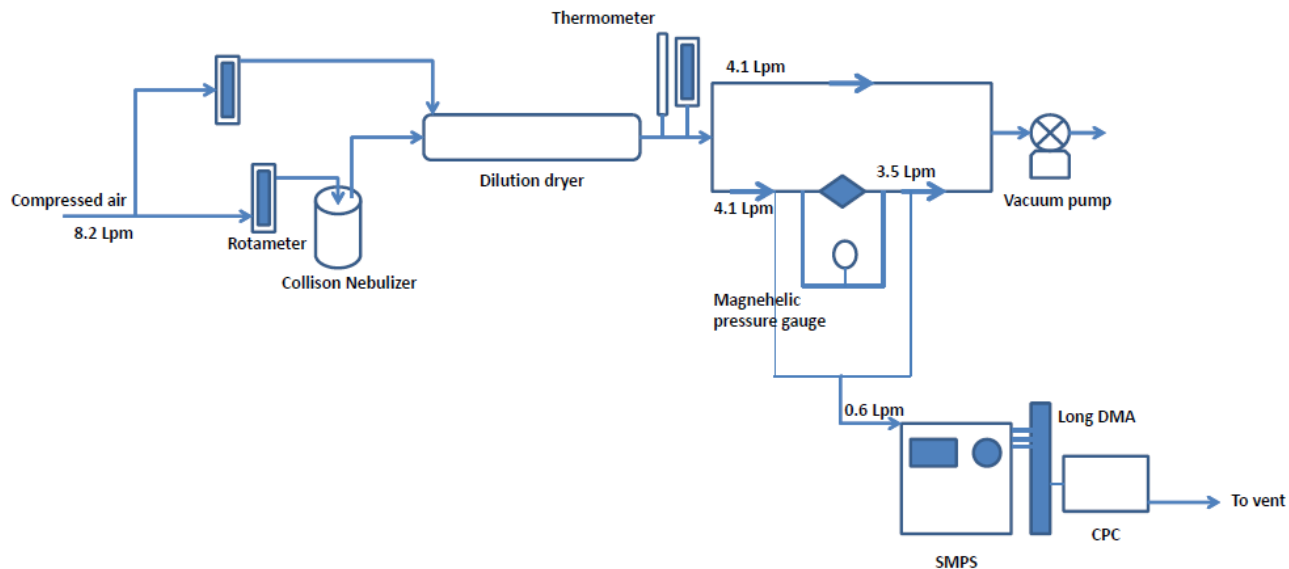


Figure 2-4. The filtration testing set-up used for determining the filtration properties of electrospun $\text{TiO}_2\text{-SiO}_2$ fibermats.

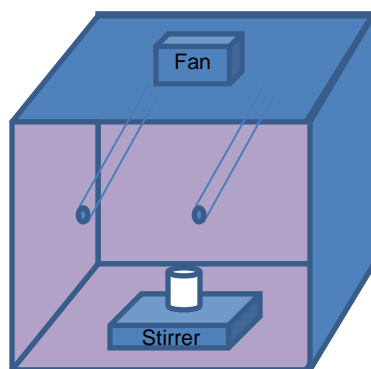


Figure 2-5. Chamber used to expose sample to ultra violet or visible light radiation. During the exposure the sample was mechanically stirred to reduce the influence of mass transport of dye molecule on the reaction rate. All samples were exposed to same condition for comparison.

CHAPTER 3
RESULTS AND DISCUSSIONS

3.1 Effect of Electrospinning Conditions on Fiber Morphology, Crystal Structure and Mechanical Properties of TiO₂-SiO₂ Fibers

The main focus of the research has always been to develop a fibremat based filter medium which can be used in-habitat in lunar and Martian environment. The ideal characteristics which are desired as far as application in filtration technology is concerned are narrow fiber size distribution, uniform fiber thickness along the length and minimal bead formation. Various parameters in the electrospinning process were varied to obtain this desired objective. While presence of beads and inhomogeneity in fiber diameter may very well affect the filtration properties but study of how such morphological features influence filtration is beyond the scope of this research. In the case of this research, the influence of processing parameters on the morphology, crystal structure and mechanical properties of the fibers were of interest.

As has been discussed previously, the various parameters that have been modified during the course of the research are a) electric field strength, b) concentration of polymeric aid added and c) flow rate. In addition, the surface tension of the sol was also modified by adding ethanol. All these parameters appear in the equation derived for terminal diameter of the jet (h_t) as expressed in Eq. 3-1.

$$h_t = \left(\gamma \bar{\epsilon} \frac{Q^2}{I^2} \frac{2}{\pi(2 \ln \chi - 3)} \right)^{1/3} \quad (3-1)$$

From the equation it appears that fiber diameter is directly related to the surface energy and flow rate of the sol and is inversely related to the electric field strength. Keeping this theory in mind it would be interesting to tabulate all the various attempts that has been

made to electrospin fibers from the sol – with all the various parameters shown next to them.

For all samples in Table 3-1, other parameters such as flow rate, electric field strength and collector distance are kept constant. While collector distance does not appear in any equation related to the terminal diameter of jet, there are reasons which make it an important factor. The terminal diameter is achieved when the repulsive force due to surface charge is compensated by surface tension^[24]. Enough separation between needle and the collector must be present to ensure the jet reaches this stage. Consequently 25 cm has been used as the collector distance throughout the research, which is much larger than conventionally used collector distance^[29]. Larger collection distance also helps in deposition of fibers evenly over a larger area^[81]. As can be observed from the data the fiber diameter increases with increase in the PVP content used. However no such relationship is observed in the equation for terminal jet diameter in an electrospinning process. The most probable reason behind the observed phenomena is that in presence of higher polymer concentration, the number of chain entanglements in the jet increases. When very low quantity of polymer (between 0.4% w/v and 0.75% w/v) is used, there is a tendency to form beads and the fibers produced exhibit a very large range in terms of diameter. This may be explained by a qualitative analysis of the various types of instabilities acting on such a system. When the amount of dissolved polymer molecule is lower, the amount of surface charge stored by the system also decreases. Because of this, Rayleigh instability becomes dominant over electrically induced non-axisymmetric whipping instability. Since the electrically induced non-axisymmetric instability is the reason behind formation of fibers and reduction of

their diameters, increase in the contribution of Rayleigh instability results in bead formation. Secondly, in the absence of molecular chain entanglements from long chain polymer molecules, multiple jets emerge from the needle-end, instead of a steady single jet. This results in huge deviation in terms of fiber diameter. The morphological features are readily visible in Figure 3-1. The figure also shows a plot representing the average fiber diameter of synthesized $\text{TiO}_2\text{-SiO}_2$ fibers as a function of polymer content used to aid electrospinning. It must be noted that the fiber diameter that has been discussed until now in this section is the diameter of as-processed fibers before heat treatment. The fibers must be heat treated before the polymeric aid is burnt out and all that is left is inorganic ceramic fiber mat. Since the initial fiber diameter before heat treatment is reflective of the chain entanglement of the polymer molecules, it's not predictive of the final diameter after heat treatment.

Since chain entanglement of polymer molecules is so important, the subject of selection of PVP with molecular weight (M_w) of 1.3×10^6 warrants a little commentary. Attempts were made earlier in the research to electrospin fiber with PVP having M_w of 630000. It was observed that even though it is possible to electrospin such a sol but the amount of polymer and flow rate required are higher. Also when such a polymer with low molecular weight is used, there is a greater tendency to form beads. So PVP with a higher molecular weight of 1.3×10^6 was used for the sake of simplifying the process of interpreting the results. The reason for not choosing a molecular weight higher than 1.3×10^6 is that such an increase would result in increase in fiber diameter. Heat treatment was carried out at 600°C for 3 hour in atmosphere and fiber diameters measured and are tabulated in Table 3-2.

As mentioned in Table 3-1, when $\text{TiO}_2\text{-SiO}_2$ sol was electrospun with 0.4 w/v percent PVP, no fiber was observed and the corresponding SEM image is predominantly that of droplets, almost reminiscent of electrospraying. The image before the heat treatment is shown in 3-1 A. Figure 3-2 represents the same fiber mat after heat treatment. Upon heat treatment the beads shrink and fibers become more visible.

It is of interest to look at the percentage reduction in fiber diameter after heat treatment and how that varies depending on the polymer content of the electrospinning sol. While fibers electrospun from sol containing high concentration of PVP has more polymer that is burnt off during heat treatment, such increased polymer chain entanglements can trap more $\text{TiO}_2\text{-SiO}_2$ precursor. The reduction in cross section area of a fiber varies depending on which of these two factors is dominant. This is tabulated in Table 3-3.

Ceramic materials, especially nanofibers are extremely brittle^[82]. Until this research we found only three studies, and all by the same research group, where flexible TiO_2 fiber mats were produced^[83-85]. Even $\text{TiO}_2\text{-SiO}_2$ fibers, when the fiber mats were heat treated at 800°C or above^[77], are very brittle and are extremely difficult to handle and almost impossible to use as filtration media. The stress applied by the filtration testing set-up fixture and the air flow is too high for using such fiber mats. However flexible ceramic fiber mats were obtained^[82] when fibers were collected over an aluminum foil over a heating plate maintained at 85°C and then heat treated at 600°C. The fiber mat could be easily bent to a radius of curvature of 3.4 mm. The flexibility is more at certain areas and such small sections can be bent to an even smaller radius of curvature of 1.3 mm. Figure 3-3. A) – C) demonstrates the flexibility of the fiber mat. One

possible reason behind such mechanical properties may be the presence of unburned polymer molecules. However previous research has shown that complete oxidation of PVP takes place when fibers are heat treated at 500°C^[29, 82]. So the influence of polymer chain entanglements on the flexibility can be ruled out. Such high degree of flexibility is unusual for ceramic fiber mats and it is mechanically robust enough for use as filtration media.

In the course of our research, equal volume of TiO₂-SiO₂ aqueous sol was mixed with ethanol (200 proof, Fisher Scientific), to reduce surface energy^[75] and in turn the fiber diameter. In this particular case, 2% w/v PVP (M_w 1.3x10⁶) was added as an electrospinning aid. A comparison of electrospun fibers containing 2% w/v percent of PVP, with and without ethanol is compared in Table 3-4. As is evident, the average fiber diameter decreased by approximately 133% due to the lowering of surface energy of the sol by ethanol. Scanning and Transmission electron microscopy was used to obtain image of the nanofibers. Selected area diffraction of individual fiber heat treated at 600°C showed diffused ring pattern, characteristic of amorphous phase. No grain structure was observed in the images either.

To understand the mechanism in action behind the enhanced flexibility it is important to revisit the topic of toughness in ceramics. As has been mentioned previously in the background section, polycrystalline ceramics have higher fracture toughness than single crystal ceramics, which in turn have higher toughness compared to amorphous ceramics (glass). This is so because, unlike in single crystal ceramic where crack propagates along a preferred plane, in polycrystalline ceramics once a crack is initiated it has to traverse through a larger distance along grain boundaries.

From this perspective amorphous ceramics should be the most brittle since once a crack is formed in such a material, in the absence of any preferred plane, it propagates perpendicular to the surface through the shortest route. However micron sized glass fibers have shown near theoretical strength^[40, 41] when the process of crack initiation is inhibited or the number of crack initiation sites are few. Neither any surface defect nor any grain structure was observed in the SEM and TEM images obtained of the heat treated fibers. A diffused ring pattern was observed in selected area diffraction pattern of individual fibers - indicating an amorphous structure. It is theorized that the reduced number of crack initiation sites in such an amorphous fiber is the reason behind the observed mechanical properties. Figure 3-4. A) and (B) illustrates the fiber morphology of heat treated fibers - electrospun from a 1:1 mixture by volume of aqueous TiO₂-SiO₂ sol with ethanol, and using 2% w/v PVP (M_w 1.3x10⁶) as electrospinning aid.

It is obvious from previous research findings that 500°C is high enough temperature for crystallization of titania and hence presence of crystallized TiO₂ is expected in the images and the selected area diffraction pattern^[29]. This apparent contradictory observation maybe explained by the fact that Ti-O-Si bonds are formed during the synthesis of the sol and such bonds inhibit the crystallization of TiO₂^[76, 82, 86]. During the course of preparing the sol, hydrolysis of 3-glycidoxypropyltrimethoxysilane (GPTMS) occurs in the first step. In the next stage condensation of the hydrolyzed GPTMS takes place with both titanium butoxide and tetraethylorthosilicate (TEOS). It is during the condensation with titanium butoxide that Ti-O-Si bonds are formed with the release of butanol. The hydrolysis and condensation reactions are shown in Figure 3-5. A) and (B) respectively.

A final observation may be mentioned about the heat treated TiO₂-SiO₂ fibers. The TiO₂-SiO₂ fibers maintain their general fibrous morphology even after vigorously ultrasonicated in deionized water for 20 minutes^[82]. In the process they break into shorter filaments few tens of micrometers in length. These short filaments can be used as reinforcements in composite materials. A similar observation was reported in 500µm amorphous silica fiber in a previously published research^[87].

3.2 Filtration Properties of Electrospun Ceramic Fibermat

As has been discussed previously, the terminal jet diameter and in turn the fiber diameter in the electrospinning process depends on several factors such as electric field strength between the needle and the collector, flow rate of the sol and the surface energy (i.e. composition)^[24]. So these parameters were varied to obtain fiber mats with different fiber diameters. The average fiber diameters after heat treatment of the various fiber mats that have been tested for filtration properties are provided in table 3-5.

As expected, there is a general trend showing increase in fiber diameter with increase in the polymer content and flow rate of the sol. However the fiber diameter decreases notably when PVP content is increased from 6.0% w/v to 6.5% w/v, even though flow rate has been increased by 50% in the later. This can be explained by the fact that the amount of material that can be burnt out increases with increase in the amount of polymeric aid used. Also the polymer molecules can store charge in the presence of high electric field. This can explain the reduction in fiber diameter for the sol containing 6.5% w/v PVP. As a side note, it is worth mentioning, that the fibers of the fiber mats used in the filtration tests were smooth with no observable beads in the SEM images. This is important since the hypothesis that pressure drop in fibrous filters decrease with reduction in fiber diameter is based on smooth single fibers. An SEM

image of electrospun $\text{TiO}_2\text{-SiO}_2$ fibers using 6.5% w/v PVP as polymeric aid is shown in Figure 3-6. The density of the fiber mat was obtained using helium pycnometer and has been found to be 2.26 g/cc. Pore size distribution obtained using BJH technique is presented in Figure 3-7. It appears that surface pores having diameter approximately 2.5 nm contribute most to pore area.

As described in details in the experimental methods section, a dispersion of 0.29 μm ($\leq 3\%$ CV) polystyrene latex (PSL) particles is aerosolized in the first stage of the filtration test. It is important to understand that even though the PSL particles were largely monodisperse, aerosolized particles had water droplets attached to them. This results in a much larger size range for aerosolized particles. The set-up has a drying chamber where most of the attached water is evaporated by using a jet of dry air. The size range for aerosolized particles in the original air-stream before it passes through the filter is important. To obtain this data the air-stream with aerosolized particles is allowed to directly enter the scanning mobile particle counter (SMPS) without any filter in the path. Figure 3-8 shows the particle size distribution in the original air-stream. The particles larger than 0.29 μm have water droplets still attached to the PSL particle. The particles much finer than 0.29 μm represent the water droplets created by the nebulizer which are not attached to any PSL particles. The high percentage of particles having 0.29 μm diameter is in the range of most penetrative particle size (MPPS). This ensures that the results obtained from the filtration tests performed using this aerosol give the most conservative values.

The most important parameter in determining filtration properties of a fiber mat is its quality factor given by $Q^{[88, 89]}$ in Eq. 3-2.

$$Q = \frac{\ln\left(\frac{1}{P}\right)}{\Delta p} \quad (3-2)$$

Since this parameter is a ratio of collection efficiency and pressure drop, a fiber mat with higher quality factor can have higher collection efficiency for same amount of pressure drop – thus conserving energy in the process. The relationship between quality factor and fiber diameter is an important one from application perspective. Previous research on the influence of fiber diameter on pressure drop is ambiguous at best. While from the theory a lower pressure drop is expected for finer fibers^[77], increase in pressure drop due to reduction in fiber diameter has also been reported in certain research articles^[15, 89]. Since different fiber mats tested have different mass and thickness, pressure drop has been normalized with respect to mass and thickness for meaningful comparison. Figure 3-9 (A) and (B) show the plot of pressure drop normalized with respect to thickness and mass respectively vs fiber diameter. It may be noticed that both parameters show a decreasing trend with increase in fiber diameter. This apparent contradiction to theory may be explained by the fact that air has to pass through several layers across the thickness of the fiber mat while the theory is based on single fiber consideration. The normalized pressure drop can also be expressed as a function of packing fraction (α) of fibers^[15].

$$\frac{\Delta p}{L} = \frac{64\mu U}{d_F^2} \alpha^2 (1 + 56\alpha^3) \quad (3-3)$$

where μ , U , d_F are the viscosity of air, face velocity and fiber diameter respectively. Packing fraction (α) in turn is a function of fiber diameter^[90] as expressed in Eq. 3-4.

$$\alpha = \left(\frac{\pi}{4}\right) \left(\frac{R_F^2}{R_C^2}\right) \quad (3-4)$$

where R_F is radius of fiber and $2R_C$ is the distance between the centers of two adjacent fibers. After some mathematical consideration it's apparent that packing fraction is proportional to mass/square of filter thickness.

$$\alpha = \left(\frac{\pi}{4}\right) \left(\frac{R_F^2}{R_C^2}\right) \propto \frac{\text{mass}}{\text{thickness}^2} \quad (3-5)$$

Since $\text{mass}/(\text{filter thickness})^2$ decreases with increase in fiber diameter as shown in Figure 3-10, it can be inferred that the corresponding packing fraction also decreases. Thus there is a larger fraction of void area in the fibermats with larger fiber diameter. So less energy is required for air to pass through fibermats with larger fiber diameter. Finally the number of stacked layers per unit thickness in a fibermat decreases with increase in fiber diameter. All these factors together may explain the observed behavior. Figure 3-10 C) compares the normalized pressure drop of present electrospun fibermats with those reported in literature and commercially available HEPA and ULPA filters.

A particular aspect of the data interpretation must be discussed. The fibermats were sandwiched between two supporting ACF fibermats. The ACF fibermats also contribute to the measured pressure drop and Darcy's law^[89] has been used to separate out the contribution arising solely from the ceramic fibermat. According to this law if there are n layers of fibermat then the total pressure drop may be denoted by Eq. 3-6.

$$\Delta p_t = n \cdot \Delta p_a + \Delta p_s \quad (3-6)$$

where subscripts t , a and s stand for total, ACF and structures respectively.

The second important individual factor is the collection efficiency. A filter may be defined as a high efficiency particulate air (HEPA) filter if the collection efficiency is equal to or greater than 99.97% for aerosolized 0.3 μm particles. Figure 3-11 shows a plot of collection efficiency vs average fiber diameter. Within the resolution of our instrument all four fibermats showed 100% collection efficiency for aerosolized 0.29 μm particles. The ACF fibermat supports contribute to the collection efficiency similar to the case of pressure drop. In order to eliminate their contribution and measure the contribution of the ceramic fibermat alone, the penetration factor for each layer may be derived using Eq. 3-7, where total penetration factor is given as the product of penetration factor for all the individual layers^[89, 91] :

$$P_t = P_1 \cdot P_2 \cdot P_3 \dots \quad (3-7)$$

where the subscript t stands for total and p_1, p_2, p_3, \dots stand for the penetration factor for the first, second, third layers and so on respectively.

3.3 Influence of Niobium Dopant on the Morphology, Crystal Structure and Photocatalytic Activity of Electrospun Titania Fiber

Unlike on earth, sources of energy are not abundant in the lunar environment. This makes it important to find novel energy efficient ways to clean the filters and photocatalysis fits the bill perfectly. Such a process can use the solar energy on the lunar surface to clean itself without using any external source of energy. Pure titania as well as titania doped with varying levels of niobium were electrospun. The fiber morphologies of all such fibers were studied and XRD were carried out to study their crystallinity. They are compared for their photocatalytic activity in this section.

As discussed previously in details in the experimental section, TiO_2 sol was prepared by mixing titanium butoxide in a 1:1 volume mixture of ethanol and acetic acid.

Niobium ethoxide was used to dope the sol with niobium. PVP was further added to aid the electrospinning process. It may be recalled that pure titania fiber mats are very brittle after crystallization. Electrospun fibers, while still wet, fuse together and this fusion hinders sliding of the fibers over each other. Part of the brittleness observed in the electrospun ceramic fiber mats is because of this fusion, apart from the contribution of the ease of crack initiation in crystallized fibers. To reduce this type of fusion two modifications have been made in the collector. Firstly, the collector is maintained at a temperature of around 85°C, which is high enough for fast drying of ethanol used as solvent in the sol. Secondly, but more importantly, an ACF fiber mat is placed on the aluminum foil which in turn is connected to the ground. The electric field required for the electrospinning is in between the needle and the grounded aluminum foil. But since ACF fiber mats have very low electrical conductivity, the charged fibers deposited on the ACF surface cannot transfer their charge as easily and efficiently as possible in case of a metallic collector like aluminum foil. Similarly charged fibers deposited on the ACF repel each other and this decreases the probability of contact between fibers. These two factors in combination, result in fibers being deposited over not only a larger area but also having a more uniform high thickness across larger cross sectional area. Figure 3-12 compares the thickness across the diameter of the cross-section of deposited fiber mat. The enlarged pictures show that the modified collector results in larger cross section with higher thickness. It's also evident that the edges of the fiber mat collected directly on aluminum foil tend to delaminate into layers. No such delamination was observed for the fiber mat deposited on ACF fiber mat. The fiber diameter for pure titania as well as titania fibers doped with varying levels of niobium dopants are presented in

Table 3-6. All parameters apart from the dopant level were kept constant to simplify comparison of the effect of Nb dopant on the morphology and photocatalytic activity of the fibers.

While establishing a clear trend of the effect of niobium doping on the fiber diameter requires more work and larger number of data points, it's clear that niobium increases the fiber diameter by almost two folds and also increases the standard deviation. Figure 3-13 shows a plot of fiber diameter versus the corresponding amount of niobium added as a dopant. The fiber diameters as well as standard deviation are significantly higher for 2.5 at% Nb compared to 5 at% and 10 at% Nb doped titania fibers. In fact the variation of fiber diameter between 5 at% and 10 at% Nb doped titania is insignificant. Addition of niobium ethoxide in the sol is expected to modify its electrical conductivity and surface tension. It is hypothesized that interplay between these two parameters is responsible for the initial sharp increase followed by decrease in fiber diameter with increase in dopant amount. A detailed study of the reason behind this behavior is beyond the scope of the present research and has been left as a future work.

The crystal structure of the fibers is of considerable interest from the point of view of photocatalysis for several reasons. Firstly, while there are scarcely any research article mentioning photocatalysis in amorphous TiO_2 ^[92, 93], almost all available literature is on crystallized titania^[94]. Even in the very few articles reporting photocatalytic properties of amorphous TiO_2 , crystallized TiO_2 shows far greater photocatalytic activity compared to the amorphous phase^[95]. Secondly, anatase exhibits better photocatalytic activity compared to rutile. This is because even though rutile has a higher bandgap

compared to anatase, the electron – hole recombination rate is lower in anatase ^[73]. And finally, semiconductor junction has been proven to improve the photocatalytic activity^[96, 97]. In this case if a mixture of anatase and rutile is formed during heat treatment it can possibly enhance the photocatalytic property. This is because even though their valence bands are at similar energy levels, the band gap of anatase is 0.2 eV less compared to rutile and hence the conduction band of anatase can act as a trapping level. Figure 3-14 shows the X-ray diffraction pattern of titania fibers doped with varying degrees of niobium. The results are as expected from theory. All the fibers were heat treated at 600°C for 3 hours. Rutile phase has strong peaks at 27°, 36° and slightly below 55°^[98] and these peaks are very strong in pure titania fibers. However the intensity of these peaks decrease monotonously as the amount of niobium dopant was increased. Some of the peaks in pure titania have contribution from both anatase and rutile but as Nb content increased, the intensity of such peaks decreased. Niobium is a pentavalent element and hence, once present in the lattice, results in reduction in the number of oxygen vacancies^[72] needed for anatase to rutile phase transformation. This is the most probable reason behind the strong suppression tendency of niobium on anatase to rutile transformation process. Similar results have been observed previously in Nb doped titania particles ^[71, 99].

One vital importance of this effect in real life applications is that filters made of Nb doped titania would not lose their photocatalytic activity after intentional or unintentional exposure to high temperature. The ramification is this that when used in-habitat in lunar missions these fibers can be cleaned both by heating using microwave as well as by

exposing to UV radiation. High temperature cleaning in microwave would not decrease its ability to be cleaned by photocatalysis.

Before finally moving on to the photocatalytic properties of Nb doped titania there is one last factor which must be considered and that is specific surface area. Firstly, since photocatalysis is a surface phenomenon it is affected by the specific area (i.e. surface area per unit mass). For this reason all observed photocatalytic activities must be normalized with respect to specific surface. This is to isolate the contribution coming just from the material irrespective of the amount of exposed surface. Secondly, it's also important to know if addition of Nb as dopant leads to surface porosity. BET technique (named after Stephen Brunauer, Paul Hugh Emmett and Edward Teller^[100]) was used towards this end. The specific surface area of titania fibers doped with varying amounts of niobium are presented in Figure 3-15. The fiber diameters for the corresponding fibers are also provided since specific surface is also a function of fiber diameter.

Neglecting packing density, for a perfectly smooth fiber of length l and material density ρ , the surface area and mass can be expressed by Eq. 3-8 and Eq. 3-9 respectively:

$$\text{Surface area} = 2\pi r l \quad (3-8)$$

$$\text{mass} = \pi r^2 l \rho \quad (3-9)$$

Since specific surface is the surface area per unit mass, it can be expressed mathematically by Eq. 3-10:

$$\text{Specific surface} = \frac{\text{Surface area}}{\text{mass}} = \frac{2\pi r l}{\pi r^2 l \rho} \propto \frac{1}{r} \quad (3-10)$$

This implies that for completely smooth non-porous cylindrical fibers, specific surface is inversely proportional to the radius and if a much higher specific area is observed than that expected from this, it can be attributed to porosity. For mathematical convenience, it is assumed that during the grinding process to produce sample for BET, the average length of broken fibers is equal for all the samples.

It is evident from the foregoing analysis and the plots in Figure 3-15. A) - B) that even though there is a decrease in $1/\text{radius}$ with increase in the amount of doped niobium, there is a significant increase in specific surface area. This strongly suggests that the doping results in tremendous increase in surface porosity. Figure 3-16 compares the cumulative volume of open pores on the surface for doped and undoped samples and further verifies this assertion. A particular advantage to the increased surface porosity is that more photocatalytically active surface is exposed per unit mass - even though it may lead to some deterioration of mechanical properties.

In the final part of the present research, all the titania fiber samples, doped with varying amounts of niobium, were tested for their photocatalytic properties. The initial dye solution has 0.0476 g of Procion Red MX-5B for each liter of the solution. Doped titania fibers, ground using mortar and pestle, was added to the initial dye solution at a concentration of 4.76×10^{-4} g/l. They were exposed to UVB radiation for 8h while stirring continuously. Finally syringe filters, with $1\mu\text{m}$ pores, were used to separate out the particles in order to carry out absorption spectroscopy for wavelength in the range of 250 nm – 800 nm. The absorbance is proportional to the concentration of un-degraded dye in the suspension according to the Beer-Lambert law^[101] as shown in Eq. 3-11; where A , ϵ and l are absorbance, absorptivity and length through which light passes:

$$A = \epsilon l C \quad (3-11)$$

This in turn implies that a decrease in absorbance (ΔA) is directly related to the amount of dye that is degraded. If C_0 is the initial concentration of dye and C is its concentration after exposure to radiation for a certain amount of time, then the decrease in absorbance can be mathematically expressed by Eq. 3-12.

$$\Delta A = \epsilon l \Delta C = \epsilon l (C_0 - C) \quad (3-12)$$

The reduction in absorbance can thus be used as a proxy for degradation. Figure 3-17 shows the absorbance of the residual dye when titania fibers, doped with varying amounts of niobium, were used as photocatalyst. As has already been discussed in details in the background section, photocatalysis is a surface phenomenon and so all the data were normalized with respect to specific surface for comparison. For the purposes of Beer-Lambert's law, absorbances for various samples are compared at a particular wavelength. Since Procion Red MX-5B dye has maximum absorbance at 538 nm, the normalized absorbance at this particular wavelength for un-degraded dye are also plotted versus the corresponding amount of dopant in titania used as photocatalyst. From the observations in Figures 3-17 it is evident that the photocatalytic activity of titania decreases with increase in the amount of doped niobium.

Previously published literature on the photocatalytic properties of niobium doped titania is inadequate. The hypothesis that niobium may enhance the photocatalytic activity is based on the effect of transition elements like Fe^{3+} and Cu^{2+} on creating trapping energy levels in the forbidden gap^[58] of titania which in turn prevent electron – hole recombination. It has also been theorized that such dopants reduce the band gap and increase the photonic efficiencies^[102]. However instead of the expected red-shift, a

blue-shift is observed in the differential reflectance with increase in Nb-dopant level. This is presented in Figure 3-18. A) and (B). This is consistent with the corresponding decrease in photocatalytic activity observed in Nb-doped titania. However, there is atleast one article reporting improvement in photocatalytic activity of titania by using niobium as dopant^[67]. In that instance, hydrothermal process was used and the synthesized material was in the particle form. One possible reason behind the contradictory observations in the present research might be the position of Nb atoms in the lattice. In the theory behind the generation of trapping energy level, it is assumed that Nb⁵⁺ substitute Ti⁴⁺ in the lattice ^[102, 103]. However if the atoms of Nb⁵⁺ exist in the interstitial spaces then the theory might not be applicable. In the absence of sufficient work on photocatalytic properties of Nb-doped titania it can also be hypothesized that Nb⁵⁺ substitution creates certain energy levels which instead of preventing electron – hole recombination, actually promote such recombination. Previously published research articles on the effect of chromium dopant on photocatalytic properties of titania have mentioned such promotion of the recombination process at Cr³⁺ sites^[52]. The fact that photocatalytic activity of Nb-doped titania decreases steadily with increase in niobium content, mostly point towards this explanation. Finally, the presence of semiconductor junction has been known to significantly improve photocatalytic activity by inhibiting electron – hole recombination ^[96, 97]. From the X-Ray diffraction studies it is evident that niobium, when used as dopant, highly inhibits the formation of rutile. Thus there is a decrease in anatase-rutile junctions. This may also lead to a decrease in observed photocatalytic behavior.

Table 3-1. TiO₂-SiO₂ aqueous sol compositions and electrospinning conditions used throughout the research for TiO₂-SiO₂ sol [E = 1 kV/cm, Q = 0.6 ml/h, collector distance = 25 cm.]

Composition of sol	Amount of PVP added (M _w 1.3x10 ⁶)	Mean fiber diameter
TiO ₂ -SiO ₂ sol	0.4% w/v	Too many beads and uneven fiber diameter
TiO ₂ -SiO ₂ sol	0.5% w/v	Too many beads and uneven fiber diameter
TiO ₂ -SiO ₂ sol	0.75% w/v	Too many beads and uneven fiber diameter
TiO ₂ -SiO ₂ sol	1.25% w/v	311 nm
TiO ₂ -SiO ₂ sol	1.5% w/v	337 nm
TiO ₂ -SiO ₂ sol	2% w/v	444 nm
TiO ₂ -SiO ₂ sol	3% w/v	1231 nm
TiO ₂ -SiO ₂ sol	4% w/v	1337 nm

Table 3-2. Fiber diameter of electrospun TiO₂-SiO₂ fibers after heat treatment in presence of air in a box furnace

Composition of sol	Amount of PVP added (M _w 1.3x10 ⁶)	Heat treatment condition	Mean fiber diameter
TiO ₂ -SiO ₂ sol	1.25% w/v	600°C for 3h in air. Furnace cooled.	195 nm
TiO ₂ -SiO ₂ sol	1.5% w/v	600°C for 3h in air. Furnace cooled.	136 nm
TiO ₂ -SiO ₂ sol	2% w/v	600°C for 3h in air. Furnace cooled.	350 nm
TiO ₂ -SiO ₂ sol	4% w/v	600°C for 3h in air. Furnace cooled.	803 nm

Table 3-3. Loss of fiber diameter on heat treatment at 600°C in air for 3 hours

PVP content (% w/v)	Percent cross section loss after heat treatment
1.25	60.5
1.5	83.7
2.0	37.8
4.0	63.8

Table 3-4. Influence of addition of ethanol on fiber diameter of heat treated electrospun TiO₂-SiO₂ fibers (2% w/v PVP, M_w 1.3x10⁶ used as polymeric aid)

Composition	Average fiber diameter	Standard deviation
TiO ₂ -SiO ₂ sol	350 nm	50 nm
TiO ₂ -SiO ₂ sol + Ethanol (1:1 volume ratio)	157 nm	42 nm

Table 3-5. Modifying fiber diameter of heat treated fiber by varying different electrospinning parameters

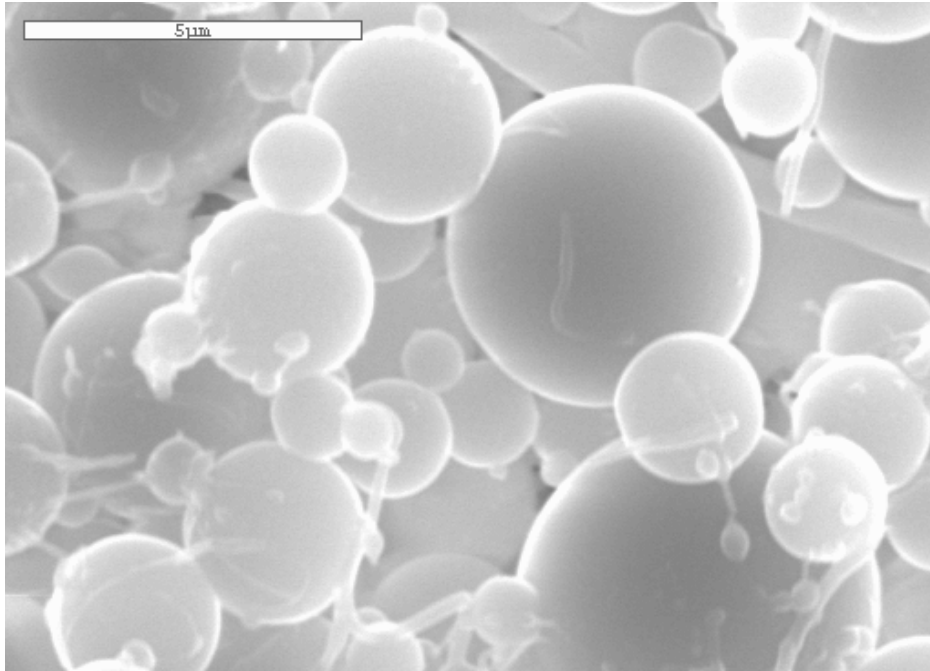
Composition	Flow rate (ml/h)	Electric field Strength (kV/cm)	Collector distance (cm)	Fiber diameter after heat treatment (nm)
1.5% w/v PVP ($M_W = 1.3 \times 10^6$) dissolved in TiO_2 - SiO_2 sol	0.6	1	25	280 ± 35
4.0% w/v PVP ($M_W = 1.3 \times 10^6$) dissolved in TiO_2 - SiO_2 sol	0.6	1	25	803 ± 116
6.5% w/v PVP ($M_W = 1.3 \times 10^6$) dissolved in TiO_2 - SiO_2 sol	1.5	1	25	1138 ± 299
6.0% w/v PVP ($M_W = 1.3 \times 10^6$) dissolved in TiO_2 - SiO_2 sol	1	1	25	1541 ± 295

Table 3-6. Fiber morphology for electrospun fibers of pure titania and niobium doped titania after heat treating at 600°C for 3 hours. 4% w/v PVP was added. Electric field strength and flow rate were maintained at 1 kV/cm and 0.6 ml/h.

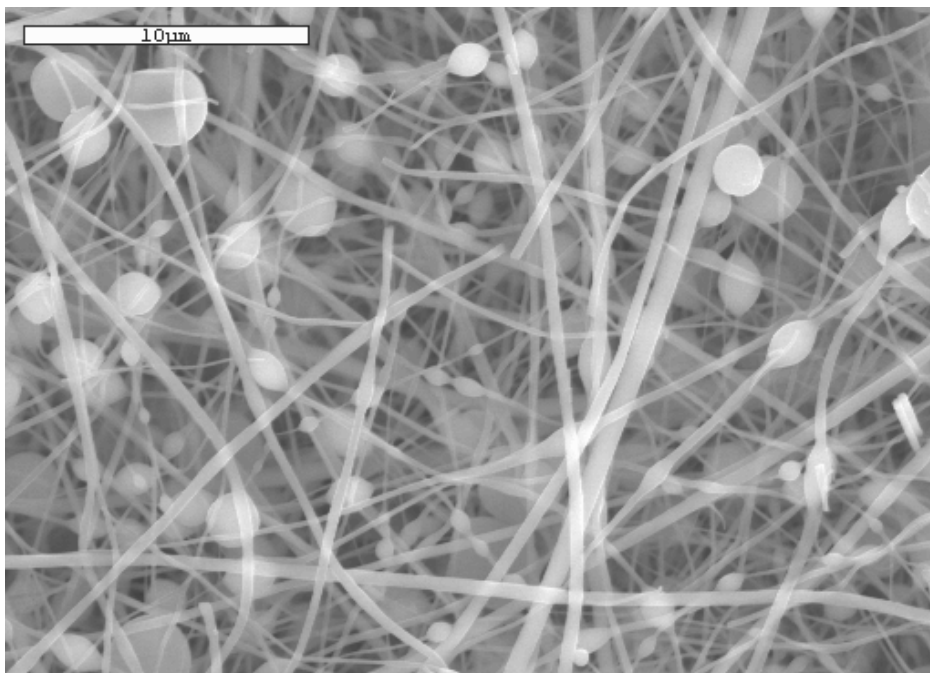
Composition	Fiber diameter (nm)
Pure titania	1321 ± 339
2.5 at% Nb doped titania	2933 ± 1072
5.0 at% Nb doped titania	2091 ± 687
10.0 at% Nb doped titania	2113 ± 833

Table 3-7. Specific surface of niobium doped titania fibers after heat treatment

Composition	Fiber diameter (nm)	Specific surface (m ² /g)
Pure titania	1321 ± 339	4.3
2.5 at% Nb doped titania	2933 ± 1072	16.9
5.0 at% Nb doped titania	2091 ± 687	29.6
10.0 at% Nb doped titania	2113 ± 833	26.1

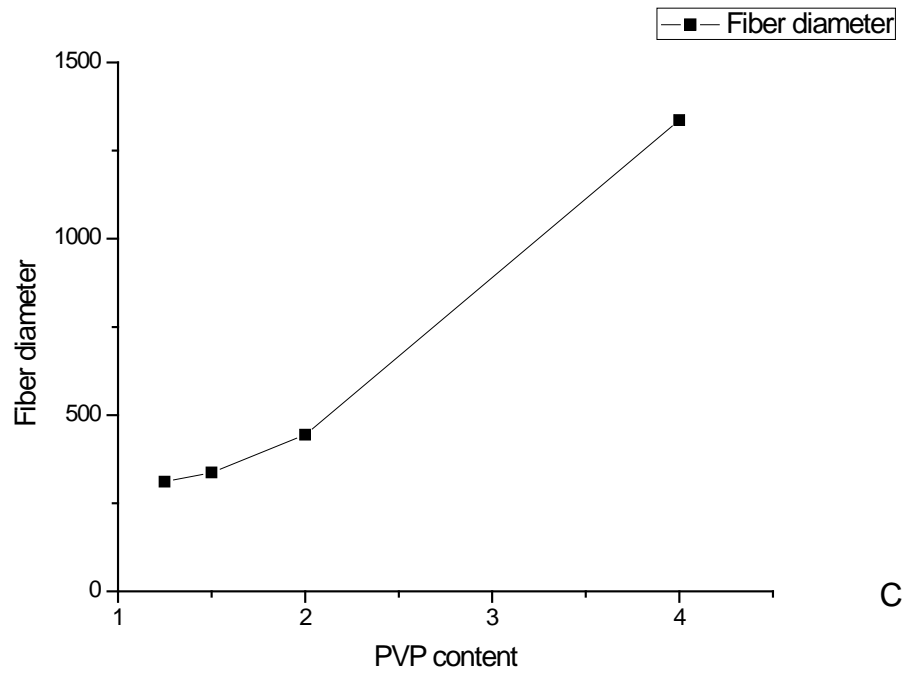


A



B

Figure 3-1. Influence of PVP content on the morphology of electrospun $\text{TiO}_2\text{-SiO}_2$ fibers. Images obtained using scanning electron microscopy of fibers electrospun from sol containing A) 0.4% w/v PVP and B) 0.5% w/v PVP. Notice the presence of several beads. When fibers are present, they are highly irregular with a huge variation in diameter. C) Plot showing increase in fiber diameter with increase in PVP content.



C

Figure 3-1. Continued.

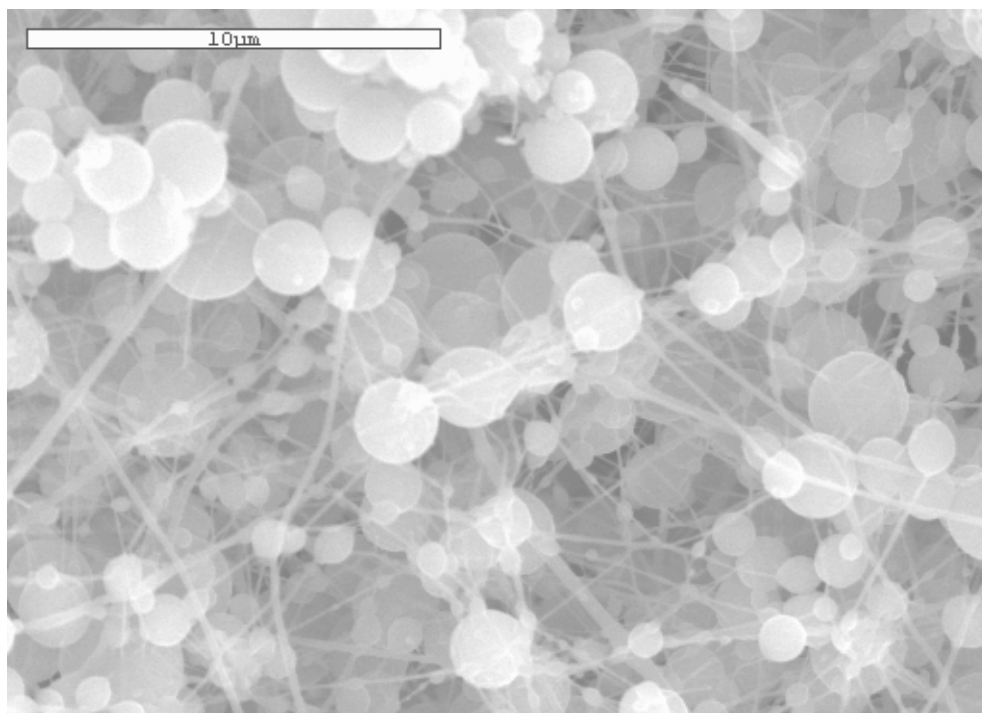
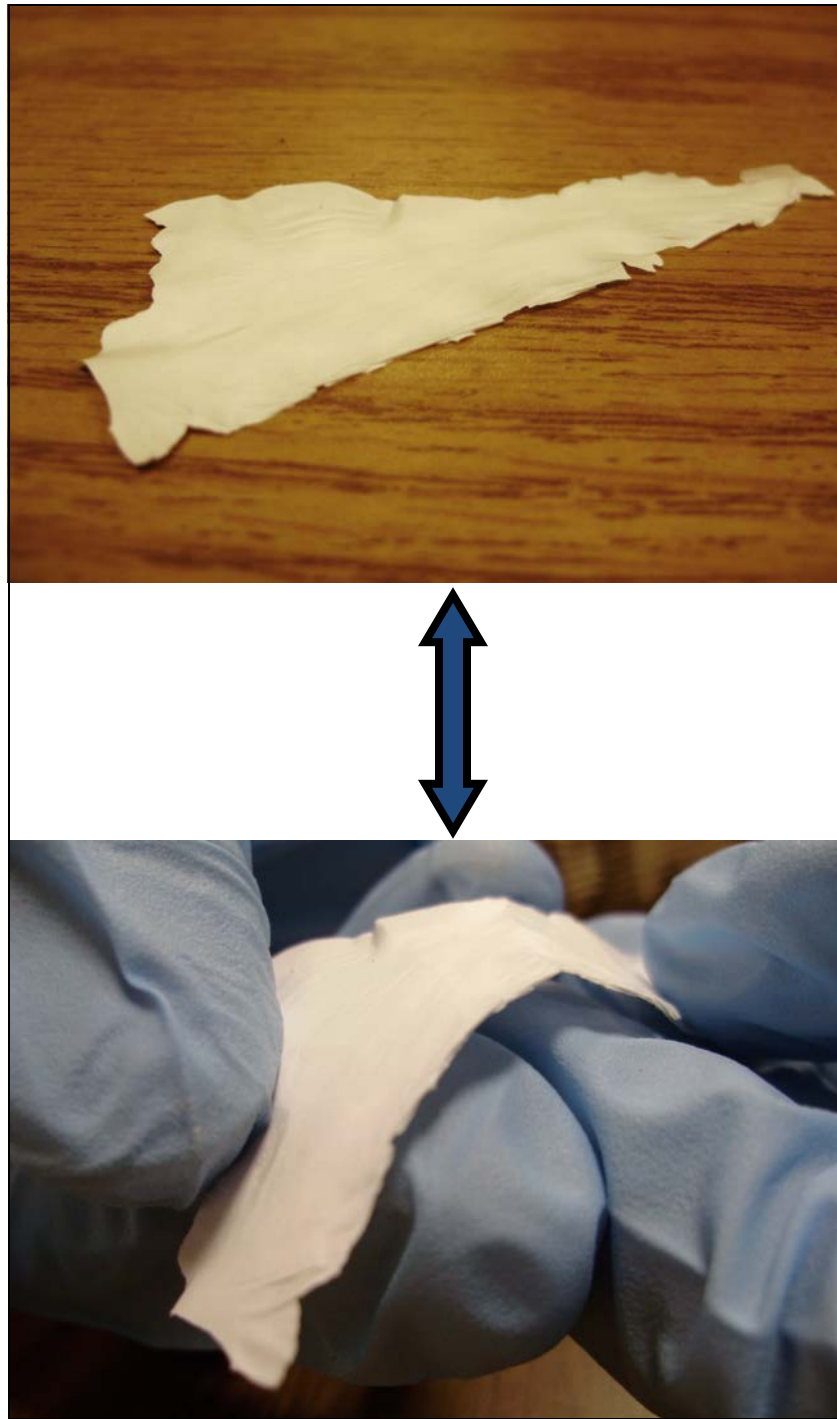


Figure 3-2. $\text{TiO}_2\text{-SiO}_2$ fibermats, electrospun from sol containing 0.4% w/v PVP, after heat treatment at 600°C for 3h. Figure 3-1. A) shows the same material before heat treatment. There is a significant reduction in the beads after heat treatment.

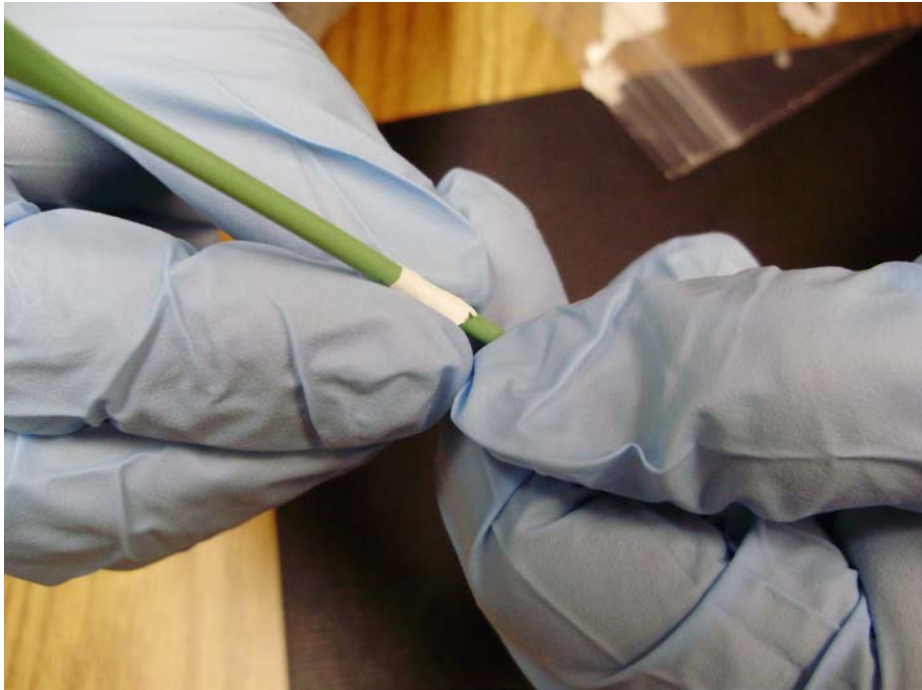


A

Figure 3-3. Flexibility of heat treated $\text{TiO}_2\text{-SiO}_2$ fibers. A) $\text{TiO}_2\text{-SiO}_2$ fibermat, heat treated at 600°C , exhibiting flexibility and can be bent without fracture. (B) and (C) demonstrate that the fibermat may be curved to a radius of curvature of 3.4 mm and in certain portions up to 1.3 mm respectively. Reprinted from A. Biswas, H. Park, W. M. Sigmund, *Ceramics International* **2012**, 38, with permission from Elsevier.

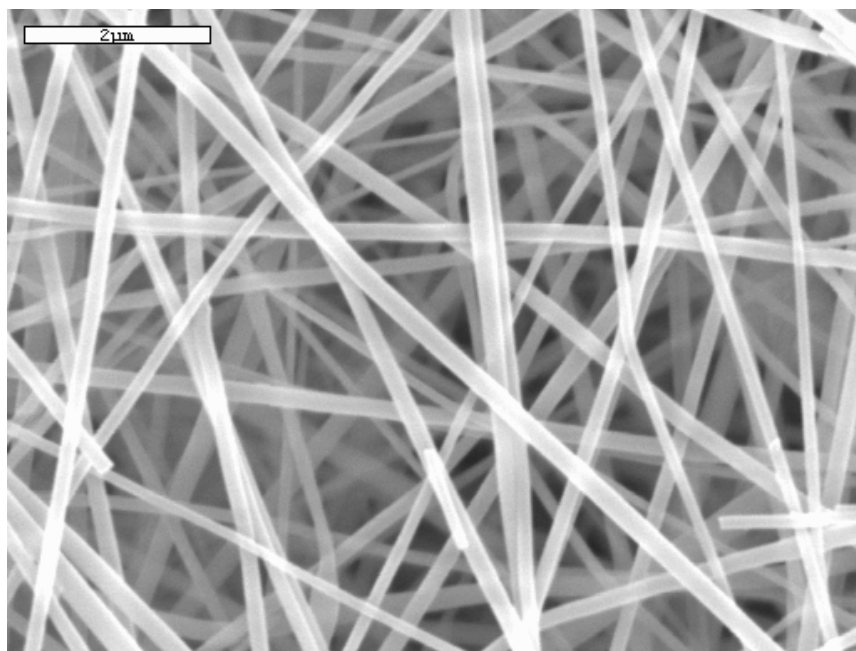


B

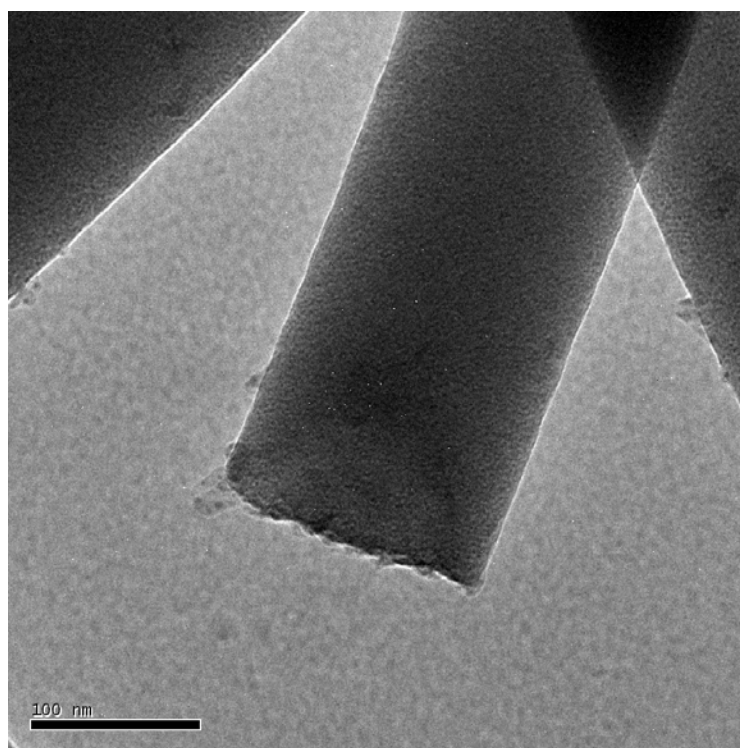


C

Figure 3-3. Continued.

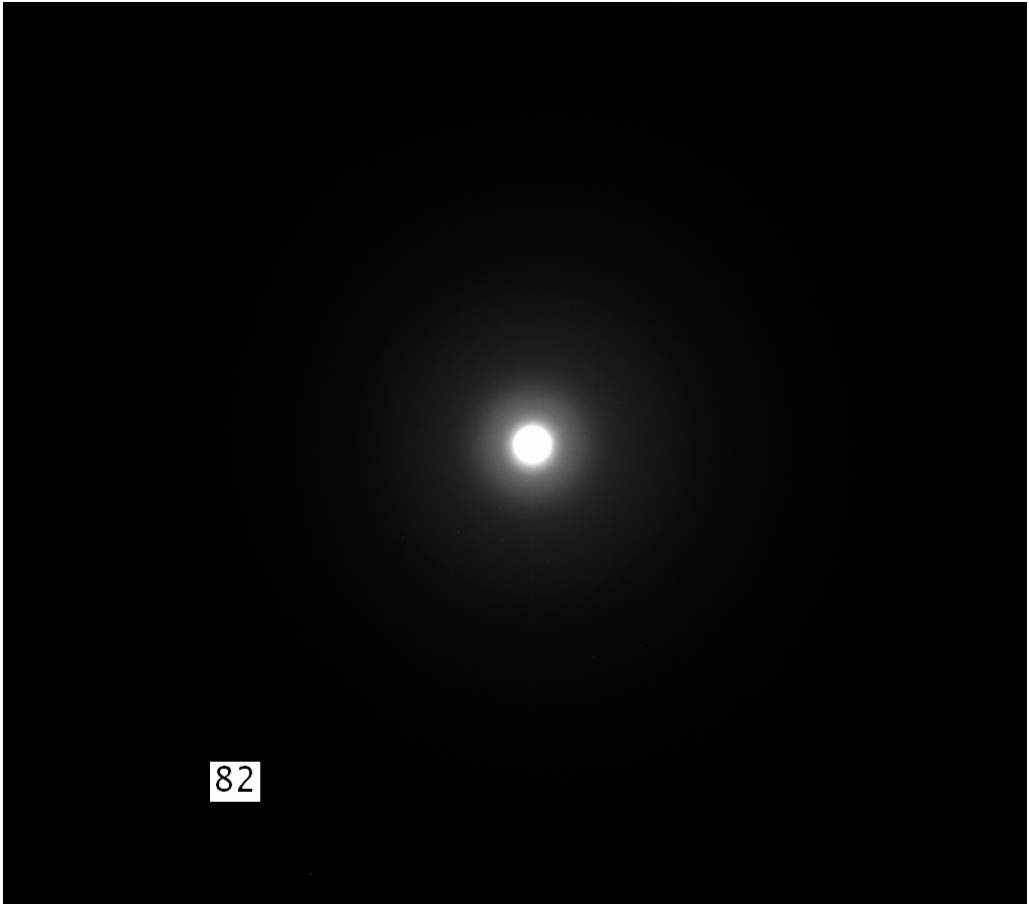


A



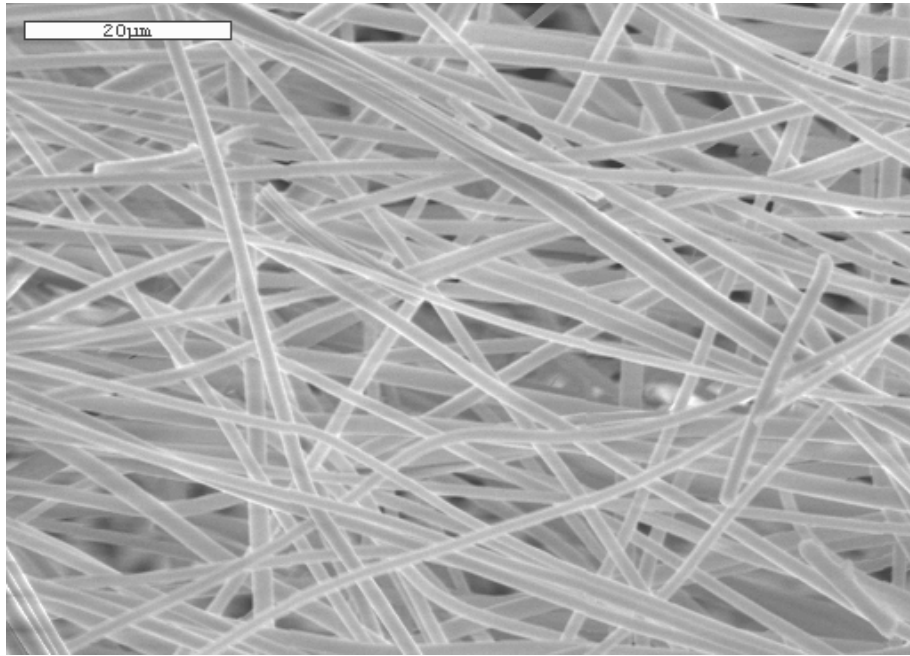
B

Figure 3-4. Morphology and crystallinity of heat treated $\text{TiO}_2\text{-SiO}_2$ nanofibers. A) Scanning electron microscopic image of electrospun fibermat. The $\text{TiO}_2\text{-SiO}_2$ sol was mixed with Ethanol to lower Surface Energy and fiber diameter. (B) No surface defects were observed in transmission microscope image of individual fibers. (C) Diffused ring pattern, obtained from selected area diffraction of fibers, is characteristic of an amorphous structure.

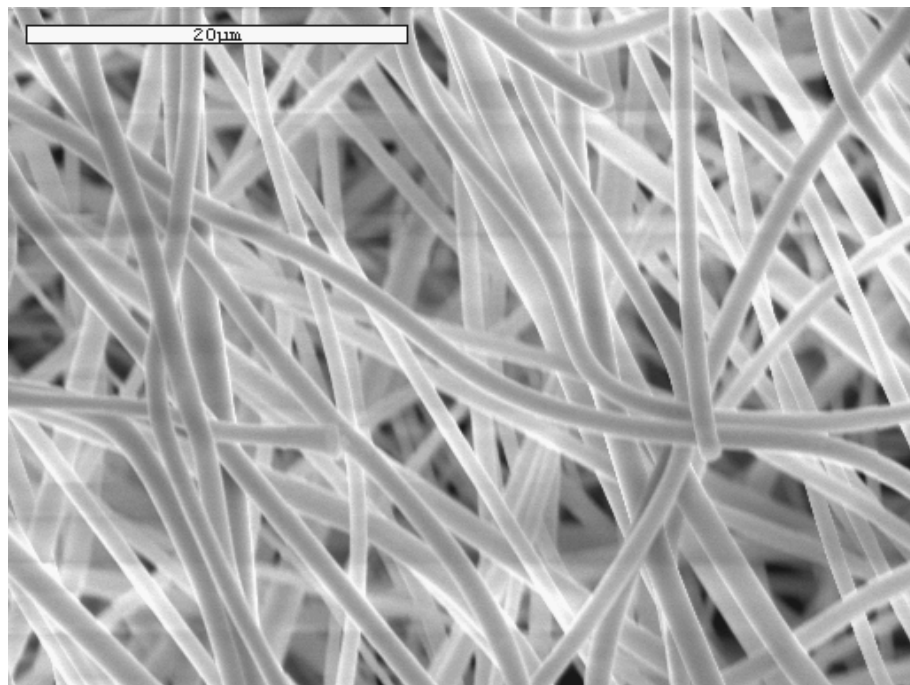


C

Figure 3-4. Continued.



A



B

Figure 3-6. Electrospun micron sized $\text{TiO}_2\text{-SiO}_2$ fibers. Scanning electron microscopic image of $\text{TiO}_2\text{-SiO}_2$ fibers electrospun using (A) 6.0% w/v PVP as polymeric aid and 1 ml/h flow rate and (B) 6.5% w/v PVP as polymeric aid and 1.5 ml/h flow rate.

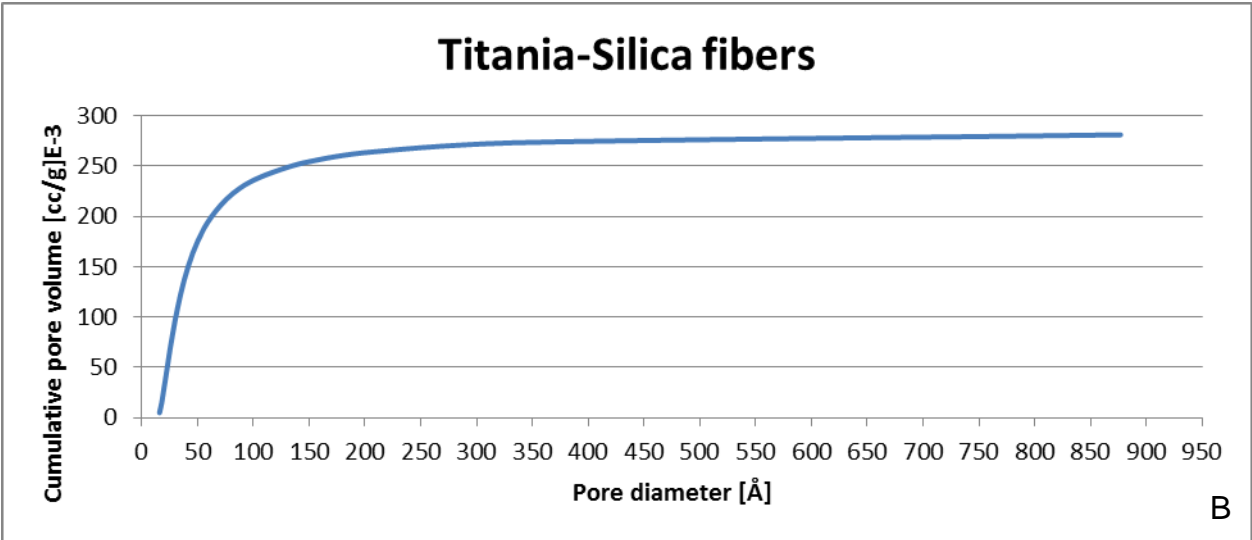
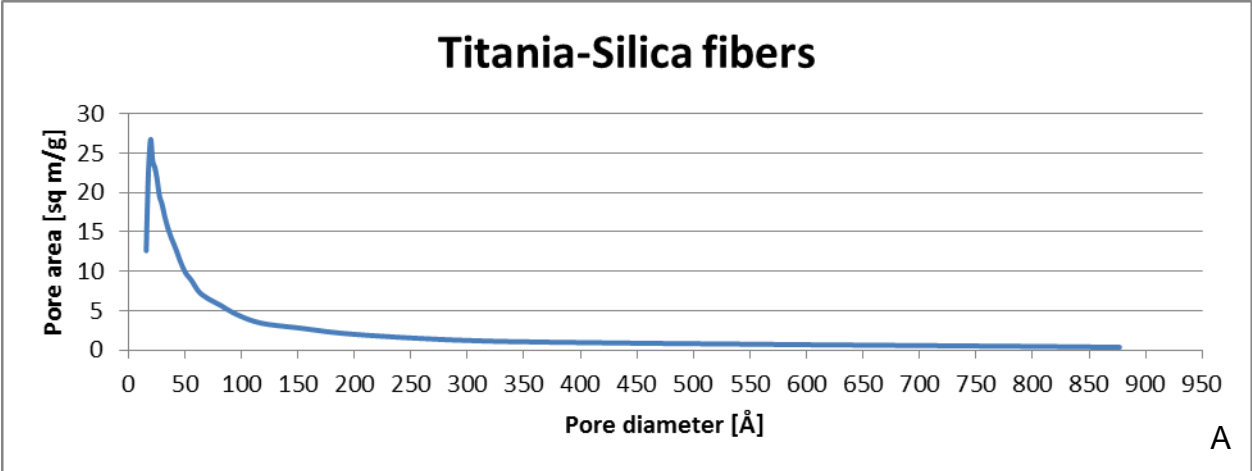


Figure 3-7. Pore size distribution of electrospun $\text{TiO}_2\text{-SiO}_2$ fiber mat obtained using BJH method. A) Pores with diameter of approximately 2.5 nm has the largest contribution towards the pore area. B) Almost entire volume of pores are from pores with diameter less than 25 nm.

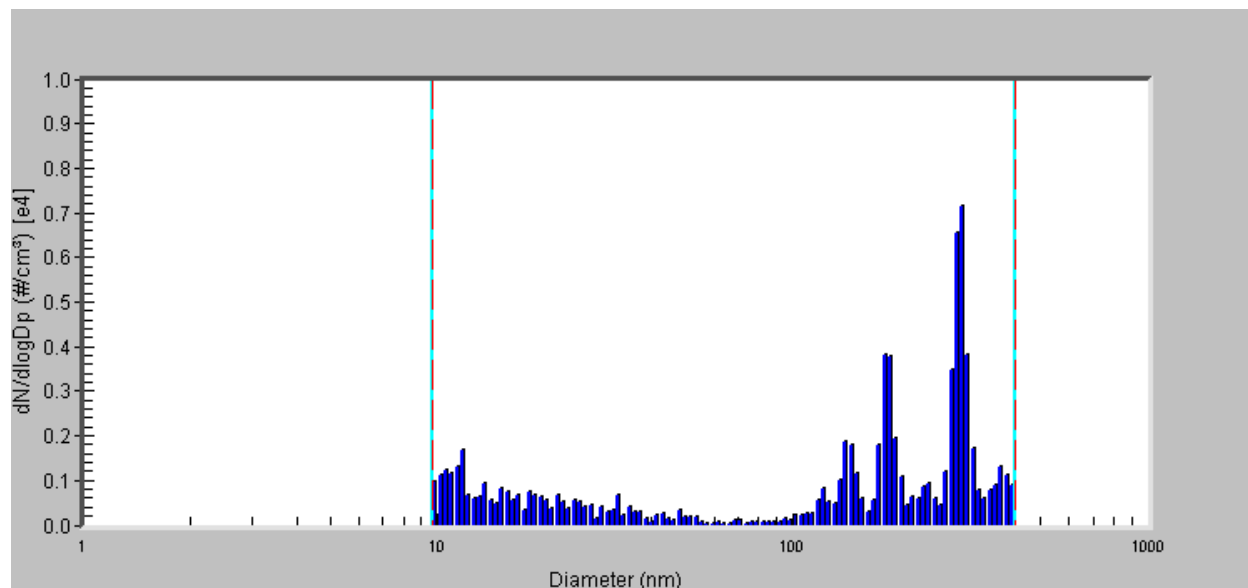


Figure 3-8. Original particle size distribution of aerosol generated in the filtration testing set-up. A scanning mobile particle counter was used to obtain the data on the distribution.

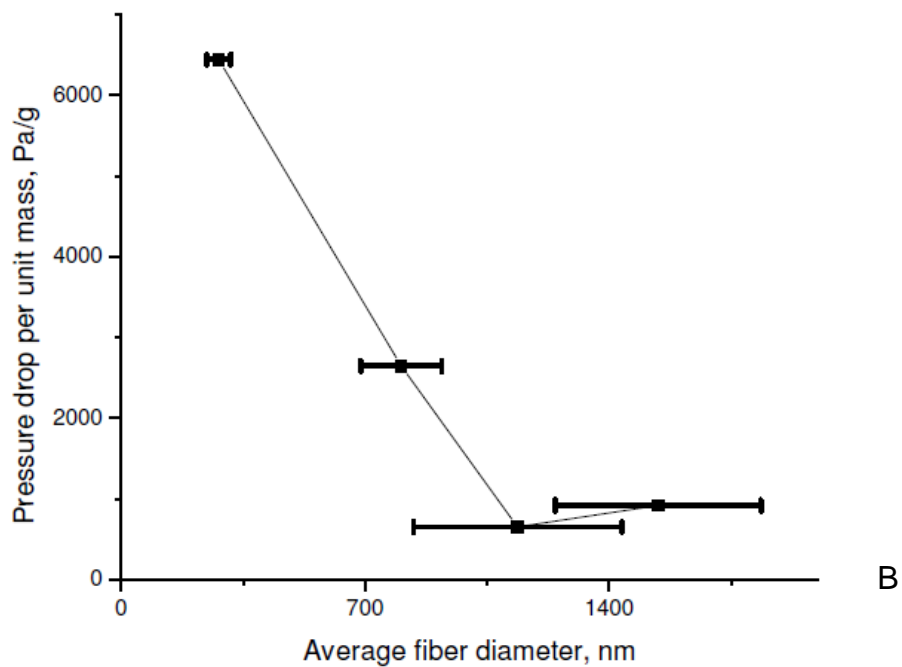
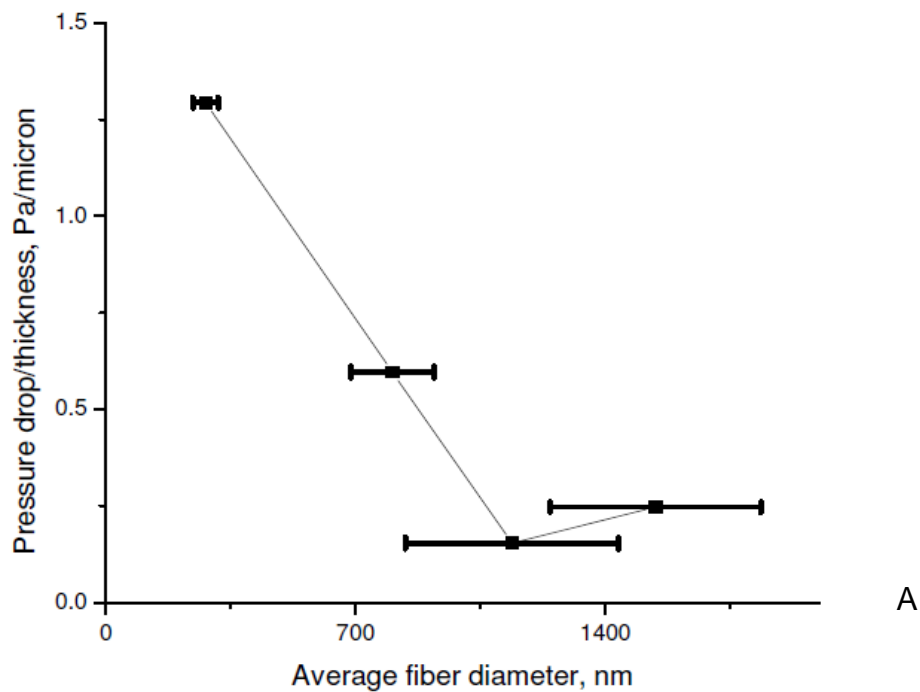


Figure 3-9. Experimentally determined pressure drop of electrospun $\text{TiO}_2\text{-SiO}_2$ fibermats plotted vs average fiber diameter. Pressure drop normalized with respect to (A) fibermat thickness^[104] and (B) mass of fibermat^[104], plotted against average fiber diameter. (C) Comparison of electrospun $\text{TiO}_2\text{-SiO}_2$ filtermats with data for commercially available HEPA and ULPA filters.

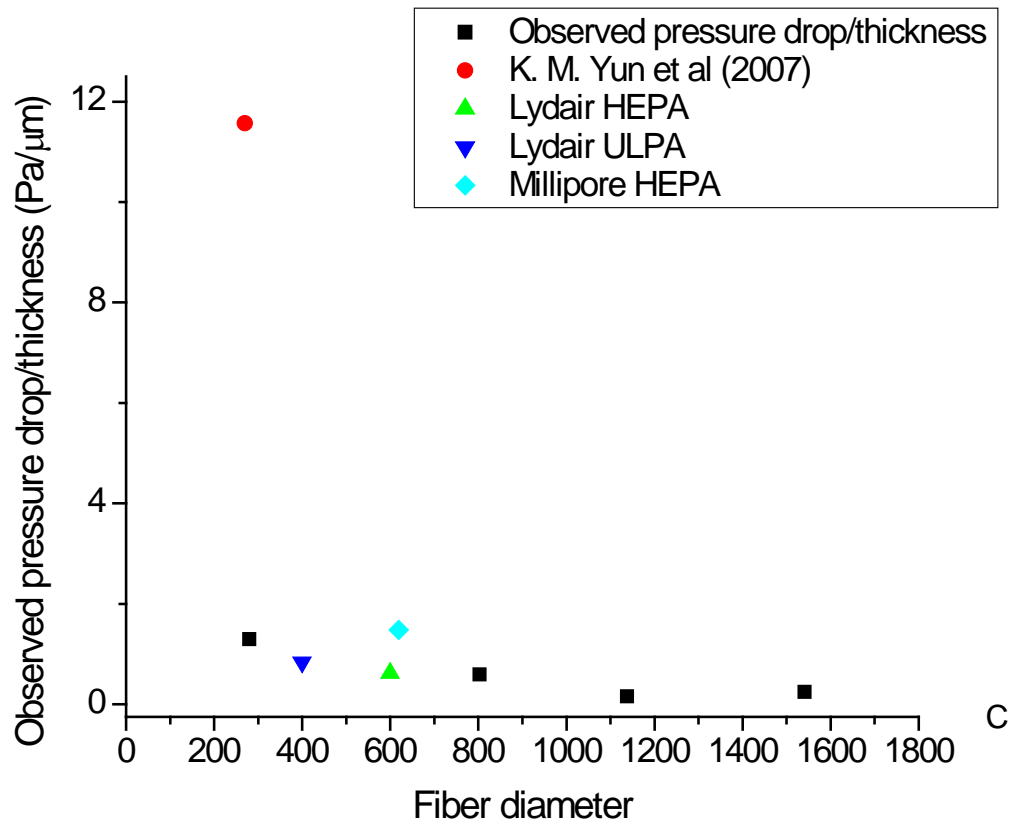


Figure 3-9. Continued.

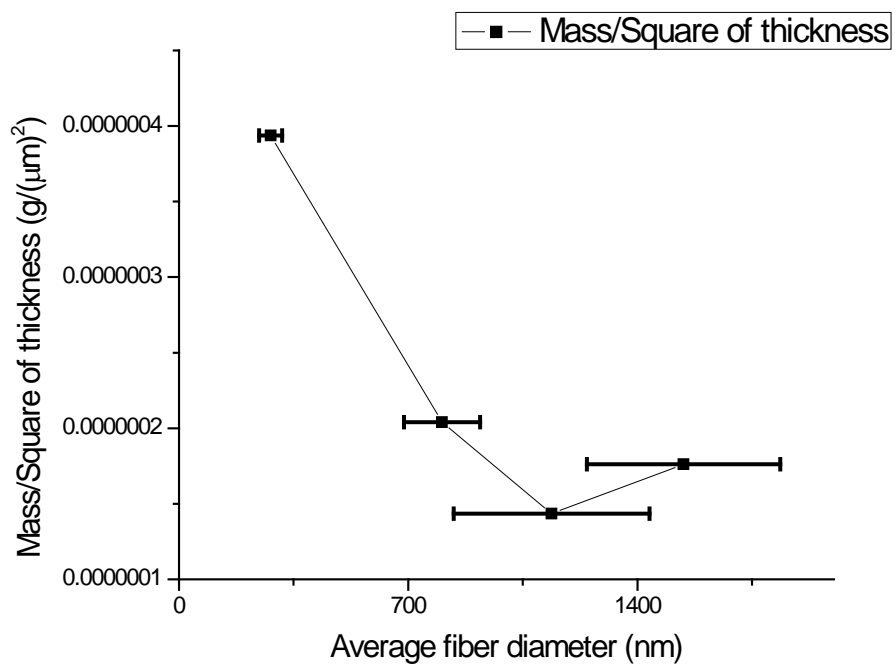


Figure 3-10. Plot of mass/(square of thickness) vs average fiber diameter. Mass/square of thickness is proportional to packing density of fibers.

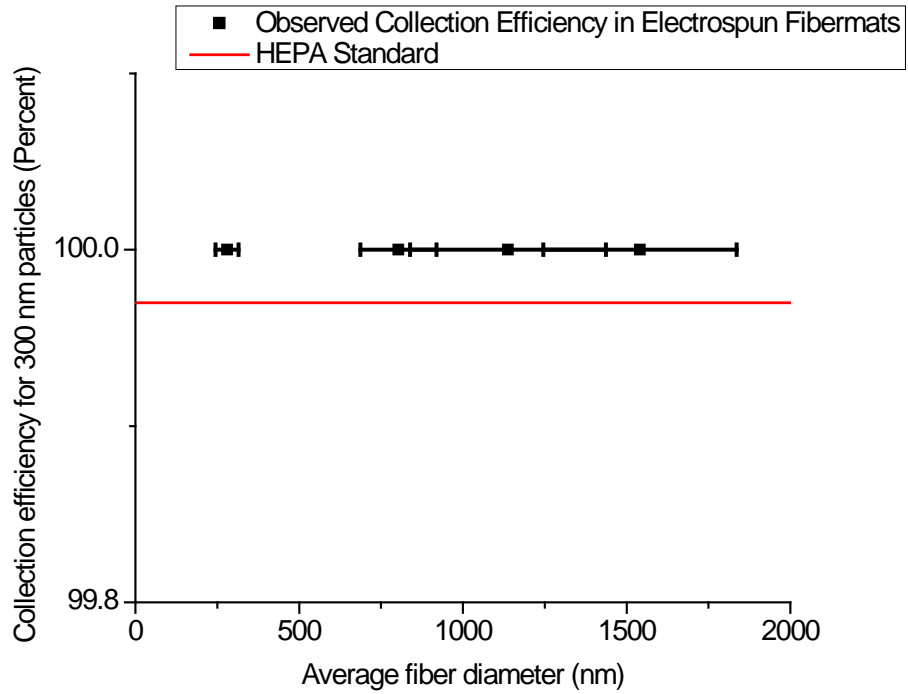
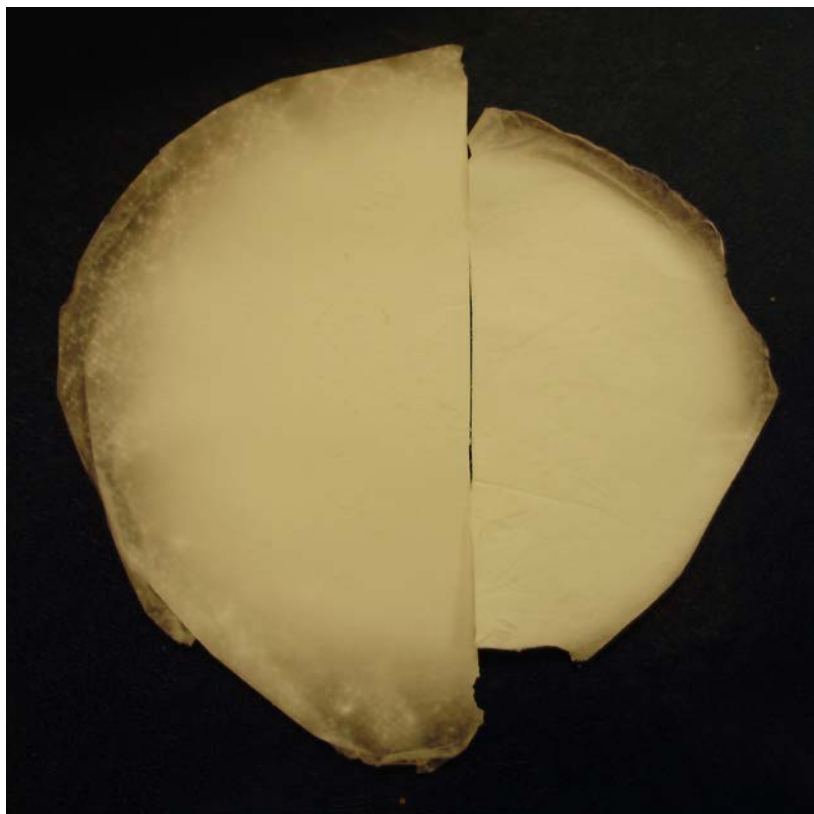
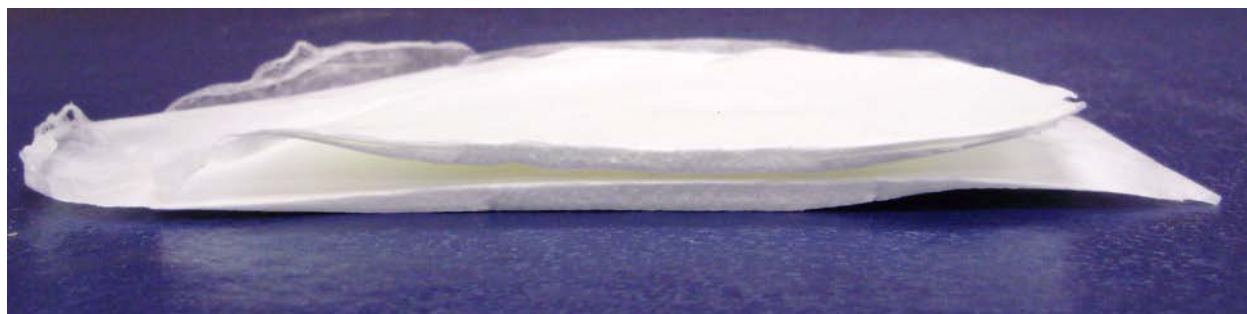


Figure 3-11. Collection efficiency of ceramic fibermats plotted versus average fiber diameter. Within the resolution of our instrument, near perfect efficiency was observed in all the four cases.



A



B

Figure 3-12. The effect of using activated carbon fiber as collector for electrospun fibers. A) The left semi-circle is from a fibermat deposited on an ACF fibermat. The one on the right is from a fibermat deposited directly on aluminum. Notice the difference in size. B) The effect of collector modification on the thickness of the cross-section is displayed by placing the fibermat collected over ACF on top of the one collected over aluminum collector. The fibermat collected on aluminum foil has a tendency to delaminate, and as shown in (C) and (D), this is especially prominent at the edges. An enlarged picture of the cross-section of a fibermat, deposited on ACF, is depicted in (E). It shows no such delamination. The titania fibermat is flexible even after heat treating at 600°C for 3 hours as shown in figure (F). Figures (A) – (E) depict titania fiber mats before heat treatment while figure (F) shows the fibermat after heat treatment.

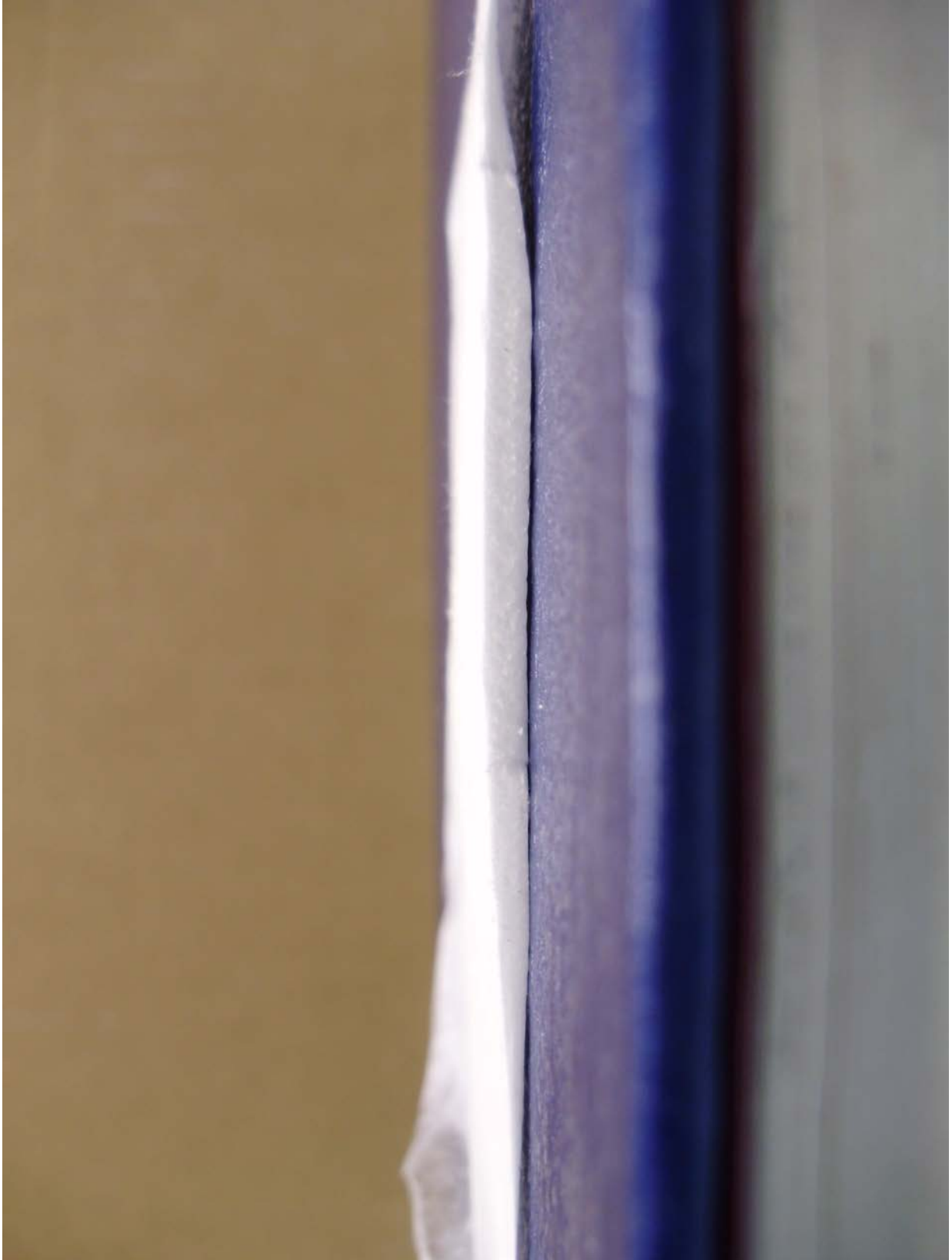


C



D

Figure 3-12. Continued.



E

Figure 3-12. Continued.



F

Figure 3-12. Continued.

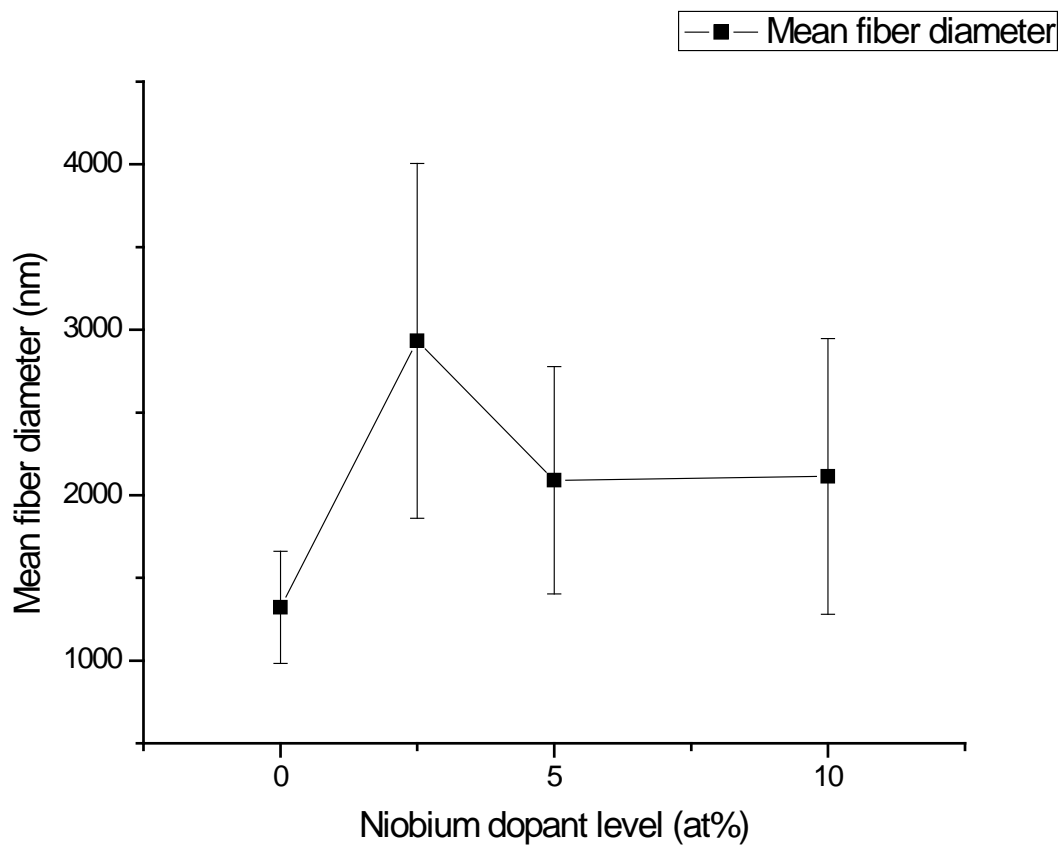


Figure 3-13. Dependence of fiber diameter after heat treatment on the niobium dopant level. All other electrospinning parameters were maintained constant for all the four data points.

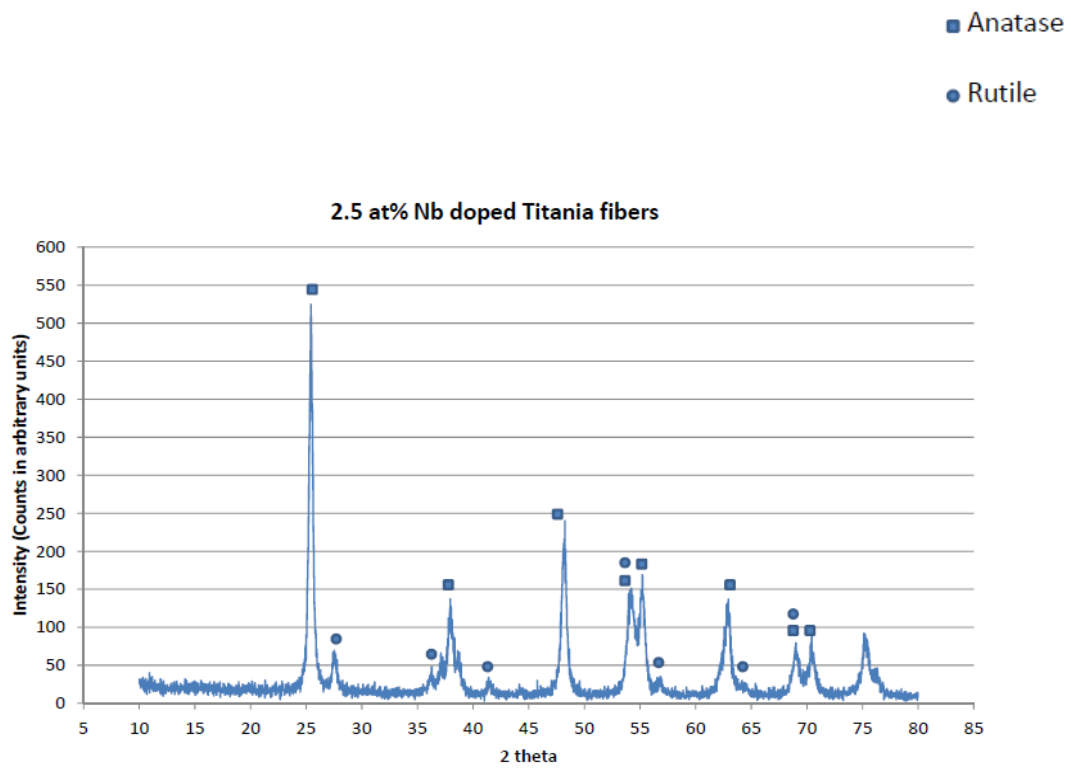
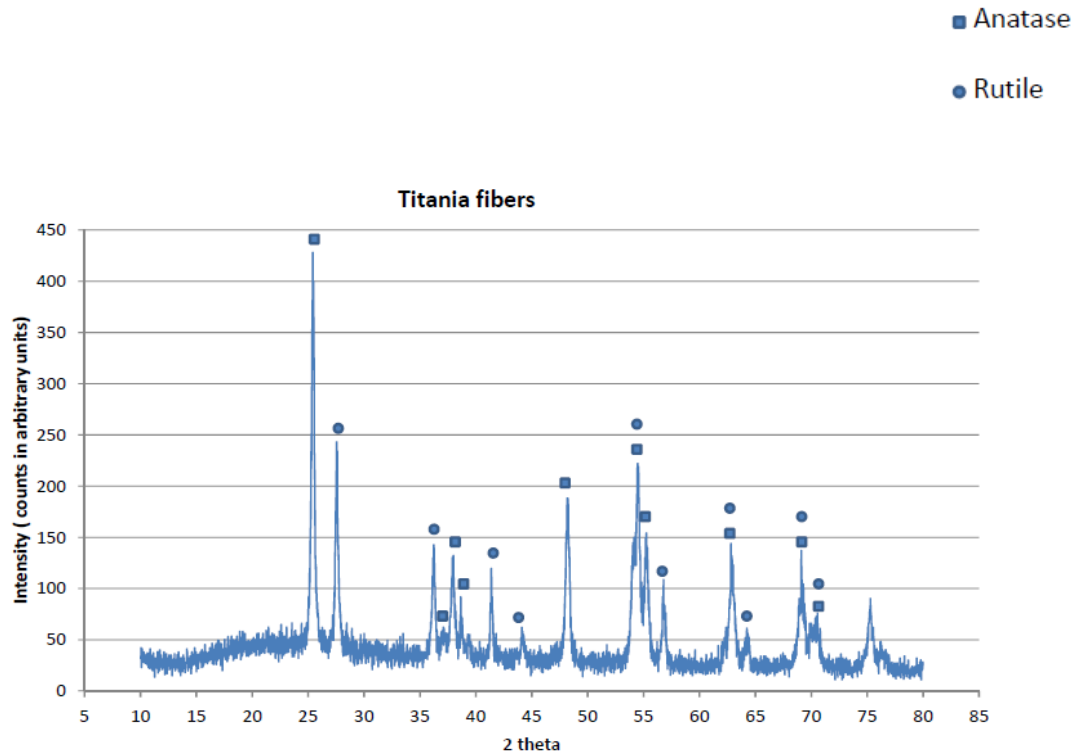


Figure 3-14. X-ray diffraction plots demonstrating the impact of niobium dopant on anatase to rutile phase transformation.

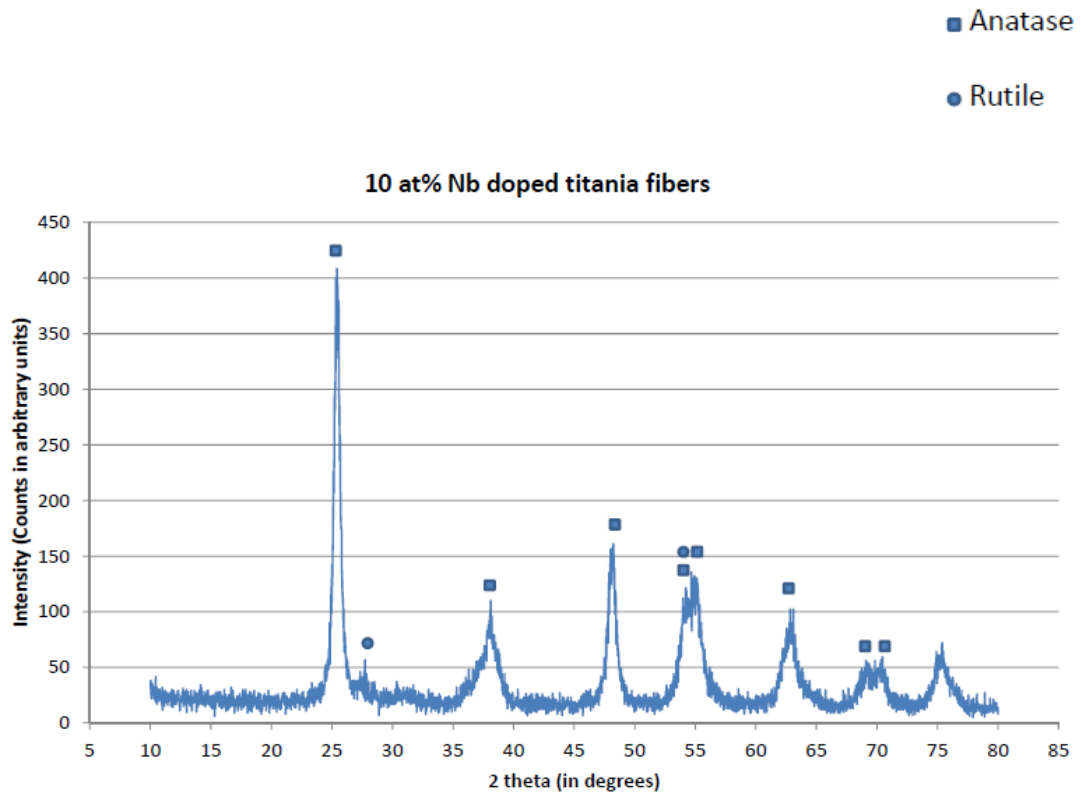
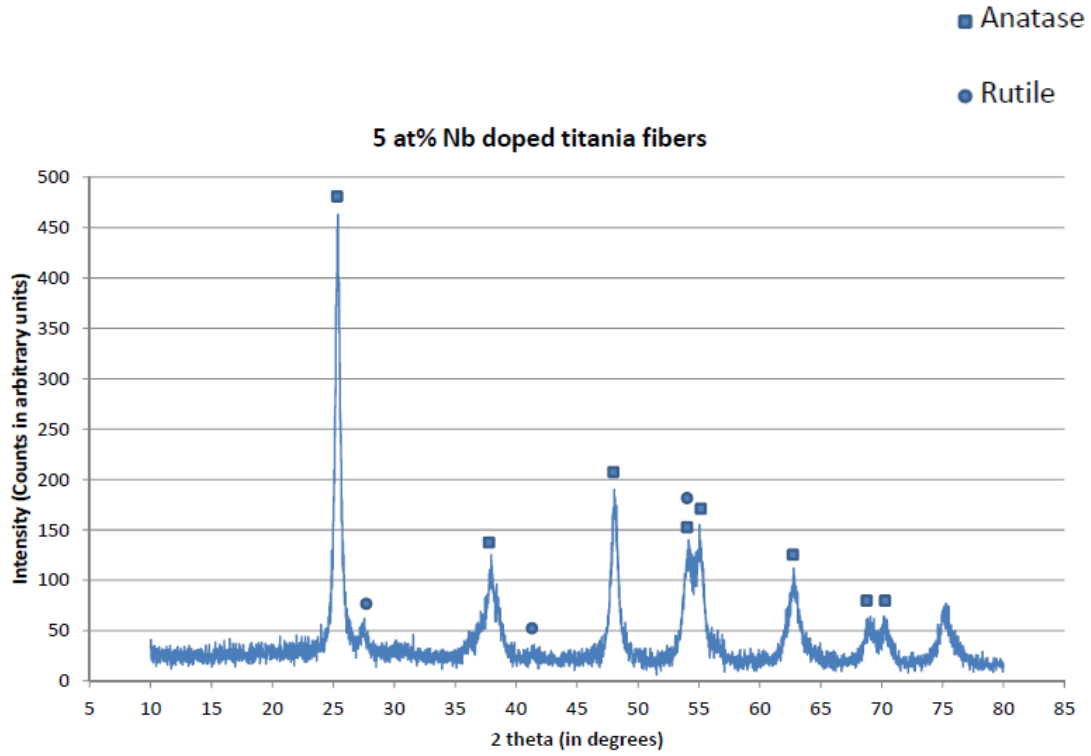


Figure 3-14. Continued.

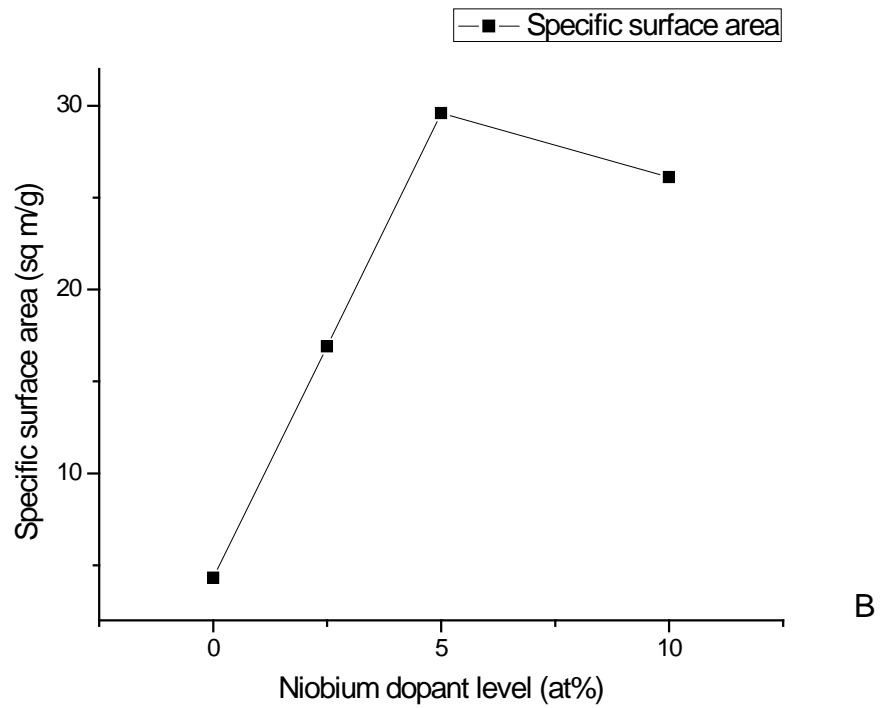
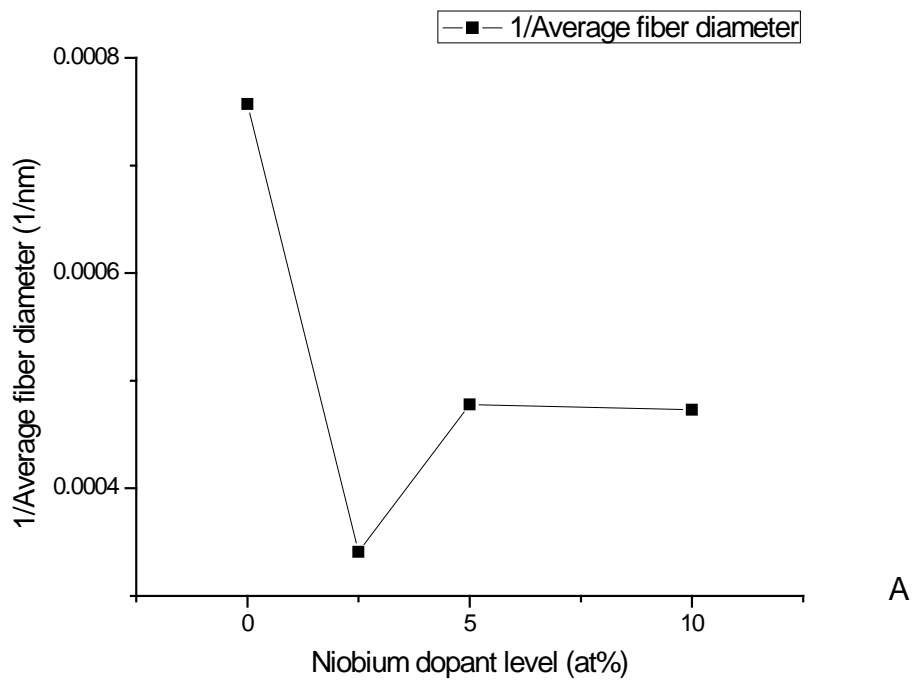


Figure 3-15. Effect of niobium dopant on diameter and specific surface of electrospun TiO₂ fibers. A) 1/fiber diameter plotted vs amount of niobium doped. B) Specific surface plotted vs amount of niobium doped.

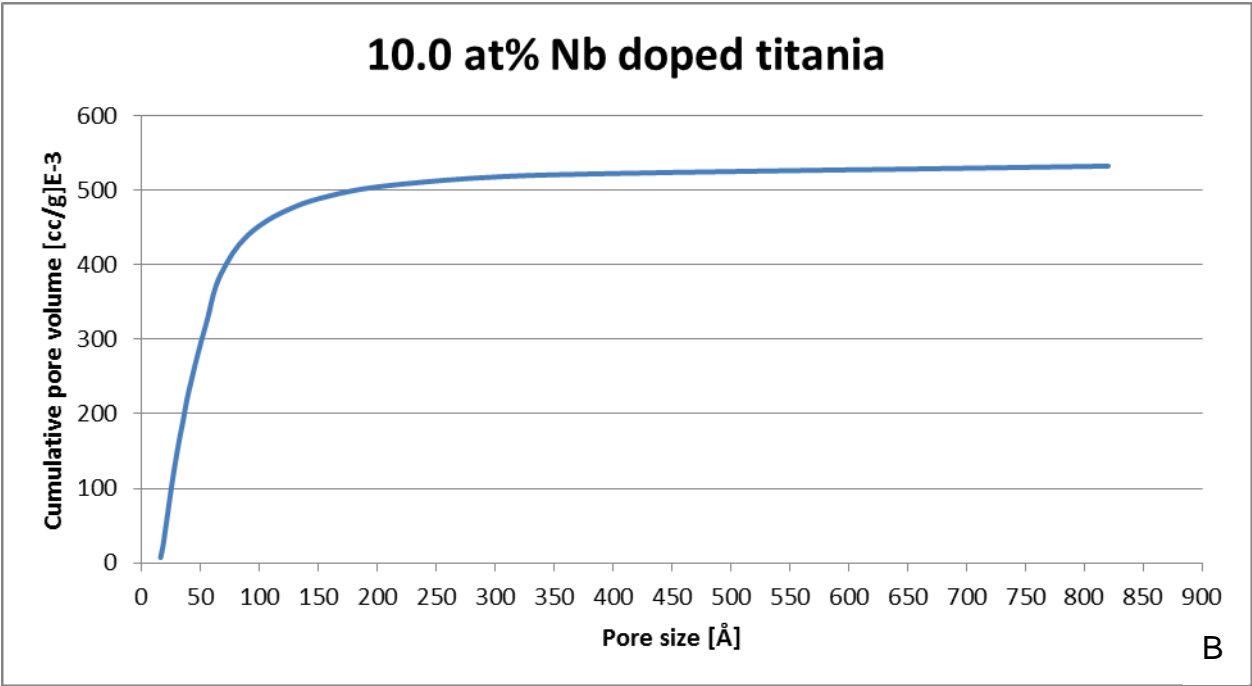
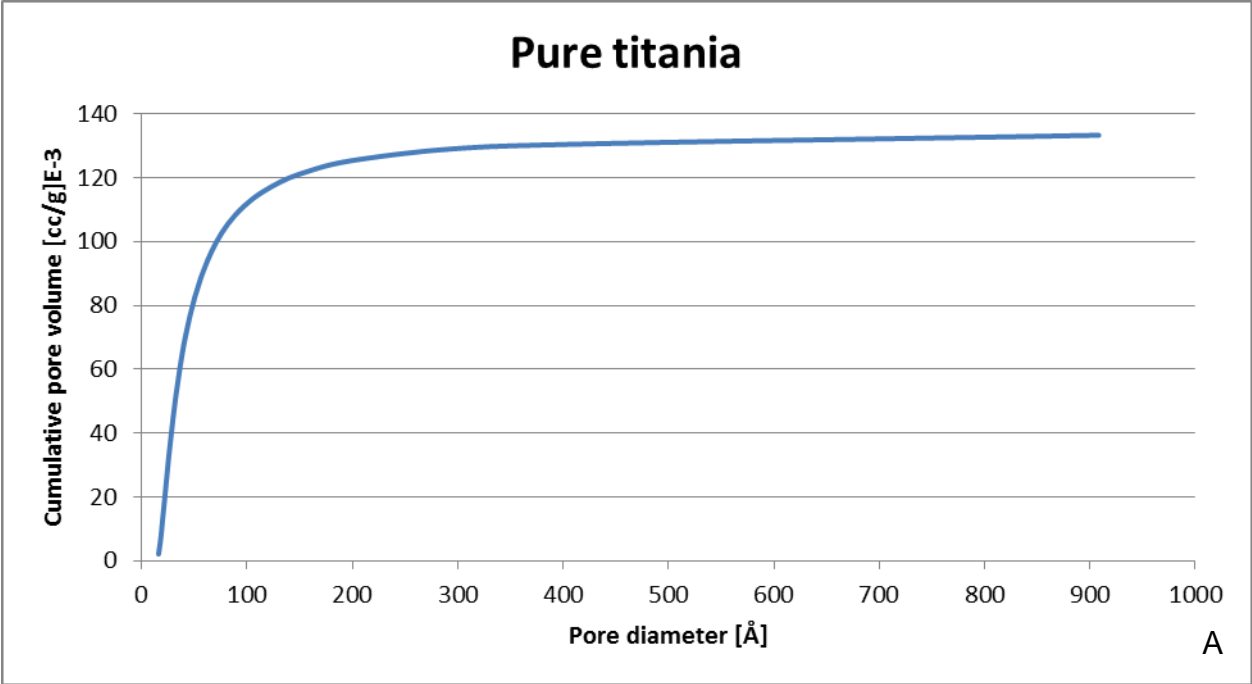


Figure 3-16. BJH pore size analysis of niobium doped titania fibers. Comparison of distribution of cumulative pore volume for A) pure titania and B) titania doped with 10.0 at% niobium.

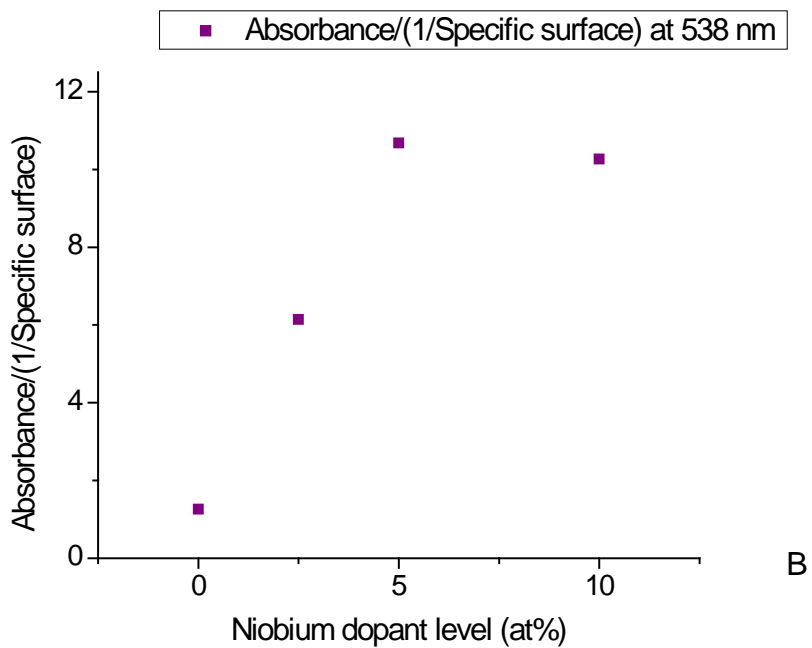
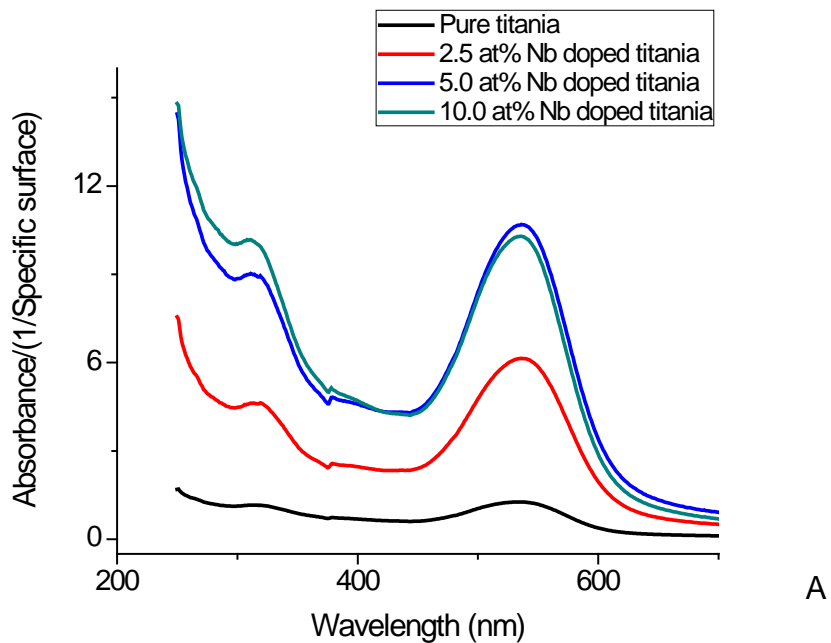


Figure 3-17. Influence of niobium dopant on UV/Vis absorption spectra of titania fibers. A) Spectra of absorbance normalized w.r.t (1/specific surface) for dye solutions after exposure to UVB for 8h. Electrospun titania fibers doped with different amount of niobium were used as photocatalyst. (B) Absorbance/(1/specific surface) for 538 nm wavelength.

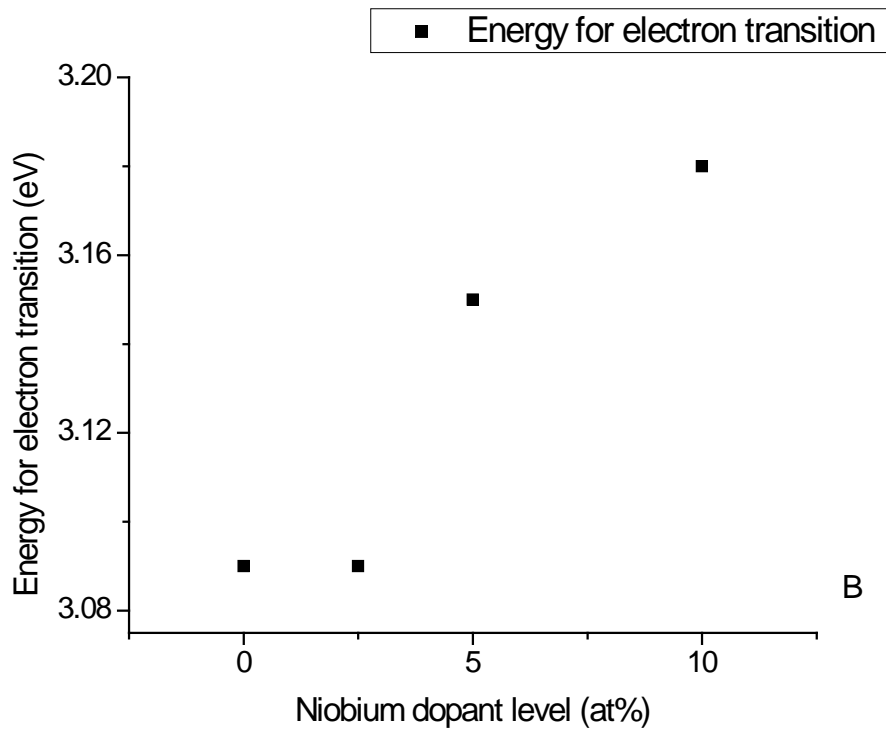
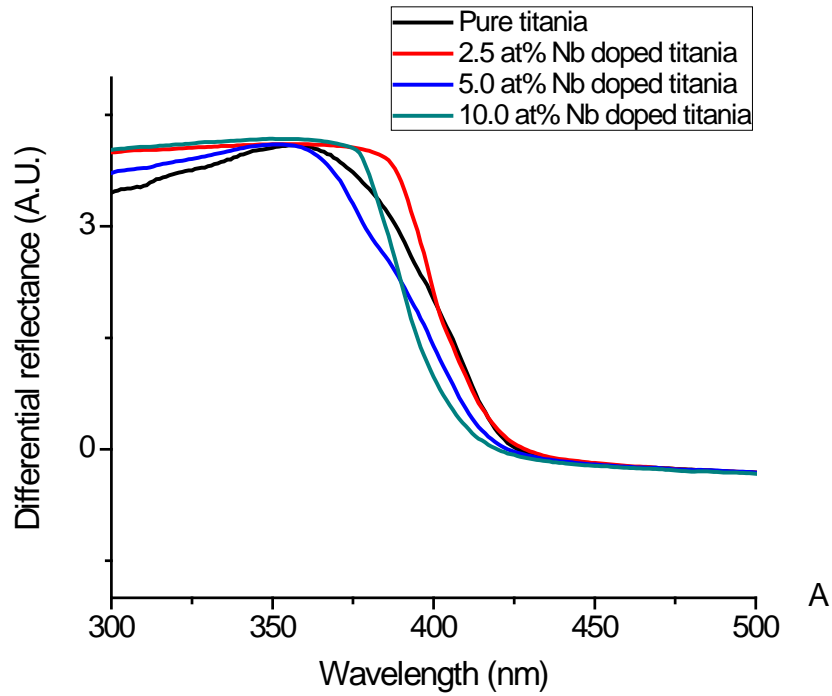


Figure 3-18. Differential reflectance of niobium doped titania. A) Differential reflectance spectra of doped titania fibers plotted vs amount of niobium dopant. B) Photon energy required for electron transition based on differential reflectance spectra.

CHAPTER 4 CONCLUSIONS AND FUTURE WORK

Ceramic filter media was developed for in-habitat application in the lunar environment. Ceramics have been chosen as the preferred class of materials due to the abrasive nature of dust particles on the Moon. The two most common types of filters are porous and fibrous and between these two types, fibrous filters are preferred as they exhibit lower pressure drop. The lower pressure drop ensures more conservation of energy. But the initial problem with this approach was the general brittleness of ceramic fibers. Most such fibermats are too brittle and cannot withstand the minimum pressure applied during testing and application. However $\text{TiO}_2\text{-SiO}_2$ fibermats, heat treated at 600°C for 3 hours, were found to be flexible and mechanically robust enough to be used as filtration media. Heat treatment at 600°C for 3 hour is not enough for crystallizing $\text{TiO}_2\text{-SiO}_2$ and the material remains amorphous even though the polymeric aid burns off completely. No surface defect, which can act as crack initiation site, was observed on the surface of the glassy fibers under SEM and TEM. This reduction in crack initiation sites is proposed to be the reason behind the observed flexibility. Pore size distribution of the $\text{TiO}_2\text{-SiO}_2$ fibers, obtained using BJH technique, demonstrates that most surface pores have a diameter of approximately 2.5 nm.

Tests have been performed to determine the filtration properties of the fibermat. In an apparent contradiction to theoretical expectation, pressure drop normalized with respect to either mass or thickness decreases with increase in fiber diameter. Using mathematical deductions it appears that fibermats with larger fibers have a lower packing density. A lower packing density implies a higher void ratio which in turn means

that it's easier for air to pass through the filter. This can sufficiently explain the observed discrepancy.

The final part of the research is an attempt to increase the utility of the fibermats in such a way that they can be cleaned and re-used multiple times. Photocatalysis has been selected for this purpose due to the absence of abundant energy sources in space. Fibers were electrospun from sols of pure titania and niobium doped titania. The electrospun fibers were characterized for their photocatalytic properties and surface porosity. There seems to be a steady decline in the photocatalytic activity of titania with the increase in the niobium dopant concentration. In general semi-conductor junctions provide trapping levels for electrons and increases photocatalytic activity of a material. Niobium suppresses the phase transformation of anatase to rutile. This decrease in the number and volume of such anatase – rutile junctions may be one of the reasons behind the loss in photocatalytic activity. Also, in the theory behind the hypothesis that doping niobium would increase photocatalytic activity, it is assumed that the niobium atoms substitute titanium atoms from the lattice. Instead, if niobium atoms segregate to the grain boundaries or occupy interstitial spaces, the theory is not applicable. There is also a third factor, which if true, can explain the observation. Sometimes doping transition metal in titania creates energy levels which promote electron-hole recombinations instead of inhibiting them. This has been observed earlier in case of chromium doping of titania. If a similar phenomenon takes place for niobium, it can also explain the decrease in photocatalytic activity. And as far as surface area is concerned, it appears that there is a significant increase with increase in the dopant level. BJH analyses of the doped fibers confirm that there is a corresponding increase in the

number and volume of surface pores with increase in the amount of niobium added as a dopant.

Due to the constraints on time and resources, several aspects have been left to be studied in the future. Using data obtained from experimental observations in mathematical equations, it appears that the packing density of fibers decreases with increase in fiber diameter. But is there a relationship between the applied electric field strength and the packing density? Higher electric field strength ensures a larger electrostatic force which in theory should improve the packing density. This remains an area to be looked into in the future. Finally the location of the deposition of niobium atoms in the lattice is an important factor. When the sol-gel process is used, do the niobium atoms really substitute the titanium atoms in the lattice? Or do they segregate to the grain boundaries? The photocatalytic activity of titania decreases with increase in the amount of niobium doped into it. But what is the exact mechanism behind this behavior? All these are still open questions to be answered in the future.

LIST OF REFERENCES

- [1] M. Horanyi, *Annual Review of Astronomy and Astrophysics* **1996**, 34, 383.
- [2] T. J. Stubbs, R. R. Vondrak, W. M. Farrell, *Advances in Space Research* **2006**, 37, 59.
- [3] M. Rehders, B. B. Grosshauser, A. Smarandache, A. Sadhukhan, U. Mirastschijski, J. Kempf, M. Dunne, K. Slenzka, K. Brix, *Advances in Space Research* **2011**, 47, 1200.
- [4] N. Khan-Mayberry, *Acta Astronautica* **2008**, 63, 1006.
- [5] N. Khan-Mayberry, J. T. James, R. Tyl, C. W. Lam, *International Journal of Toxicology* **2011**, 30, 3.
- [6] W. C. Hinds, *Aerosol Technology: Properties, Behavior, and Measurement of Airborne Particles*, 2nd ed., Wiley-Interscience, **1999**.
- [7] DOE-STD-3020-97, Washington, D.C. 20585, **1997**.
- [8] Understanding Respiratory Protection Against SARS, *National Institute for Occupational Safety and Health*, **2003**.
- [9] T. Hahn, M. Cummings, A. M. Michalek, B. J. Lipman, B. H. Segal, P. L. McCarthy, *Infection Control and Hospital Epidemiology* **2002**, 23, 525.
- [10] A. Rengasamy, Z. Zhuang, R. BerryAnn, *American Journal of Infection Control* **2004**, 32, 345.
- [11] W. C. Hinds, *Aerosol technology : properties, behavior, and measurement of airborne particles.*, 2nd ed., Wiley-Interscience, **1999**, 182-205.
- [12] C. Y. Chen, *Chemical Reviews* **1955**, 55, 595.
- [13] H.-C. Yeh, B. Y. H. Liu, *Journal of Aerosol Science* **1974**, 5, 191.
- [14] E. Cunningham, *Proceedings of the Royal Society of London. Series A, Containing Papers of a Mathematical and Physical Character* **1910**, 83, 357.
- [15] A. Podgórski, A. Balazy, L. Gradon, *Chemical Engineering Science* **2006**, 61, 6804.
- [16] R. S. Barhate, S. Ramakrishna, *Journal of Membrane Science* **2007**, 296, 1.
- [17] Z. W. Ma, M. Kotaki, R. Inai, S. Ramakrishna, *Tissue Engineering* **2005**, 11, 101.

- [18] R. Vasita, D. S. Katti, *International Journal of Nanomedicine* **2006**, 1, 15.
- [19] J. A. Matthews, G. E. Wnek, D. G. Simpson, G. L. Bowlin, *Biomacromolecules* **2002**, 3, 232.
- [20] S. Nair, J. Kim, B. Crawford, S. H. Kim, *Biomacromolecules* **2007**, 8, 1266.
- [21] E. Ochoa-Fernandez, D. Chen, Z. X. Yu, B. Totdal, M. Ronning, A. Holmen, *Surface Science* **2004**, 554, L107.
- [22] Z. K. Walczak, 1/e ed., **2002**, pp. 1.
- [23] F. K. Ko, in *Nanomaterials Handbook*, 1/e ed. (Ed.: Y. Gogotsi), **2006**, pp. 553.
- [24] W. Sigmund, J. Yuh, H. Park, V. Maneeratana, G. Pyrgiotakis, A. Daga, J. Taylor, J. C. Nino, *Journal of the American Ceramic Society* **2006**, 89, 395.
- [25] J. Z. Wang, X. B. Huang, J. Xiao, N. Li, W. T. Yu, W. Wang, W. Y. Xie, X. J. Ma, Y. L. Teng, *Journal of Materials Science-Materials in Medicine* **2010**, 21, 497.
- [26] L. J. R. Foster, B. J. Tighe, *Polymer Degradation and Stability* **2005**, 87, 1.
- [27] Y. Ono, T. Ichiryu, I. Ohnaka, I. Yamauchi, *Journal of Alloys and Compounds* **1999**, 289, 220.
- [28] D. Li, Y. Xia, *Advanced Materials* **2004**, 16, 1151.
- [29] D. Li, Y. Xia, *Nano Letters* **2003**, 3, 555.
- [30] F. Anton, Richard, Schreiber Gastell, Anton, Formhals, United States Patent No. 1975504, **1934**.
- [31] F. Anton, Richard, Schreiber Gastell, United States Patent No. 2160962, **1939**.
- [32] Y. M. Shin, M. M. Hohman, M. P. Brenner, G. C. Rutledge, *Polymer* **2001**, 42, 9955.
- [33] M. M. Hohman, M. Shin, G. Rutledge, M. P. Brenner, *Physics of Fluids* **2001**, 13, 2201.
- [34] Y. M. Shin, M. M. Hohman, M. P. Brenner, G. C. Rutledge, *Applied Physics Letters* **2001**, 78, 1149.
- [35] H. S. Michael Ashby, David Cebon, *Materials: engineering, science, processing and design*, Butterworth-Heinemann, **2009**.

- [36] V. Augugliaro, L. Palmisano, M. Schiavello, A. Sclafani, L. Marchese, G. Martra, F. Miano, *Applied Catalysis* **1991**, 69, 323.
- [37] T. N. Obee, R. T. Brown, *Environmental Science & Technology* **1995**, 29, 1223.
- [38] X. Z. Fu, W. A. Zeltner, M. A. Anderson, *Applied Catalysis B-Environmental* **1995**, 6, 209.
- [39] M. A. Malati, *Environmental Technology* **1995**, 16, 1093.
- [40] H. Schonhorn, C. R. Kurkjian, R. E. Jaeger, H. N. Vazirani, R. V. Albarino, F. V. Dimarcello, *Applied Physics Letters* **1976**, 29, 712.
- [41] P. W. France, M. J. Paradine, M. H. Reeve, G. R. Newns, *Journal of Materials Science* **1980**, 15, 825.
- [42] Y. Kanno, *Journal of Materials Science Letters* **1990**, 9, 451.
- [43] Z. Liu, Q. Zhang, L.-C. Qin, *Solid State Communications* **2007**, 141, 168.
- [44] T. Umebayashi, T. Yamaki, H. Itoh, K. Asai, *Journal of Physics and Chemistry of Solids* **2002**, 63, 1909.
- [45] G. Pyrgiotakis, PhD Dissertation thesis, University of Florida (Gainesville), **2006**.
- [46] A. Mills, S. LeHunte, *Journal of Photochemistry and Photobiology a-Chemistry* **1997**, 108, 1.
- [47] A. L. Linsebigler, G. Q. Lu, J. T. Yates, *Chemical Reviews* **1995**, 95, 735.
- [48] M. R. Hoffmann, S. T. Martin, W. Choi, D. W. Bahnemann, *Chemical Reviews* **1995**, 95, 69.
- [49] S. T. Martin, H. Herrmann, W. Choi, M. R. Hoffmann, *Journal of the Chemical Society, Faraday Transactions* **1994**, 90, 3315.
- [50] S. T. Martin, H. Herrmann, M. R. Hoffmann, *Journal of the Chemical Society, Faraday Transactions* **1994**, 90, 3323.
- [51] T. J. Kemp, R. A. McIntyre, *Polymer Degradation and Stability* **2006**, 91, 165.
- [52] J.-M. Herrmann, J. Disdier, P. Pichat, *Chemical Physics Letters* **1984**, 108, 618.
- [53] N. Serpone, D. Lawless, J. Disdier, J.-M. Herrmann, *Langmuir* **1994**, 10, 643.

- [54] Y. Sakata, T. Yamamoto, T. Okazaki, H. Imamura, S. Tsuchiya, *Chemistry Letters* **1998**, 27, 1253.
- [55] M. Iwasaki, M. Hara, H. Kawada, H. Tada, S. Ito, *Journal of Colloid and Interface Science* **2000**, 224, 202.
- [56] H. Kato, A. Kudo, *The Journal of Physical Chemistry B* **2002**, 106, 5029.
- [57] J. Zhang, L. Xiao, Y. Cong, M. Anpo, *Topics in Catalysis* **2008**, 47, 122.
- [58] E. C. Butler, A. P. Davis, *Journal of Photochemistry and Photobiology A: Chemistry* **1993**, 70, 273.
- [59] Z. Zhang, C. Shao, L. Zhang, X. Li, Y. Liu, *Journal of Colloid and Interface Science* **2010**, 351, 57.
- [60] H. Yamashita, Y. Ichihashi, M. Takeuchi, S. Kishiguchi, M. Anpo, *Journal of Synchrotron Radiation* **1999**, 6, 451.
- [61] W. Choi, A. Termin, M. R. Hoffmann, *The Journal of Physical Chemistry* **1994**, 98, 13669.
- [62] Z. H. Luo, Q. H. Gao, *Journal of Photochemistry and Photobiology a-Chemistry* **1992**, 63, 367.
- [63] L. Palmisano, V. Augugliaro, A. Sclafani, M. Schiavello, *Journal of Physical Chemistry* **1988**, 92, 6710.
- [64] Y. Q. Wang, Y. Z. Hao, H. M. Cheng, J. M. Ma, B. Zu, W. H. Li, S. M. Cai, *Journal of Materials Science* **1999**, 34, 2773.
- [65] Y. Wang, H. Cheng, Y. Hao, J. Ma, W. Li, S. Cai, *Thin Solid Films* **1999**, 349, 120.
- [66] Y. Matsumoto, J.-i. Kurimoto, T. Shimizu, E.-i. Sato, *Journal of the Electrochemical Society* **1981**, 128, 1040.
- [67] M. Hirano, K. Matsushima, *Journal of the American Ceramic Society* **2006**, 89, 110.
- [68] X. J. Lu, X. L. Mou, J. J. Wu, D. W. Zhang, L. L. Zhang, F. Q. Huang, F. F. Xu, S. M. Huang, *Advanced Functional Materials* **2010**, 20, 509.
- [69] P. S. Archana, R. Jose, M. M. Yusoff, S. Ramakrishna, *Applied Physics Letters*, **2011**, 98,152106.

- [70] M. Hirano, Y. Ichihashi, *Journal of Materials Science* **2009**, *44*, 6135.
- [71] J. Arbiol, J. Cerda, G. Dezanneau, A. Cirera, F. Peiro, A. Cornet, J. R. Morante, *Journal of Applied Physics* **2002**, *92*, 853.
- [72] R. D. Shannon, J. A. Pask, *Journal of the American Ceramic Society* **1965**, *48*, 391.
- [73] A. Sclafani, J. M. Herrmann, *Journal of Physical Chemistry* **1996**, *100*, 13655.
- [74] Y. Dai, W. Liu, E. Formo, Y. Sun, Y. Xia, *Polymers for Advanced Technologies* **2010**, *22*, 326.
- [75] G. Vazquez, E. Alvarez, J. M. Navaza, *Journal of Chemical & Engineering Data* **1995**, *40*, 611.
- [76] L. P. Xu, Y. X. Zhao, Z. G. Wu, D. S. Liu, *Chinese Chemical Letters* **2003**, *14*, 1159.
- [77] H. Park, PhD Dissertation thesis, University of Florida (Gainesville), **2010**.
- [78] C. Guillard, H. Lachheb, A. Houas, M. Ksibi, E. Elaloui, J. M. Herrmann, *Journal of Photochemistry and Photobiology a-Chemistry* **2003**, *158*, 27.
- [79] S.-i. Nishimoto, B. Ohtani, T. Kagiya, *Journal of the Chemical Society, Faraday Transactions 1: Physical Chemistry in Condensed Phases* **1985**, *81*, 2467.
- [80] B. Ohtani, Y. Okugawa, S. Nishimoto, T. Kagiya, *The Journal of Physical Chemistry* **1987**, *91*, 3550.
- [81] S. G. L. Sarabjit Singh, M. Vijayakumar, *NanoBiotechnology* **2009**, *5*, 10.
- [82] A. Biswas, H. Park, W. M. Sigmund, *Ceramics International* **2012**, *38*, 1, 883.
- [83] S. J. Park, G. G. Chase, K. U. Jeong, H. Y. Kim, *Journal of Sol-Gel Science and Technology* **2010**, *54*, 188.
- [84] D. A. Reneker, OH, US), Chase, George (Wadsworth, OH, US), Kataphinan, Woraphon (Akron, OH, US), Katta, Prathyusha (Oxnard, CA, US), THE UNIVERSITY OF AKRON (Akron, OH, US), United States Patent Application No. 20080242178 , **2008**.
- [85] E. T. Bender, P. Katta, G. G. Chase, R. D. Ramsier, *Surface and Interface Analysis* **2006**, *38*, 1252.
- [86] B. Ding, H. Kim, C. Kim, M. Khil, S. Park, *Nanotechnology* **2003**, *14*, 532.

- [87] Y. Liu, S. Sagi, R. Chandrasekar, L. F. Zhang, N. E. Hedin, H. Fong, *Journal of Nanoscience and Nanotechnology* **2008**, 8, 1528.
- [88] J. Wang, S. C. Kim, D. Y. H. Pui, *Aerosol Science and Technology* **2008**, 42, 722.
- [89] Q. Zhang, J. Welch, H. Park, C. Y. Wu, W. Sigmund, J. C. M. Marijnissen, *Journal of Aerosol Science* **2010**, 41, 230.
- [90] K.-c. Fan, J. W. Gentry, *Industrial & Engineering Chemistry Fundamentals* **1979**, 18, 306.
- [91] J. Wang, S. C. Kim, D. Y. H. Pui, *Journal of Aerosol Science* **2008**, 39, 323.
- [92] K. Tanaka, M. F. V. Capule, T. Hisanaga, *Chemical Physics Letters* **1991**, 187, 73.
- [93] M. Kanna, S. Wongnawa, S. Buddee, K. Dilokkhunakul, P. Pinpithak, *Journal of Sol-Gel Science and Technology* **2010**, 53, 162.
- [94] B. Ohtani, Y. Ogawa, S.-i. Nishimoto, *The Journal of Physical Chemistry B* **1997**, 101, 3746.
- [95] S. C. Jung, N. Imaishi, *Korean Journal of Chemical Engineering* **2001**, 18, 867.
- [96] L. Wei, C. Shifu, *Journal of the Electrochemical Society* **2010**, 157, H1029.
- [97] L. Wei, C. Shifu, Z. Sujuan, Z. Wei, Z. Huaye, Y. Xiaoling, *Journal of Nanoparticle Research* **2010**, 12, 1355.
- [98] P. L. Kheamrutai Thamaphat, Boonlaer Ngotawornchai, *Kasetsart Journal: Natural Science* **2008**, 42, 357.
- [99] J. T. A. Ahmad, and S. Ismat Shah, *Journal of Physics: Conference Series* **2007**, 61, 11.
- [100] S. Brunauer, P. H. Emmett, E. Teller, *Journal of the American Chemical Society* **1938**, 60, 309.
- [101] D. F. Swinehart, *Journal of Chemical Education* **1962**, 39, 333.
- [102] N. Serpone, *The Journal of Physical Chemistry B* **2006**, 110, 24287.
- [103] M. Lira-Cantu, M. K. Siddiki, D. Munoz-Rojas, R. Amade, N. I. Gonzalez-Pech, *Solar Energy Materials and Solar Cells* **2010**, 94, 1227.

- [104] A. Biswas, H. Park, W. M. Sigmund, N. Afshar-Mohajer, C.-Y. Wu, in *41st International Conference on Environmental Systems*, American Institute of Aeronautics and Astronautics, Inc., Portland, Oregon, **2011**, AIAA 2011-5185.

BIOGRAPHICAL SKETCH

As a graduate student, Apratim Biswas has worked on processing and characterizing electrospun fibers as a member of Dr. Wolfgang M. Sigmund's research group in the Department of Materials Science and Engineering at the University of Florida. Apart from processing technology, a major part of his work involves studying photocatalysis. He graduated with a Bachelor of Engineering degree with honors in Metallurgy and Materials Engineering from the Bengal Engineering and Science University in India in 2007.